UC Berkeley
UC Berkeley Electronic Theses and Dissertations

Title

Lithium Plating Detection, Quantification, and Modeling to Enable Lithium-Ion Battery Fast-Charging

Permalink

https://escholarship.org/uc/item/9mz0z29j

Author

Konz, Zachary Martin

Publication Date

2023

Peer reviewed|Thesis/dissertation

Lithium Plating Detection, Quantification, and Modeling to Enable Lithium-Ion Battery Fast-Charging

By

Zachary Martin Konz

A dissertation submitted in partial satisfaction of the

requirements for the degree of

Doctor of Philosophy

in

Chemical Engineering

in the

Graduate Division

of the

University of California, Berkeley

Committee in charge:

Professor Bryan D. McCloskey, Chair
Professor Nitash P. Balsara
Professor Scott J. Moura

Summer 2023

Abstract

Lithium Plating Detection, Quantification, and Modeling to Enable Lithium-Ion Battery Fast-Charging

by

Zachary Martin Konz

Doctor of Philosophy in Chemical Engineering

University of California, Berkeley

Professor Bryan D. McCloskey, Chair

A key challenge for energy storage and conversion technologies is finding simple, reliable methods that can identify device failure and prolong lifetime. Lithium plating is a well-known degradation process that prevents Li-ion battery fast charging, which is essential to reduce electric vehicle 'range anxiety' and enable emerging technologies such as aerial drones and high-performance portable electronics. The ability to detect the initial onset of lithium plating from easily accessible voltage measurements would greatly improve battery safety and feedback controls modeling. In this work, we first highlight the application of a differential open-circuit voltage analysis (dOCV) to detect when Li plating begins during a single charge for room temperature fast charging. We also show that dOCV can identify the Li plating onset during cycling with sensitivity of 1 mg plated Li per gram graphite, equivalent to 1% of the graphite capacity, indicating that this method has commercial promise for on-line Li detection.

Next, we demonstrate the power of simple, accessible, and high-throughput cycling techniques to quantify irreversible Li plating spanning data from over 200 cells. We first observe the effects of energy density, charge rate, temperature, and State-of-Charge (SOC) on lithium plating, use the results to refine mature physics-based electrochemical models, and provide an interpretable empirical equation for predicting the plating onset SOC. We then explore the reversibility of lithium plating and its connection to electrolyte design for preventing irreversible Li accumulation. Finally, we design a method to quantify in-situ Li plating for commercially relevant Graphite|LiNi$_{0.5}$Mn$_{0.3}$Co$_{0.2}$O$_2$ (NMC) cells and compare with results from the experimentally convenient Li|Graphite configuration. The hypotheses and abundant data in this section were generated primarily with equipment universal to the battery researcher, encouraging further development of innovative testing methods and data processing that enable rapid battery engineering.

Finally, we consider the challenge of highly variable charging conditions possible in commercial cells. We combine pseudo-2D electrochemical modeling with data visualization methods to reveal important relationships between the measurable cell voltage and difficult-to-predict Li plating onset criteria. An extensively validated model is used to compute lithium plating for thousands of multistep charging conditions spanning diverse rates, temperatures, states-of-charge (SOC), and

cell aging. We observe an empirical cell operating voltage limit below which plating does not occur across all conditions, and this limit varies with battery state-of-charge and aging. A model sensitivity analysis also indicates that when comparing two charging voltage profiles, the capacity difference at 4.0V correlates well with the difference in the plating onset capacity. These results encourage simple strategies for Li plating prevention that are complementary to existing battery controls.

Table of Contents

Acknowledgements

McCloskey Lab at UC Berkeley. I am first and foremost extremely grateful for the continuous guidance from Professor Bryan D. McCloskey, who was a supportive mentor and advocate for me throughout the PhD and also works tirelessly on behalf of all PhD students in the UC Berkeley Department of Chemical and Biomolecular Engineering. I also acknowledge Dr. Eric McShane, who was an excellent mentor and friend during the first years of my PhD. Brendan Wirtz was a gifted mentee who contributed intellectually to our work and also helped me learn about mentorship. Drs. David Brown, Lori Kaufman, Kara Fong, Tzu-Yang Huang, and Matt Crafton were also great teachers and friends in the McCloskey lab. A special acknowledgement to Dr. Helen Bergstrom for her intellectual, lab safety, and equipment troubleshooting contributions. Thanks to all McCloskey lab members past and present for great discussions and fun over lunch, especially office-mate Ning Guo.

Collaborators. Dr. Andrew Colclasure was an important collaborator throughout the PhD with abundant knowledge of electrochemical modeling and experiments, and I am grateful for his support and encouragement to join his team at NREL through the DOE fellowship. I thank Dr. Peter Weddle for his help learning about electrochemical modeling, how to use COMSOL, and for creating an inclusive work environment at NREL. I also acknowledge Dr. Paul Gasper, who provided many resources to learn about machine learning and offered invaluable insights throughout our joint project. Dr. Ankit Verma also contributed to our modeling efforts and helped with understanding model formulas. I also thank Professors Scott Moura and Aditi Krishnapriyan as well as Dr. Eric Taw for their time to discuss machine learning efforts in Spring 2023.

Early Science Educators and Opportunities. Going backwards chronologically, there are many people who helped put me on the path towards a successful PhD. Dr. Joe Chada was a great resource and role-model for scientific mentorship in the Huber Group in the University of Wisconsin-Madison Department of Chemical and Biological Engineering. Dr. Mohammad Rafiee provided countless hours of mentorship and advice throughout 2.5 years in the Stahl Group at UW. An internship in Summer 2015 with Ecolab, supervised by Derrick Andersen and Dr. Victor Mann, inspired me to get involved in research and pursue a PhD. I thank inspiring professors and teaching assistants throughout undergraduate degree including Prof. Regina Murphy, Prof. James Rawlings, Allison Balloon, and Dr. Andrew Maza. The courses EPD397 and CBE324 were invaluable for providing a strong foundation for Technical Writing. I also remember brilliant, motivating friends to pursue academic excellence at Franklin High School, including Emma Klein, MPH, and Austin Bohn, who was a wonderful human and friend to so many.

Chemical and Biomolecular Engineering (CBE) Department at UC Berkeley. I thank the CBE Graduate Student Advisory Committee (GSAC) for their leadership and efforts to make the

department a more inclusive, supportive, and social environment. Carlet Altamirano and Joseph Nolan provided seamless administrative support throughout the PhD. I thank the department leadership, the department DEI committee for helping to address equity challenges, and the Union members who assisted achieving higher wages for graduate students across the UC.

CBE Cohort of 2018 and Friends. The CBE 2018 cohort of PhD students was very supportive and provided important social and intellectual opportunities throughout the degree. Special thanks to roommates Clay Batton, Johnny Petrovick III, Branden Leonhardt, and Justin Baerwald for the fun times and support, as well as friends Sal Butrus, Natalie Lefton, Ana Carneiro, Neel Shah, Eric Taw, Emily Carvahlo, and Sam Crowe. Also thanks to close friend Daniel Gabay for his constant support and dedication to having fun and showing me new experiences during the long PhD.

Berkeley Community. Ohlone Park Volleyball Club was an incredible group dedicated to having fun while staying safe during the pandemic. The Lewis Base Stealers softball team as well as past intramural soccer teams were a great way to stay competitive and fit while having fun. The Bay Area Jewish community including various Moishe House groups and The Kitchen in San Francisco were essential spiritual and social connectors outside of UC Berkeley. Finally, a huge thanks to Professor Kyungmi 'Lucy' Yoo, a PE Instructor at UC Berkeley who emphasized the importance to learn dance and live fully through Salsa I, Salsa II, and Swing I classes.

Family. The most important for last – thank you to my grandparents, great-grandparents, and beyond for the sacrifices you made to enable me to attend UW-Madison and UC Berkeley and earn degrees in Chemical Engineering. You endured various hardship and religious persecution that I have never known and persevered, and I hope you are proud of what I have been able to do with this life of freedom. Another thanks to my cousins and other relatives for their support, love, and friendship throughout this time when it has been hard to reciprocate from the west coast. My brothers Matthew and Aaron are my best friends and their support while attending to their own endeavors means a lot, and adding Kelsey to the family during the PhD was a highlight. Finally, I am always lucky to have amazingly intelligent, supportive, loving, and quirky parents. Our talks throughout grad school have helped me see them independently as good friends, and during hard times, the combination of Mom's compassion and action-oriented thinking with Dad's optimism and thoughtfulness is the best I could ask for. Love you all!

1. An introduction to Li plating in Li-ion batteries

Creating a transportation system powered by renewable energy is a promising solution to reduce greenhouse gas emissions, improve urban air quality, and slow the costly effects of climate change. This task will require the broad application of diverse energy storage and conversion technologies, especially the lithium-ion batteries used for electric vehicles (EV). Despite recent growth, consumers are hesitant to adopt EVs due to long charging times, or 'range anxiety,' and EVs still only accounted for 7% of U.S. new vehicle sales in 2023[1]. As a result, the U.S. Department of Energy has set an ambitious goal for designing a lithium-ion battery (LIB) pack that can withstand a 200-mile charge in only 10 minutes[2].

The most recent advances in LIB technology address one of the key barriers to fast-charging, which is the ability to predict highly variable battery lifetimes. Severson et al. leveraged the power of machine learning to develop a model that can predict cycle life within 9% of the true value using discharge voltage data from the first 100 cycles[3]. Zhang et al. then showed that only a single impedance measurement, collected at any point during cycling, could give information about remaining battery capacity and useful life[4]. These learning-based predictive models, however, require extensive training data and may not detect anomalous cell failure.

A remaining challenge for LIB fast-charging is identifying unsafe battery conditions in real-time. This includes detection of the lithium plating reaction at graphite electrodes, the cell component widely recognized as limiting for fast-charging performance[5,6]. The LIB charge process requires the release of lithium ions (Li^+) from the positive electrode and insertion of Li^+ into the graphite negative electrode (Fig. 1a). During fast charge, however, the severe electrode polarization required to sustain high current densities causes the graphite voltage to deviate significantly from equilibrium. Fig. 1b illustrates how the graphite voltage is expected to decrease throughout charge for various current densities, a composite effect of the applied rate and Li concentration gradients in the electrolyte and solid phases. When the voltage goes below 0 V vs. Li/Li^+, the deposition of lithium metal (Li^0) onto the graphite surface becomes thermodynamically favorable. This process is referred to as Li plating. In extreme cases, plated Li can protrude through the porous polymeric

$$xLi^+ + xe^- + C_6 \rightarrow Li_xC_6 \quad 0 \le x \le 1$$
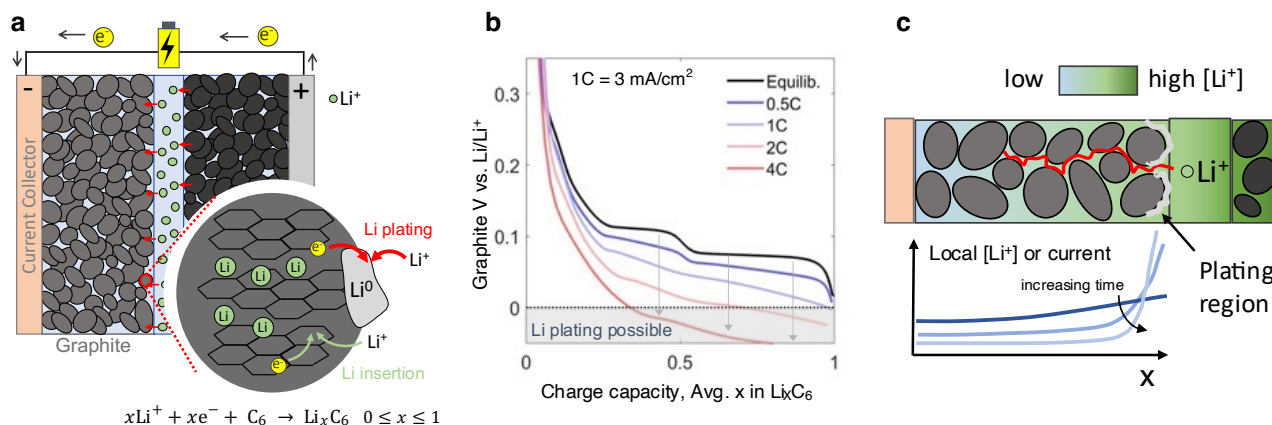
Fig. 1. Battery fast-charging and the lithium plating reaction. a, Li-ion battery charging with a graphite negative electrode. The unwanted Li plating reaction may occur in addition to standard Li insertion. **b,** The graphite electrode potential decreases throughout charge as it is filled with lithium. At high current rates, the voltage may go below 0 V vs. Li/Li^+. **c,** Electrolyte-phase ion transport within the porous electrode is slow relative to the reaction rate at fast charging conditions, causing gradients in concentration and current density along the electrode depth (x direction) that increase with time.

battery separator to the positive electrode, causing cell shorting that sparks electrolyte oxidation and dangerous thermal runaway. Li plating also results in both short-term efficiency losses due to the low reversibility of the Li plating/stripping process as well as long-term capacity fade from the decrease in cyclable lithium and increased cell resistances over time[7].

Many interconnected phenomena influence when and where in the electrode that Li plating occurs, making it difficult to predict with even the highest fidelity electrochemical models. Sluggish kinetics for the graphite intercalation reaction, which may decrease over cell lifetime due to the continuous growth of the solid electrolyte interphase (SEI)[8,9], necessitate the electrode polarization that pushes the voltage below 0 V vs. Li/Li$^+$. The rate of solid-phase transport of lithium from the graphite particle surface to interior may limit the rate of the surface intercalation reaction. Most importantly, the rapid depletion of Li$^+$ in the electrolyte within the porous electrode causes severe underutilization of the graphite near the current collector. High local current densities result near the separator interface, where Li$^+$ is most abundant, and thus this is where plating is frequently observed experimentally (Fig. 1c)[10]. Modeling suggests that electrode properties affecting the local electrolyte diffusivity, such as the porosity and tortuosity, are especially influential for performance[11]. This is consistent with reports of successful fast-charging using 3D-architectured graphite electrodes containing vertical pore channels to enhance ion transport[12,13].

1.1. Key Research Gaps

While Li plating is a widely reported failure mechanism, there are many challenges to accurately detecting and quantifying the reaction, which is critical to engineering new strategies that avoid it. The first challenge is that many characterization techniques such as solid state ^{7}Li NMR[14], X-ray diffraction, neutron diffraction[15], optical emission spectroscopy[16], electron paramagnetic resonance (EPR) spectroscopy[17], and acoustics[18] require special cell designs and probes. A more comprehensive list of these techniques has been compiled elsewhere[19]. To ensure widespread implementation in laboratories and battery control systems, in situ detection techniques are needed that rely only on simple, accessible electrochemical parameters such as voltage, current, and capacity.

A challenge for electrochemical plating detection is that it is difficult to measure the point at which the graphite voltage drops below 0 V vs. Li/Li$^+$ is in full battery cells. This is because the voltage of the cathode, typically comprised of a layered lithium transition metal oxide active material, also changes significantly during fast charge. The potential difference between the two electrodes is the only conveniently measured voltage output, thereby hindering the discovery of a simple and accurate voltage measurement method to identify the point at which Li plating could occur.

Methods for monitoring and predicting Li plating would be an invaluable safety feature for commercial batteries, a characterization means for fundamental fast-charging studies, and a predictive tool for long-term battery performance. Modern measures to avoid Li plating – such as setting conservative voltage cutoffs during charge, oversizing graphite electrodes, and heating batteries before charge – could be relaxed and lead to more efficient battery operation. Simple Li quantification technology would also fill a recognized gap in capabilities to study and assess new fast-charging materials[20]. This includes studying graphite electrodes with higher loadings, in which Li plating is more favorable, which must be considered for higher energy density LIB[21].

1.2. Contributions

This work is divided into three sections pertaining to the detection, quantification, and modeling of Li plating, respectively. We define *detection* as using battery voltage signals to determine whether or not plating has occurred immediately after charging, within about 30 minutes and without additional cycling tests. *Quantification* refers to determining the specific amount of plating, either with multi-cycle test protocols or by applying chemical analysis tools to the graphite electrode. Finally, the *modeling* work uses physics to estimate the battery voltage evolution during charge and understand the voltage connection to lithium plating for diverse conditions. Major novel intellectual contributions of this work include:

Chapter 2. The design and validation of an in situ Li plating detection technique using voltage relaxation data collected after charge. The testing protocol can quickly determine the SOC at which plating begins, the plating 'onset', for a constant current charge, valuable information for determining when to terminate device charging.

Chapter 3. The development of simple battery testing and data analysis methods to quantify:

- o the accumulation of Li plating as a function of charge duration for a single charge for both Li|Graphite and Graphite|Cathode cell configurations
- o the accumulation of Li plating throughout long-term cell cycling
- o the reversibility of the Li plating reaction

The validation of these methods was enabled by a novel high-throughput version of a chemical titration, which can confidently quantify Li plating on harvested graphite electrodes. Together, the methods generate data from over 200 experimental cells, the largest study of its kind, providing insights about the importance of temperature, charging rate, electrode loading, and electrolyte composition for fast-charging performance.

Chapter 4. Electrochemical modeling that predicts Li plating accumulation for a single charge is newly applied with added aging equations and for thousands of charging protocols that span realistic SOC, temperatures, and rates.

- o Results clearly illustrate the sensitivity of Li plating and voltage to various aging mechanisms.
- o New data visualization methods show that measured voltage differences between nominally identical cells may correlate with the difference in Li plating onset SOC, helping to address variable fast-charge ability with battery packs.
- o Across all charging conditions tested, a universal relationship between plating onset voltage and onset SOC is observed, suggesting a new upper-voltage battery operating boundary curve that is a function of SOC, a simple control to avoid plating.

Together, the contributions demonstrate the chronology of simple laboratory experiments leading to trustworthy electrochemical models that can provide suggestions for fast-charging policy of highly variable large-format cells.

2. Detecting the onset of lithium plating and monitoring fast charging performance with voltage relaxation[1]

2.1. Introduction: Monitoring open circuit voltage to detect Li plating

Perhaps the most practical reported Li plating detection method analyzes the cell open-circuit voltage (OCV) after charge[22–26]. Data for an OCV-based technique could be easily collected in the 5-10 minutes immediately after charging, which could be done in a vehicle by turning off a fraction of the LIB packs while the rest supply the required power. Uhlmann et al. first generated interest in monitoring the OCV after charge by showing that plated Li can chemically intercalate into graphite via corrosion reactions when the cell is at rest[23]. This phenomenon gives rise to a characteristic 'dual plateau' OCV feature, which we highlight in Fig. 2. It is hypothesized that the initial potential plateau during relaxation corresponds to a mixed potential of the plated Li and lithiated graphite (Li_xC_6). As the plated Li chemically intercalates, the mixed Li/Li_xC_6 potential transitions to a pure Li_xC_6 potential after some threshold amount of surface Li has been depleted. This potential decay feature is more prominent as a voltage derivative (Fig. 2, dashed), an analysis first proposed by Schindler et al[22]. Here we will refer to this type of data as a differential OCV (dOCV). While previous authors have used dOCV to study Li plating, the experimental scope has primarily been limited to cold temperatures ($\leq 5°C$)[22,24–27] or charging to high graphite states of charge (SOC, the fraction of total Li that can be inserted) at which point abundant Li has plated.[23] Limited studies show that dOCV signals are less visible as the temperature is increased to 30°C[28,29], but it remains unclear whether this observation is simply due to reduced Li plating at those conditions.

A proposed Li detection technology is only suitable for commercial use if it can reliably detect small, safe quantities of plating at the ambient temperatures used for fast charge. This is an unaddressed question for the dOCV method, but coulombic efficiency (CE) analysis of fast charging cycles in Li|Graphite'half-cells' offers an opportunity for simple, in situ plating quantification. Low CE has long been tied to inefficiencies from lithium plating[30], and has been used to determine C-rates at which plating occurs in graphite|Li(Ni,Mn,Co)O_2 (NMC) full-cells[31]. Efficiencies from full-cell cycling, however, do not provide quantitative information about plating because they are affected by the shifting voltage windows of both electrodes and total Li inventory loss. In contrast, recent work by Tanim et al. illustrates how CEs from graphite half-cell cycling can provide quantitative insights about the Li plating and stripping process due to the large Li inventory surplus provided by the Li counter electrode[32].
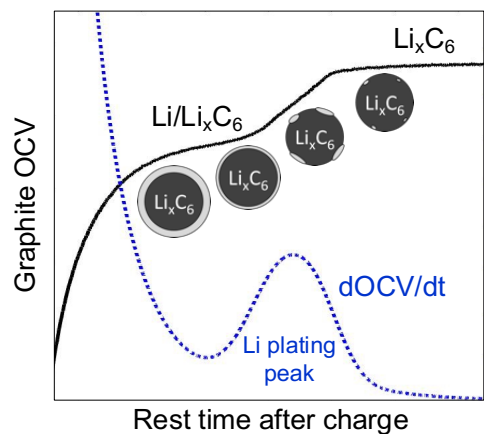

Fig. 2. Voltage response to lithium chemical intercalation during rest. Chemical intercalation is shown schematically as the evolution of a Li-covered graphite (Li_xC_6) particle at various points during OCV, which causes unique features in the OCV and its derivative due to differences in equilibrium potentials of Li^0/Li^+ and Li_xC_6/Li^+.

In this section we report a method for determining when Li plating begins during fast charge using dOCV in Li|Graphitecells. Coulombic efficiencies are used to verify the presence of Li plating and to estimate the detection limit of the technique, an important step towards commercial use. The utility of dOCV for monitoring performance trends in long-term cycling with varied charge durations is shown. Finally, we report a novel cycling procedure that allows us to provide a direct comparison of dOCV with other electrochemical Li detection signals. All experiments in this work were performed at 23°C, so the presented results are relevant for fast charging applications.

2.2. Detecting the SOC onset of Li plating

The ability to predict when lithium plating begins during charging would be invaluable for efficiently designing safe fast charging protocols. To the best of our knowledge, the only prior technique that directly observes Li plating onsets is EPR spectroscopy from Wandt et al.[17], which requires a custom cell design and low temperatures not feasible for widespread application. Rao Koleti et al. have recently proposed an impedance-based method for detecting plating onsets, but
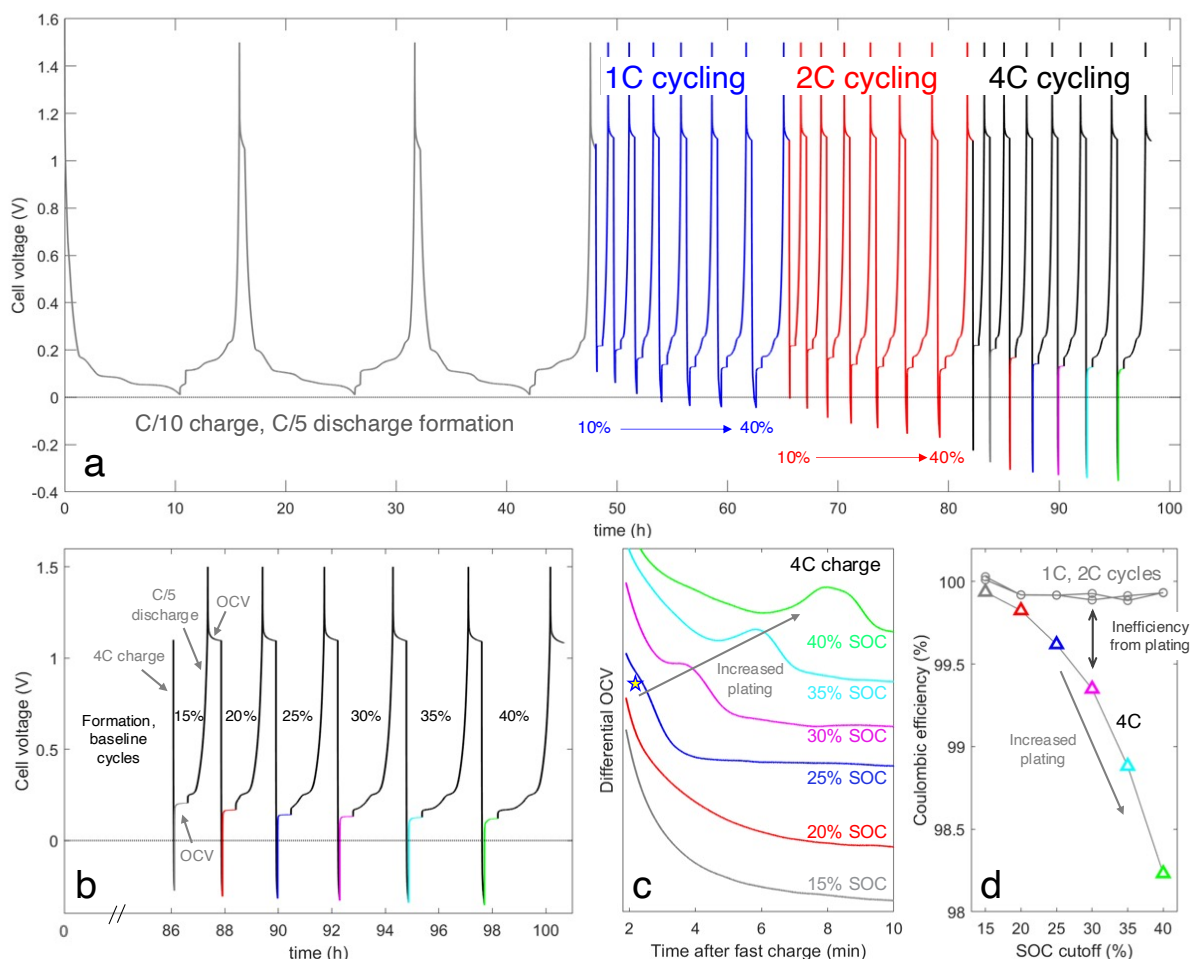
Fig. 3. Detecting the onset of Li plating with dOCV in a Li|Graphitecell. a, Cycling protocol to generate OCV data after charging graphite to 10-40% SOC at 1C, 2C, and 4C rates. All cycles begin with fully delithiated graphite ($x < 0.01$ in Li_xC_6), which is ensured by slow C/5 discharging up to 1.5V. **b,** The 4C fast charge cycles of interest. **c,** Differential OCVs extracted from cycling data in (b). After 4C charging to 25-40% SOC, the dOCV profiles show an inflection point feature not observed at 15-20% SOC, suggesting plating begins near 25% SOC (star). **d,** Coulombic efficiencies for the cycles in (a).

they have not verified the absence of Li plating before the onset nor the presence of plating immediately after the onset[29]. A robust technique for determining plating onsets would be invaluable for assessing the fidelity of predictive tools such as mathematical modeling[25,26] or reference electrode potential monitoring[33]. The latter predicts Li plating when the graphite potential reaches 0 V vs. Li/Li^{+}, but this thermodynamic plating threshold does not consider possible kinetic limitations or nucleation energy barriers.

Fig. 3a illustrates a progressive cell cycling technique combined with dOCV analysis that was applied to detect the onset of Li plating. A Li|Graphitecell was cycled repeatedly with a 4C charge rate to varied SOC cutoffs between 15-40% to generate voltage relaxation data corresponding to different charge durations (Fig. 3b, colored). Significant Li plating is expected at 4C for this electrode architecture (see Methods for electrode properties), the rate corresponding to a full charge in 15 minutes, and prior measurements indicated that the Li plating onset SOC is roughly 15-40%. The voltage relaxation profile derivatives (dOCV) from the cycling are seen in Fig. 2b. After the 25% charge (Fig. 3c, blue), an inflection point feature is observed in the dOCV and becomes more prominent for the 30-40% SOC cycles (Fig. 3c, pink, light blue, green). We attribute this feature to Li plating because increased Li plating and a more prominent signal is expected at higher SOC. The shift of the dOCV peak position to longer times has been previously correlated with higher amounts of Li plating[22,23,25], and von Lüders et al. suggest this relationship is approximately linear[24]. Li plating becomes more favorable at higher SOC for a number of reasons, including: the buildup of Li^{+} concentration gradients over time that leads to higher overpotentials near the electrode-separator interface, the decrease of graphite solid state Li diffusion coefficient with increasing Li content, and intraparticle lithiation gradients that result in LiC_6 near the particle surface which prevents further intercalation[34,35].

Coulombic efficiency (CE) analysis of the plating onset cycling in Fig. 3d provides strong evidence that dOCV signals correspond to Li plating instead of other graphite phase relaxation processes. Past work studying graphite phase relaxation after fast charge suggests that, for our cycling temperature and graphite SOC range, voltage derivative features are possible from the relaxation of LiC_6 to LiC_{12} as well as the depletion of plated surface lithium[28]. We conclude that the dOCV feature corresponds to surface lithium depletion because the coulombic efficiencies – the ratio of discharge and charge capacities – for those same cycles drop from the 99.9% baseline observed at lower rates and SOC (Fig. 3d). These efficiency drops are expected because the chemical intercalation of plated Li is known to leave behind inactive or 'dead' Li, which contributes to capacity fade.

This plating onset estimation technique was also successfully applied to fresh cells at 3C and 2C rates (Fig. 4, Fig. S3, Fig. S4). Progressive cycling on these cells was
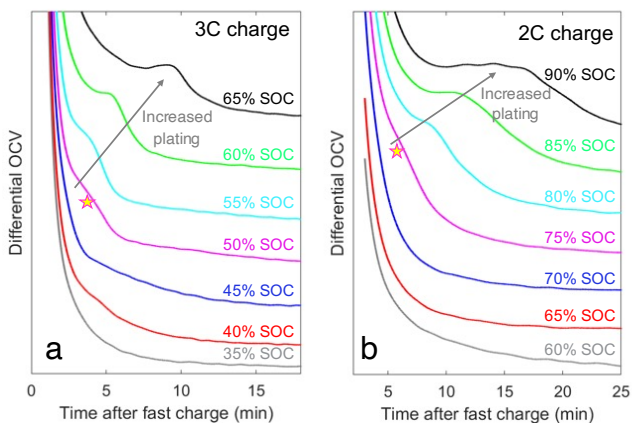
Fig. 4. Detecting the onset of Li plating at 3C and 2C rates. Differential OCVs corresponding to 3C (a) and 2C (b) charging were generated with identical cycling protocols to that in Fig. 3a but with different charge rates and graphite SOC cutoffs. **a,** After charging to 50-65% SOC at 3C, the dOCV profiles show an inflection point feature (star) not seen for 35-45% SOC that we attribute to plating. **b,** After charging to 75-90% SOC at 2C, the dOCV plating feature (star) is observed.

3

performed with delayed SOC cutoffs ranging 35-65% SOC for 3C and 60-90% SOC for 2C given later expected onsets for lower rates. The dOCV profiles after 3C charging in Fig. 4a first show a plating inflection point feature beginning at 50% SOC (pink star), and this onset is confirmed by a corresponding 0.3% CE decrease from 99.7 to 99.4% between the 45 and 50% SOC cycles (see Fig. S3 for CE data). We attribute the unique shape of the 40-45% SOC curves to LiC_6 relaxation to LiC_{12} because similar features are observed at these SOC in other experiments (see Fig. S6b). Similarly, dOCV profiles after 2C charging in Fig. 4b first show plating at 75% SOC (pink star), and this onset is confirmed by a 0.2% CE decrease from the previous 70% SOC cycle (Fig. S4e).

One advantage of using dOCV for Li detection is that the profiles are remarkably consistent in the absence of Li plating, avoiding false positive plating diagnostics. This characteristic is emphasized further with overlaid dOCV data from all C-rates in the Supplementary Information Fig. S1c, Fig. S3d, and Fig. S4d. In the presence of Li plating, on the other hand, the dOCV curvature varies significantly between cells. Most notably, the dOCV profile after 2C charging to 90% SOC (Fig. 4b, black) is a broad plateau feature that decays for 25 min in contrast with the sharp peaks observed after 4C charging to 40% (Fig. 3b, green) that decay in nearly half the time. We attribute the longer relaxation time at 90% SOC to the smaller potential difference between Li^0 and $Li_{0.9}C_6$ – the driving force for Li chemical intercalation – than the difference between Li^0 and $Li_{0.4}C_6$ for the 40% charge case.

We have carefully considered the impact of electrode aging effects on the Li plating onsets determined from progressive cycling protocols. It is widely recognized that Li plating becomes more favorable with cell aging and higher cell resistances. To keep aging roughly consistent between cells, all fast charging cycles at 2C to 4C were preceded by C/10 formation cycles and 1C baseline cycling to varied SOC cutoffs. The cycling protocol was designed to begin with low SOC cutoff cycles – the least destructive charging conditions – to avoid the possibility that previously nucleated Li promotes plating prematurely on subsequent cycles. Thus, we expect the determined plating onsets to be largely unaffected by aging effects in the measurements presented in Fig. 3 and Fig. 4. The predictive capability of these plating onset experiments is showcased later by cycling repeatedly to various SOC, another verification that this technique provides useful results.

2.3. Quantifying the Li detection limit of dOCV
Lithium plating sensing technology is only suitable for battery control applications if it can reliably detect small, safe quantities of plating. To date, no group has investigated the threshold amount of lithium that must plate to observe the dOCV plating signal. This knowledge gap must be filled before consideration for commercial use.

Coulombic efficiency (CE) analysis is commonly used to identify degradation processes in battery cycling, and we refine a method to use CEs to quantify irreversibly plated Li during fast charge. In our experiments, fast charging occurs at a constant C-rate for specified time to give a known charge capacity, which corresponds to the sum of all graphite intercalation, lithium plating, and solid-electrolyte interphase (SEI) formation processes. The capacity that is subsequently recovered during discharge is thus attributed to any of the charge processes that are reversible, primarily the deintercalation of lithiated graphite or stripping of metallic surface lithium. The ratio of the discharge and charge capacities, the CE, provides information about the reversibility of the graphite reduction reactions during charge.

4

Table 1. Estimating the lithium detection limit of differential OCV

C-rate	Plating onset SOC	Average CE for 1C cycles, no plating	CE at onset, with plating	CIE from plating	Capacity irreversible Li $Q_{Li,irrev}$ (µAh)	Capacity plated Li $Q_{Li,total}$ (µAh)	Li detection limit normalized to $Q_{graphite}$
2C	75%	99.86%	99.59%	0.27%	6.0	20	0.7%
3C	50%	99.94%	99.40%	0.54%	8.0	27	0.9%
4C	30%	99.91%	99.35%	0.56%	5.0	17	0.6%

$Q_{graphite}$ is the graphite electrode capacity determined from C/10 formation cycling, nominally 2.95 mAh

The lithium plating reaction has poor reversibility due to the various fates of plated Li during charge, OCV, or discharge. Plated lithium can react with electrolyte to form organic carbonate salts[36,37] and can lose contact with the graphite particles as it reacts, becoming electrically isolated or 'dead.' Many report that dead Li is the primary culprit for the poor reversibility of the plating reaction[17,38]. Neither the SEI salts nor dead Li can readily be oxidized back to produce Li$^+$ on discharge, so these processes constitute an irreversible Li plating capacity $Q_{Li,irrev}$.

Efficiency losses due to irreversibly plated Li can be estimated by comparing CEs for cycles with and without Li plating. For charging at rates such as 1C that avoid Li plating, the CEs are consistently near 99.9% for charging to different SOC cutoffs (Fig. 3c, grey). For fast-charging rates, however, CEs drop significantly, and this difference from the baseline is reported as a coulombic inefficiency (CIE) due to plating (Eqn. 2). This normalization is important to account for any inefficiencies from SEI formation that are consistent across cycles. The capacity of irreversibly plated Li, $Q_{Li,irrev}$, is then estimated by multiplying the CIE by the total charge capacity Q_{charge} for that cycle (Eqn. 2).

$$CIE(\%)_{plating} = CE(\%)_{no\,plating} - CE(\%)_{with\,plating} \quad (1)$$
$$Q_{Li,irrev} = CIE(\%)_{plating} \cdot Q_{charge} \quad (2)$$

Estimating the total amount of lithium plating $Q_{Li,total}$ from $Q_{Li,irrev}$ requires an assumption about the fraction of plated lithium that is reversible, defined here as η, the lithium recovery factor (Eqn. 3). Other works have reported a lithium plating/stripping efficiency of about 70%[17,32], which refers to the quantity of metallic lithium that is reversibly stripped after intentionally plating on a fully-lithiated electrode. Here we approximate η as 0.7 from those references, but we refer to it as a Li recovery factor instead of a plating/stripping efficiency. This is an important nuance for our experiments because for partially-lithiated graphite electrodes, most plated Li inserts into the graphite during rest and is subsequently deintercalated, not stripped, during discharge. We later verify that 0.7 is a reasonable value for η with a dV/dQ technique.

$$Q_{Li,total} = \frac{Q_{Li,irrev}}{1-\eta} \quad where \quad \eta = 0.7 \quad (3)$$

The above analysis was applied to estimate the Li detection limit of the dOCV technique by estimating the amount of lithium plating present when it was first detected in the onset experiments in Fig. 3 and Fig. 4. The results from this analysis are summarized in Table 1. The $Q_{Li,total}$ values corresponding to each of the detectable dOCV plating onsets are normalized to the graphite electrode capacity and presented in the far-right column. These values on average are below 1%

of the graphite electrode capacity, highlighting that dOCV can reliably detect approximately 4 mAh Li/g graphite active material.

2.4. Using plating SOC onsets to inform charging

Previously, we determined that Li plating begins near 50% SOC for a 3C charge rate under the experimental conditions. Here we use long-term cycling experiments to show that this information can be useful for designing a constant-current charge step that avoids Li plating, which could be useful for constraining the first step in fast charge protocol design[8]. Three Li|Graphitecells were charged at 3C repeatedly either to 30, 40, and 50% SOC with the expectation that the latter exhibit poor performance and signs of Li plating.

The cumulative capacity loss for each cell is shown with respect to the total charge passed during cycling in Fig. 5a. Instead of plotting by cycle number, this analysis adjusts for the varied charge amounts passed to each cell on a given cycle to enable a more direct comparison between the cycling protocols. The capacity loss for 50% cycling is consistently about 4x larger than that of the 40% cycling, while the 30% cycling shows negligible capacity loss. The dOCV profiles throughout the 50% cycling show a growing Li plating signature, confirming that this heightened capacity loss is due to Li plating (Fig. 5b). The Li plating feature is not observed in the dOCV for the 30% and 40% cycling cells (Fig. 5c-d). The dOCV feature growth along with consistent CE decline with cycling (Fig. 5a, inset) support that the nonlinear growth of the capacity loss is due to increased Li plating with cell aging. Plated Li can alter the composition of the SEI, which may increase cell resistances. It can also provide nucleation sites for further plating on subsequent cycles. Finally, accumulated plated Li can block electrolyte ion transport pathways, preventing access to electrode active material. For these reasons, Li plating is expected to increase with cell aging and prior Li plating.
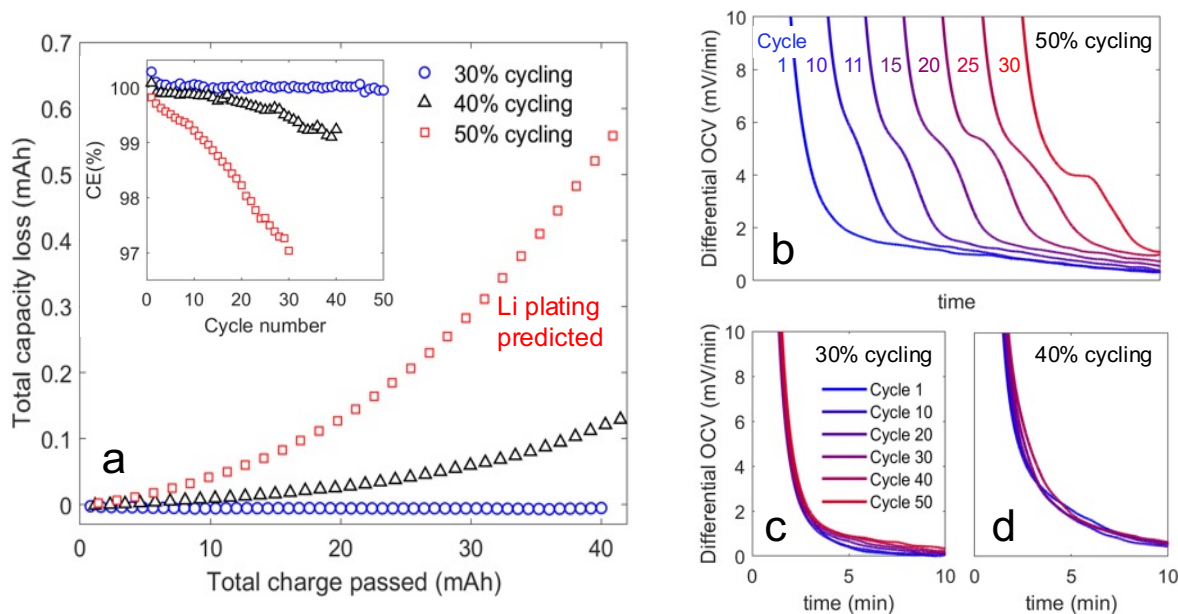
Fig. 5. Long-term 3C cycling designed to avoid Li plating. Three graphite half-cells were cycled repeatedly to 30, 40 and 50% SOC, with plating predicted at 50% from prior dOCV Li onset detection. **a,** The cumulative capacity loss for each cell normalized to the total charge passed. Inset: corresponding coulombic efficiencies throughout cycling. **Right**: dOCV profile evolution throughout cycling to **b,** 50% SOC, offset along x-axis for clarity **c,** 30% SOC and **d,** 40% SOC.

2.5. Detecting the onset of Li plating during cycling

Although Li plating was predicted at 50% SOC from the screening experiment as shown in Fig. 4, the dOCV plating feature for this experiment is not clearly observed until the 11th cycle of 50% charging (Fig. 5b). We attribute this discrepancy to variability between cells and differences in cycling prior to the 50% SOC cycles that could impact electrode aging. The CEs decrease from 99.9% to 99.2% up to Cycle 11, suggesting that the dOCV signal is not observed until then because the amount of plating in Cycles 1-10 may be less than the 4 mAh Li/g graphite detection limit. One unanswered question is whether the capacity loss observed near the end of the 40% cycling is due to Li plating or unrelated degradation processes. The absence of the Li plating dOCV feature suggests the absence of plating, but the amount of plating could be below the detection limit. We plan to investigate this in future work using ex-situ Li quantification techniques[39]. Nevertheless, this cycling data highlights the utility of the dOCV technique to provide real-time feedback about battery aging, which is valuable for control systems and models.

2.6. Direct comparison of dOCV and dV/dQ plating detection

In addition to voltage relaxation (dOCV), another widely reported technique for electrochemical Li detection is differential voltage analysis of the discharge profile (dV/dQ), which detects a plateau feature corresponding to Li stripping – the reverse of the Li plating reaction – and can estimate the amount of plated Li based on the length of the plateau[22,38,40,41]. This technique, however, can give false positive plating signals[41], fail to identify plating when it occurs[41], and requires a constant-current battery discharge immediately following the fast charge, which may be challenging to implement given the fluctuating power demand for vehicles. We assert dOCV as the more commercially feasible analysis but believe it important to understand its detection capabilities relative to dV/dQ.

Few direct comparisons have been provided for dOCV and dV/dQ because the methods have distinct cycling protocols. Relaxation-based techniques require a rest period after charge, whereas dV/dQ must have immediate discharge to maximize the signal corresponding to Li stripping. In Fig. 6a we demonstrate a useful cycling protocol for explicit comparison of dOCV and dV/dQ detection. The cell is cycled progressively at 3C to 35-65% SOC cutoffs to induce varied amounts of Li plating as in Fig 3a, but this time repeating each cycle twice, first with 30 min OCV for dOCV detection (Fig. 6a, solid) and then with 0 min OCV for dV/dQ analysis (dashed). We assume that there is a negligible difference in the amount of plating for repeated cycles, and we support this by showing exceptional agreement of CEs for those cycles in Fig. 6e. A first comparison of the voltage derivatives (Fig. 6b-c) reveals that the qualitative profile shape is remarkably similar for both techniques. The resemblance suggests that the Li depletion mechanism from the surface is similar in both cases. The larger peak height for dV/dQ corresponds to a larger difference in the voltage plateaus during discharge, which are affected by the overpotentials to drive the Li plating and graphite deintercalation reactions. It is also interesting that for the 60-65% cycles with the most Li plating, the dV/dt peaks during discharge (Fig. 6c) appear sharper and have larger amplitude than the peaks from relaxation. This suggests improved peak resolution as a potential advantage of dV/dQ for detecting large quantities of Li plating. While dV/dQ may have useful laboratory applications, performing this analysis in battery control systems as a 'Yes/No' Li sensing technology remains much less likely than dOCV due to the hardware requirements for slow constant-current discharge.
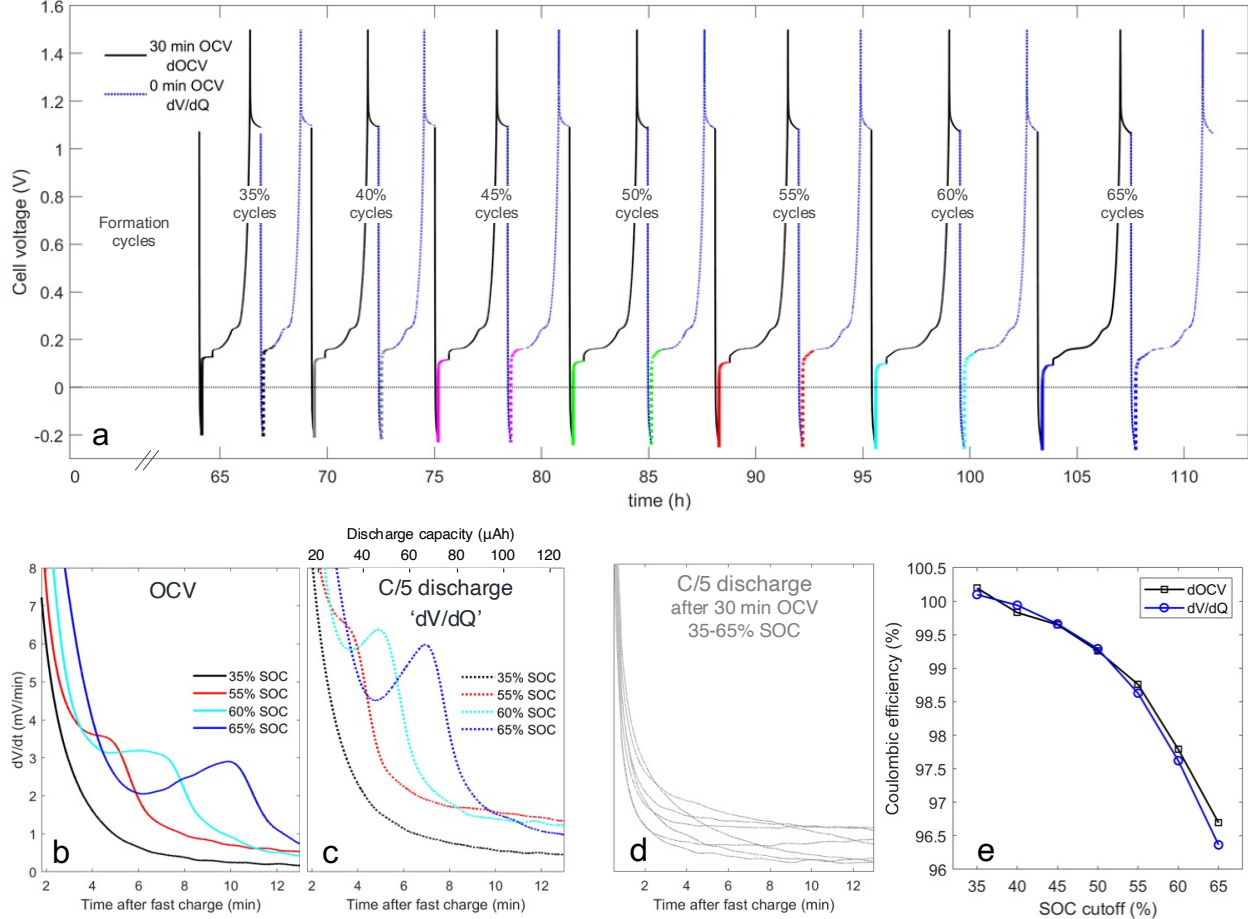
Fig. 6. Direct comparison of dOCV and dV/dQ Li plating detection techniques. a, Cycling protocol to generate dOCV and dV/dQ data for 3C charging to 35-65% graphite SOC. **b,** Differential OCVs extracted from cycling data in (a). **c,** Differential voltage with respect to discharge time, which is analogous to dV/dQ method. **d,** Differential voltages with respect to discharge time for the 30 min OCV cycles, which show no Li stripping peak features due to the chemical intercalation of plated Li during the OCV period. **e,** Coulombic efficiencies for the 30 min (dOCV) and 0 min OCV (dV/dQ) are nearly identical, suggesting the same amount of plating for repeated cycles to the same SOC.

It was our intention to use the dV/dQ peak positions to quantify the capacity of reversible Li plating[22,26,38,41], $Q_{Li,rev}$, and combine that information with CE data to estimate Li stripping efficiencies (SE), the fraction of plated Li that is stripped during discharge. This method, however, yields SE values that decrease systematically from 72% to 50% for the charge cycles ranging 50-65%. We believe that this analysis, discussed in detail in the Supplementary Information Table S1 and Fig. S7, is invalid due to the severe underestimation of plated Li that results from the simultaneous Li stripping and reinsertion into the graphite electrode during discharge. This effect has been observed by other groups, which caution that $Q_{Li,rev}$ estimates decrease when using slower discharge rates after the same amount of Li plating[22,41,25]. The higher temperatures used in this work (23°C vs. ≤ 0°C) appear to exacerbate the effect. Another observation consistent with these statements is that the dV/dQ maxima peak times during discharge (Fig. 6c – 3.3, 4.8, 7.0 min) are similar to the dV/dt peak times during relaxation (Fig. 6b – 4.2, 6.4, 9.9 min), further suggesting that the Li depletion processes present during OCV (Li stripping and reinsertion) still occur at comparable rates during discharge even though a C/5 current is applied. This work highlights the difficulty of experimentally estimating stripping efficiencies on partially-lithiated

graphite, in which Li reinsertion poses a distinct challenge. Future studies to estimate SEs will require new methods that account for or prevent Li reinsertion.

2.7. Methods

Materials. All experiments were performed with Li|Graphitecoin cells (CR2032, MTI Corp) containing 11 mm diameter graphite electrodes and 11 mm diameter Li foil (0.7 mm thickness, MTI Corp). The graphite electrode was prepared at the Argonne National Laboratory CAMP facility with 91.83 wt% Superior Graphite SLC 1506T, 2 wt% Timcal C45 carbon, 6 wt% Kureha 9300 PVDF Binder, 0.17wt% Oxalic Acid on Cu foil (10 μm thick) with a total coating thickness of 70 μm, 38.2% porosity, and approximately 3.0 mAh/cm^2 capacity based on C/10 formation cycling. Punched electrodes were vacuum-dried at 120°C overnight prior to use. Cells contained one Celgard 2500 separator (monolayer polypropylene) and 40 μL 1.2 M lithium hexafluorophosphate (LiPF$_6$) in a 3:7 wt:wt mixture of ethylene carbonate (EC) and ethyl methyl carbonate (EMC), all electrolyte components from Gotion. Electrochemical testing was performed with a Biologic VMP3 potentiostat and an MTI 8-Channel coin cell testing board.

General Experimental. All experiments were performed at 23°C, the measured room temperature.   Each cell underwent 3 formation cycles prior to additional testing, and the deintercalation capacity for the 3rd cycle was used to set the C-rates and state of charge (SOC) cutoffs for subsequent cycling. One formation cycle entails C/10 graphite intercalation to 0.01 V, 30-minute rest, C/5 deintercalation to 1.5 V, and a final 30-minute rest period. We refer to graphite intercalation as 'charging' and deintercalation as 'discharging' for consistency with language used for full-cell commercial lithium-ion batteries, even though the intercalation process is spontaneous in the Li|Graphitehalf-cell configuration. For all cycling experiments, cells are discharged at C/5 to 1.5 V cutoff to ensure fully delithiated graphite (x < 0.01 in Li$_x$C$_6$) at the beginning of each cycle. Coulombic efficiencies (CEs) are calculated from coulomb counting and are defined here as the ratio of the discharge output to the charge capacity, which is specified from the 3rd formation cycle capacity and the present SOC cutoff.

Lithium plating onset determination. To generate voltage relaxation derivative profiles (dOCV) for plating onset experiments, cells were fast charged at different C-rates to varied SOC cutoffs, rested for 30 minutes (OCV period), discharged at C/5, and rested for another 30 minutes before the next cycle. Each cell undergoes 7 charge cycles at each rate, varying the charge capacity within a 30% SOC window at 5% SOC increments in the order of increasing capacity. For example, the cell used to determine the plating onset at 4C in Fig. 3 was charged between 10-40% SOC at 1C, 2C, and 4C for a total of 21 cycles (see Fig. 3a). The first cycle entailed 1C charge to 10% SOC, followed by 1C charge to 15% SOC etc. up to a 1C charge to 40% SOC in cycle 7. This 7-cycle sequence was then repeated at 2C and 4C rates. This 'progressive cycling' begins with a 1C charge rate, when plating is not expected, to further form the cell and provide a baseline of CEs and dOCV profiles in the absence of Li plating. Lowering the charge rate will delay the SOC onset of plating, so plating onset experiments for 3C and 2C rates required cycling to 35-65% SOC and 60-90% SOC respectively (Fig. 4a-b).

Long-term 3C cycling experiments. Three Li|Graphitecells were charged at 3C repeatedly to 30, 40, and 50% SOC with the expectation that the latter exhibit worse performance and signs of Li plating. The cells were cycled 50, 40, and 30 times respectively so that the total charge passed during cycling is approximately consistent between cells, which allows for a fair comparison of absolute capacity loss. The capacity loss for each cycle was calculated from the difference of the

charge and discharge capacities. As with all experiments in this work, cells were discharged at C/5 to 1.5 V. The cells rested at OCV for 30 min between the charge and discharge to collect data for dOCV plating analysis. In addition to the standard 3 C/10 charge formation cycles, this cell was also cycled 3 times at 1C to 80% SOC prior to the 3C cycling for additional SEI formation at higher rates, maintaining a consistent aging effect as with the 1C cycling used in the plating onset experiments.

**Comparing dOCV with dV/dQ plating detection.** Analyzing the discharge profile voltage to detect lithium plating (dV/dQ) requires immediate discharge following charge to avoid the chemical intercalation (CI) of plated Li during rest, which will otherwise reduce the lithium stripping voltage plateau feature and underestimate the extent of Li plating. To directly compare the dV/dQ and dOCV techniques for the same cell and charging conditions, progressive cycling at a 3C rate from 35-65% SOC is applied, as in the plating onset experiments, but with each cycle repeated twice – once with a 30 min rest after discharge for dOCV analysis and a second time with 0 min rest for dV/dQ analysis (Fig. 6a). As with the long-term cycling experiments, this cell was also cycled 3 times at 1C to 80% SOC prior to the 3C cycling for additional SEI formation at higher rates.

Data collection and processing. Voltage data were collected during relaxation every 0.5 s (at 2 Hz) for dOCV analysis and at the same frequency during discharge for dV/dQ analysis. This frequency produces significant noise in the voltage derivatives, which was reduced by using the MATLAB smoothdata() function. The effect of data smoothing on the dOCV peak clarity is illustrated in Fig. S2.

2.8. Supplementary Information
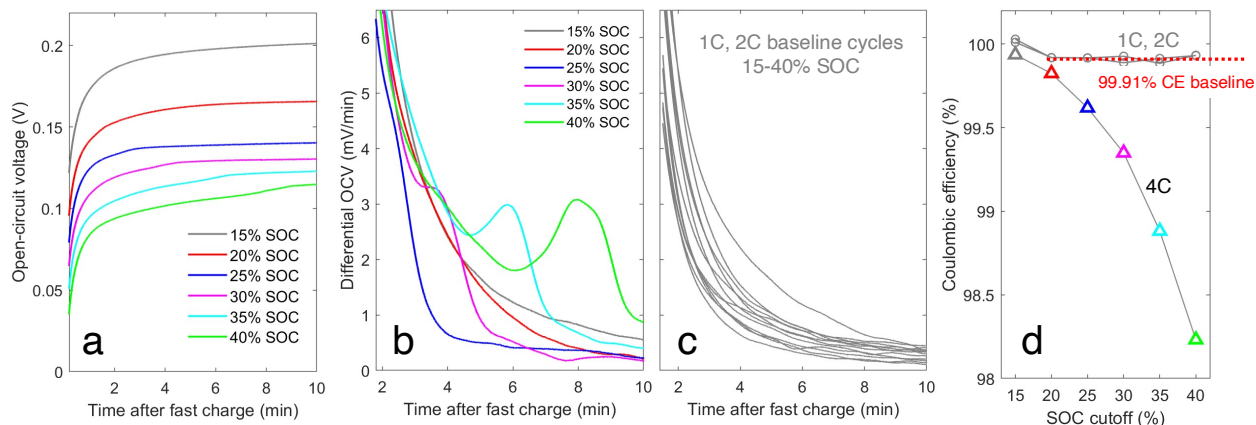
Fig. S1. Detecting the onset of Li plating at 4C in a Li|Graphite cell. a, OCVs after 4C charging. **b,** Differential OCVs from (a). **c,** Differential OCVs after charging to 15-40% SOC at 1C, 2C rates, plotted to show that dOCV does not give false positive plating features at low C-rates. **d,** Coulombic efficiencies for the cycles in Fig. 3 along with CEs from baseline cycles with 1C, 2C charge rates. The 99.91% CE baseline is used for the detection limit analysis in Table **1**.

```
smoothdata(dOCV,'gaussian',n);
```
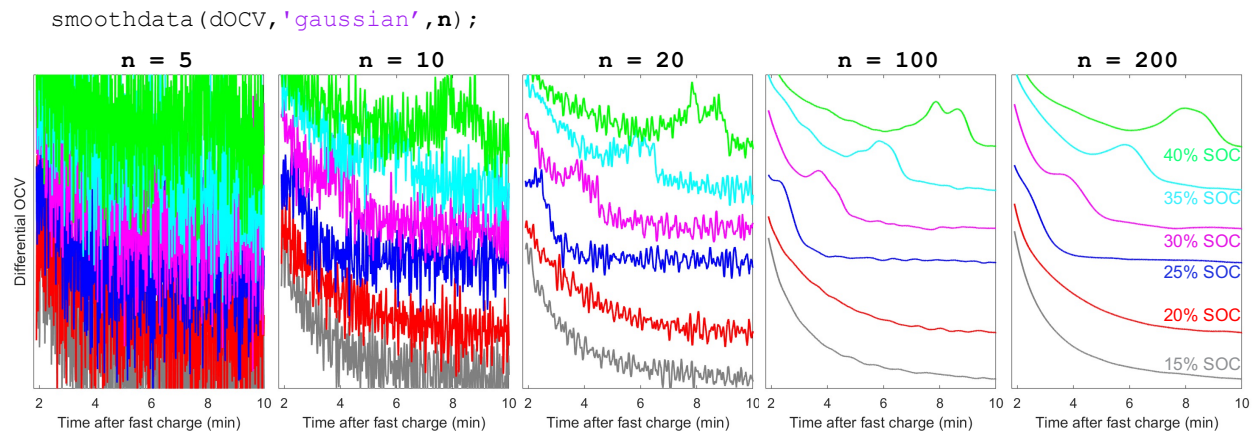

Fig. S2. The effect of data smoothing on dOCV peak clarity. The dOCV profiles from the 4C plating onset experiment of Fig. 3 are plotted with MATLAB's smoothdata() function over varied numbers of data points **n**. The peak feature at 40% SOC (green) observed in the n = 10 window has similar profile shape to the smoothed version in the n = 200 window.
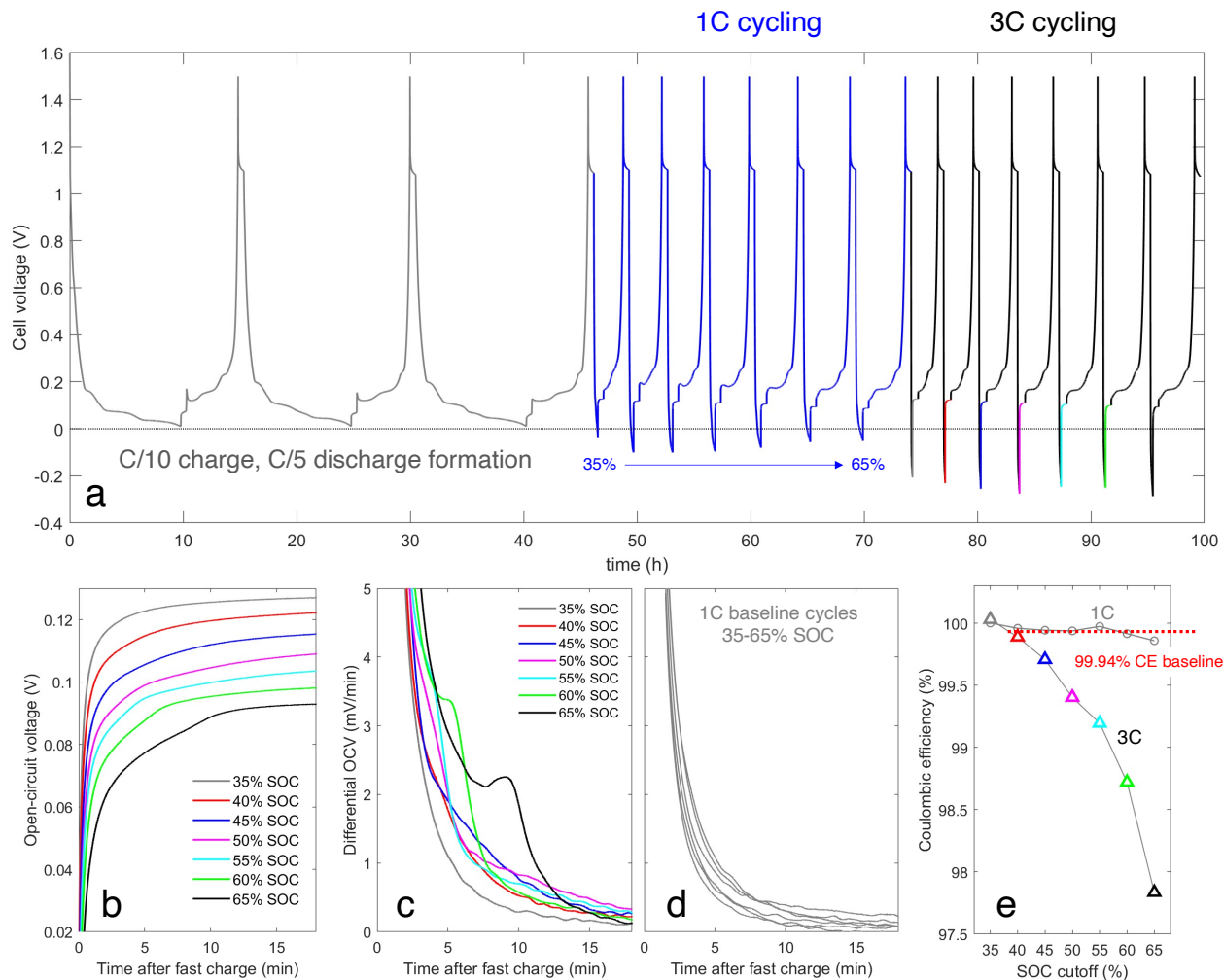
Fig. S3. Detecting the onset of Li plating at 3C in a Li|Graphitecell. a, Complete voltage vs. time data for cycling protocol. **b,** OCVs after 3C charging, extracted from cycling data in (a). **c,** Differential OCVs from (b). **d,** Differential OCVs after charging to 35-65% SOC at 1C, plotted to show that dOCV does not give false positive plating features for this SOC range. **e,** Coulombic efficiencies for the cycles in (a) along with CEs from the 1C baseline cycles. The 99.94% CE baseline is used for the detection limit analysis in Table 1.
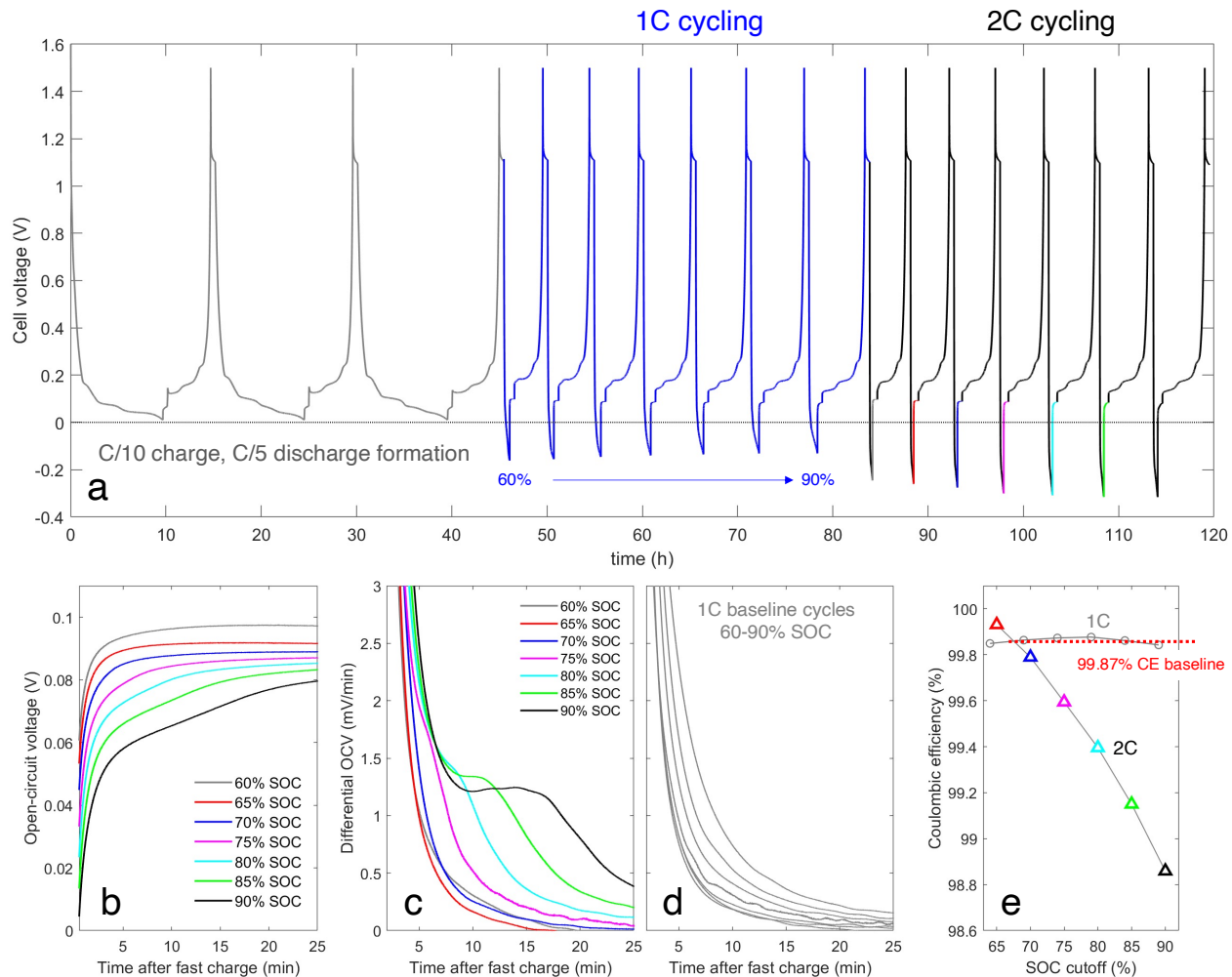
Fig. S4. Detecting the onset of Li plating at 2C in a Li|Graphite cell. a, Complete voltage vs. time data for cycling protocol. **b,** OCVs after 2C charging, extracted from cycling data in (a). **c,** Differential OCVs from (b). **d,** Differential OCVs after charging to 60-90% SOC at 1C, plotted to show that dOCV does not give false positive plating features for this SOC range. **e,** Coulombic efficiencies for the cycles in (a) along with CEs from the 1C baseline cycles. The 99.87% CE baseline is used for the detection limit analysis in in Table 1.
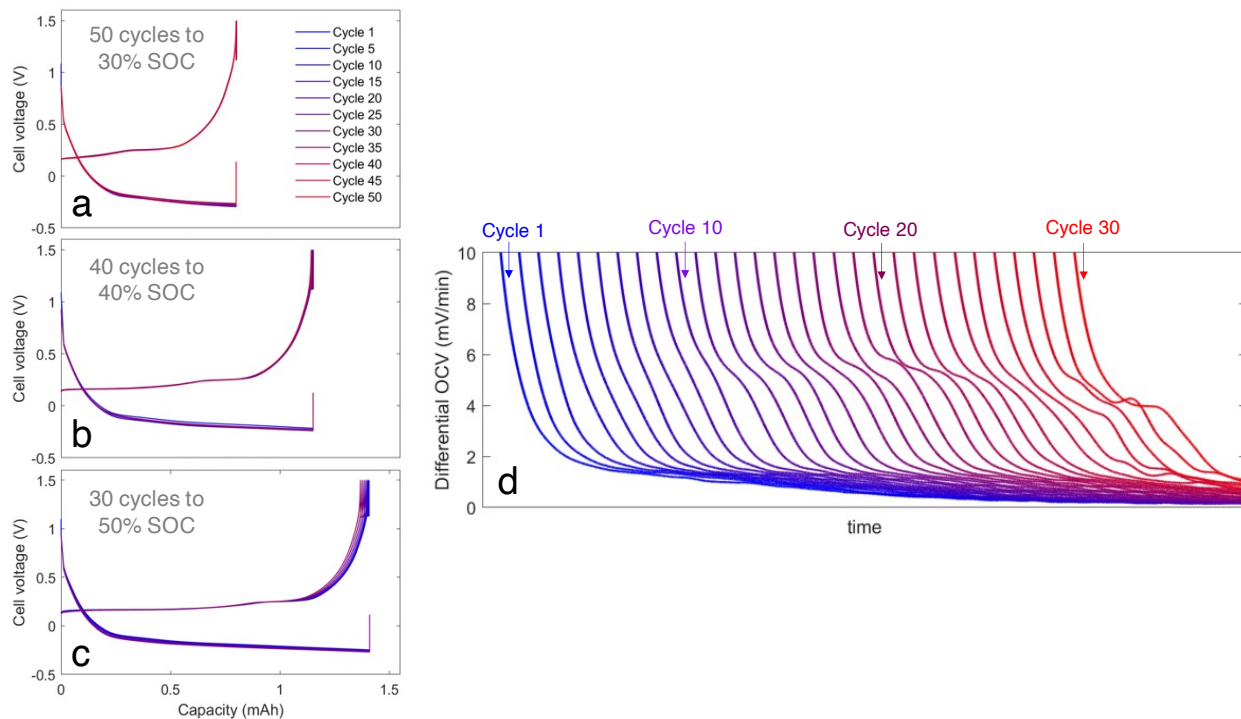
Fig. S5. Long-term cycling voltages and dOCV profiles. Three graphite half-cells were cycled repeatedly to 30, 40 and 50% SOC, and the voltage-capacity data for this cycling is shown in figures a-c respectively. **d,** The dOCV profile evolution throughout cycling to 50% SOC after each of the 30 cycles, complementary to the dOCV for select cycles plotted in Fig. 5b.
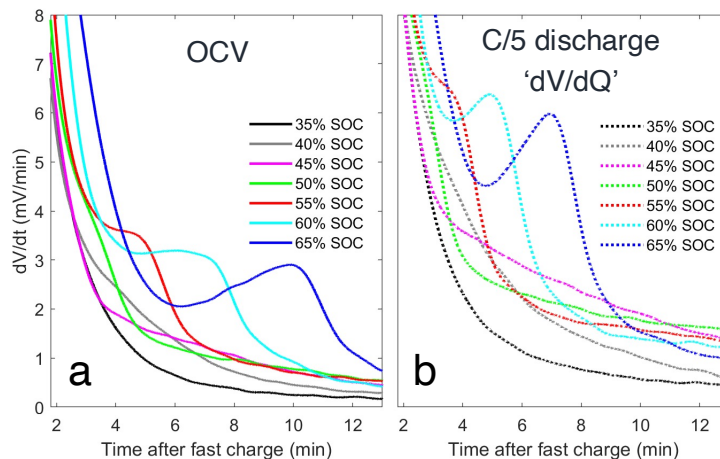
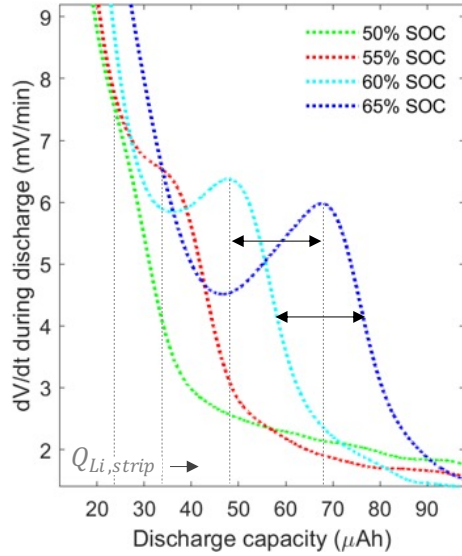**Fig. S6. Direct comparison of dOCV and dV/dQ Li plating detection techniques. a,** Differential OCVs for all 30 min OCV cycles from Fig. 6. **b,** Differential voltages with respect to discharge time for all 0 min OCV cycles, which is analogous to dV/dQ analysis.

Table S1. Estimating Li stripping efficiencies from dV/dQ data

Cycle SOC cutoff (%)	Coulombic efficiency $CE\,(\%)$	Inefficiency from plating, (99.9% - CE) $CIE\,(\%)$	Capacity loss from plating (µAh) $Q_{Li,irrev}$	Capacity to dV/dQ maxima (µAh) $Q_{Li,strip}$	Total Li plating estimate (µAh) $Q_{Li,total}$	Estimated stripping efficiency $SE\,(\%)$
50%	99.29%	0.6%	9	23*	32	72%
55%	98.62%	1.3%	21	34*	55	62%
60%	97.62%	2.3%	40	48	88	55%
65%	96.36%	3.5%	67	68	135	50%

*Estimated peak position

Fig. S7. Selecting dV/dQ maxima to estimate Li stripping capacity $Q_{Li,strip}$. Differential voltages with respect to discharge capacity (dV/dQ) are plotted for all 0 min OCV cycles with plating. For the 60-65% cycles with discernible peaks, the $Q_{Li,strip}$ values correspond to the maxima positions, 48 and 68 µAh respectively. For the 50-55% cycles, the Li stripping to graphite deintercalation transition is estimated by extrapolating the peak position at 60% SOC, noting that the capacity between the 60-65% peaks (↔) is approximately the same as the capacity between the curves (↔) at the dV/dt value of ~4 mV/min.

Table S1 and Fig. S7 highlight an effort to quantify the amount of plated Li stripping $Q_{Li,strip}$ during discharge with dV/dQ and combine the results with coulombic efficiency analysis to estimate Li stripping efficiencies (SE). Others have assumed that plated Li strips preferentially at the applied discharge rate before significant graphite deintercalation begins, with the transition marked by a dV/dQ maximum (in half-cells, minimum in full-cells)[22,26,38,41]. Consequently, the capacity attained prior to the maximum can be used to estimate the amount of plated Li that reversibly strips during discharge $Q_{Li,strip}$. Further assuming that $Q_{Li,strip}$ accounts for all plated Li that is reversibly removed $Q_{Li,rev}$, the total capacity of plated Li $Q_{Li,total}$ can be obtained after $Q_{Li,irrev}$ is determined from CEs (Eqn. S1). The Li stripping efficiency, the fraction of plated Li that is stripped during discharge, thus follows in Eqn. S2.

$$Q_{Li,total} = Q_{Li,irrev} + Q_{Li,rev}\,,\ where\ Q_{Li,rev} \approx Q_{Li,strip}\ \ (S1)$$

$$\frac{Q_{Li,strip}}{Q_{Li,Total}} \cdot 100\% = Li\ stripping\ efficiency\ \ (S2)$$

Li stripping efficiencies obtained with the above analysis are reported in Table S1 for each dV/dQ cycle with plating. The SE values decrease systematically from 72% to 50% as total lithium plating

16

amounts $Q_{Li,total}$ increase. This trend could indicate that dead lithium isolation becomes more favorable for higher quantities of plating. More likely, this trend could be an artefact of increased $Q_{Li,strip}$ underestimation with more plating due to the simultaneous Li stripping and reinsertion into the graphite electrode during discharge. This explanation would be consistent with other groups that have observed $Q_{Li,strip}$ to decrease with slower discharge rates after the same amount of Li plating[22,41]. Considering these effects, we consider the 72% SE value associated with the smallest $Q_{Li,Total}$ to be the most accurate estimate, as it would be the least affected by the underestimation. This value is near the 70% SEs reported from overlithiation studies that we used to estimate the Li recovery factor η in the main text[32]. This is the first attempt to experimentally estimate stripping efficiencies on partially-lithiated graphite, in which Li reinsertion poses a distinct challenge, so more in-depth exploration of SEs will be required in future work.

3. High-throughput Li plating quantification for fast-charging battery design and diagnostics[2]

3.1. Motivation for simple electrochemical techniques to detect Li plating

The urgent need to combat climate change has sparked extreme growth in demand for lithium-ion batteries (LIB). Rapid innovation in battery materials and cell design is critical to meet this demand for diverse applications from electronics to vehicles and utility-scale energy storage. Composite graphite electrodes remain a universal component of the LIB and are expected to dominate anode market share through 2030 despite the introduction of silicon and lithium-based materials[42].

The design space for graphite electrodes is immense, with parameters such as the loading, porosity, particle size, binder composition, and electrolyte being carefully selected to meet requirements for lifetime, operating temperature, charge time, and manufacturing. Regardless of design and application, the lithium plating reaction on graphite is a performance and safety concern due to the formation of non-cyclable 'dead' lithium metal and salts. While recent studies have focused on Li plating during fast charging, the phenomenon is also pertinent to other operating extremes such as low temperature[43], overcharge[44], or system malfunction[45].

Electrochemical (EChem) modeling is an important tool for understanding design tradeoffs that improve graphite performance while avoiding plating. Over decades, Newman-based models that relate cell current density, voltage, temperature, and material properties to graphite intercalation have been enhanced to also estimate lithium plating.[25,26,35,41,46,47] This has led to initial insight into the effect of charge rate, electrode loading, and temperature on lithium plating onset/amount, but simulations rely on debated parameters such as the plating exchange current density or reversibility and are frequently not verified with direct experimental measurements[48] such as Li gas evolution titrations[39,49]. EChem models also have limited ability to predict the chemical compatibility and interphasial properties for novel electrolytes. High-throughput modeling advances for battery materials and interfaces could fill this void, but they too lack commensurate validation[50].

Challenges to high-throughput battery testing can include limited access to expensive equipment, slow multiweek cycling tests, limited material availability, high labor cost of cell assembly, complex analysis methods, and inefficient data handling. There are promising solutions to some of these problems. To conserve newly synthesized electrode materials, it is common practice to determine charge rate capabilities by testing multiple rates on a single cell[51,52]. High-precision coulometers have been developed to improve early performance prediction[53,54]. Data-driven models that predict cycle life from minimal data[3] can be used to quickly optimize charge protocols[8], although large data sets are difficult to obtain in most laboratory settings[55].

Here we demonstrate the power of simple, quantitative, and accessible cycling protocols to inform battery design for Li plating-free charging. The tradeoffs between energy density, charge rate, charge temperature, and lithium plating are experimentally quantified and used to refine mature electrochemical models. We then explore the reversibility of lithium plating under varied fast charging conditions, and apply our understanding towards development of electrolytes and interfaces that limit dead Li formation. We emphasize that the hypotheses and abundant data

---

presented herein were generated primarily with equipment universal to the battery researcher, enabled by strategic data handling, while the sophisticated modeling and titration techniques were reserved for secondary support of the findings.

3.2. Quantifying Li plating accumulation during charge, Li|Graphite cells

Past independent titration studies of Li plating on copper[49] and graphite[39] both show a strong positive correlation between coulombic inefficiency and inactive Li^0, with the majority of the irreversible plating capacity attributed to H_2-evolving dead Li species (Li^0, Li_xC_6) for liquid carbonate-based electrolytes. This observation combined with the high-throughput, precise nature of Li|Graphite cell coulombic efficiency (CE) measurements motivated the protocol in Fig. 7 to estimate irreversible Li plating as a function of charge length. We define irreversible Li as the sum of irreversibly formed species during Li plating such as isolated metallic lithium and Li^+-containing solid-electrolyte interphase (SEI). After formation cycling (see Methods), the 4C charge capacity is increased stepwise by 5% State-of-Charge (SOC), or normalized graphite capacity, for each cycle from 10% to 55% SOC (Fig. 7a). Here we refer to graphite intercalation as 'charge' despite the decreasing cell voltage in the Li|Gr half-cell configuration. We previously demonstrated this 'SOC-sweep' approach to study plating with differential voltage analysis[56], and a similar stepwise capacity cycling has been used for Gr|Cathode full-cells[57], but here we first focus on half-cells due to the stable potential of the Li counter electrode and desire to isolate graphite anode degradation effects.

The CE for each of the cycles is shown vs charge capacity in Fig. 7b. To estimate the irreversible Li, a high-efficiency baseline CE (dashed line) is first assigned to the data points at low SOC, where we attribute the non-unity values to continued SEI formation or slow cell degradation processes rather than Li plating. CE data are then subtracted from these baselines, ranging 99.85-99.98% (see Supplementary Fig. S8-10 and Table S2), to yield a coulombic inefficiency (CIE) from Li plating-related degradation. The CIE multiplied by the SOC for each cycle gives irreversible plating capacities as a percent of each cell's experimental capacity, which are shown in Fig. 7c for various rates, with the result of each cell represented by a set of connected data
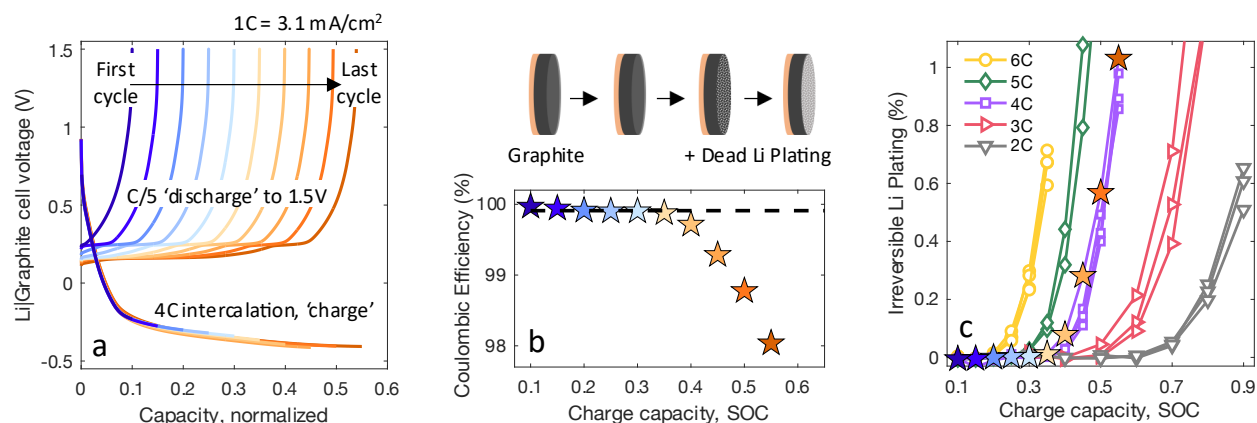
Fig. 7. Determining irreversible Li plating as a function of charge rate and length. **a**, SOC-sweep cycling protocol to test charging performance at 4C to varied states-of-charge. **b**, CEs from the cycling in (a) show a drop around 40% SOC, indicating the accumulation of irreversible Li plating. **c**, The CEs are recast as an irreversible lithium capacity by subtracting all CEs from the high-CE plateau (dashed line) and multiplying the resulting CIE% by the normalized charge capacity. Additional data are overlaid for this condition (3.1 mAh/cm², 25°C) with charge rates of 6C (n=4), 5C (n=2), 4C (n=4), 3C (n=3), and 2C (n=3). For this electrode, 1% is ~31 µAh/cm² but varies with cell capacity ($\bar{x}$ = 3.11, σ = 0.05 mAh/cm²).

19

points. Throughout this work, we point out ways that cycling data, modeling, and titrations further confirm the reliability of CIE for irreversible Li plating quantification. To start, Fig. 7c data reproducibly shows the expected trend of earlier SOC onsets for Li plating as the rate of fast charging is increased from 2C to 6C. Supplementary Fig. S11-12 and Table S3 discuss protocol development, SOC range selection, and control experiments that show minimal cell aging effects for the SOC-sweep method, whereas Fig. S13 supports the link between CIE and irreversible plating.

Increasing the charge temperature is a well-known operating control to avoid lithium plating but, to the best of our knowledge, no work has simultaneously quantified the effects across charge rates (C-rates), loadings, and SOC, all relevant for battery design. Fig. 8a-f shows the irreversible Li plating estimated from the high-throughput SOC-sweep for graphite loadings of 3.1 mAh/cm² (a-c)

Fig. 8. Irreversible Li plating and plating onsets with modeling. a-f, Irreversible lithium averages and standard deviations for rates 2C-6C for graphite loadings of 3.1 mAh/cm² (a-c) and 2.1 mAh/cm² (d-f) at 25°C (a,d), 35°C (b,e), and 45°C (c,f). Data are interpolated with a cubic spline and number of cells n are listed for each condition (see Supplementary Fig. S10). Electrochemical model simulations are in dashed lines and assume 70% plating reversibility. Horizontal lines indicate the threshold used to define the lithium plating onset SOC, 0.05% or 1.0-1.5 µAh/cm² irreversible Li. The inset in (e) illustrates that the onsets are the x-values where the average curves intersect y=0.05%. **g,** Plating onset comparisons of model and experiment for the data in (a)-(f). The experiment error bars in (g)-(h) are calculated from the intersection of y=0.05 with the upper and lower curves bounding each shaded region in (a)-(f). **h,** The data-driven fitting of Eqn. 5 overlaid with experiment plating onsets, generated with parameters α = -0.16 SOC/1C, β = -0.315 SOC/mAh·cm⁻², γ = 0.025 (°C)⁻¹, and ε = 1.70 SOC.

and 2.1 mAh/cm^2 (d-f) at each of 25°C, 35°C, and 45°C. The data points are experimental averages and the shaded regions are constructed from the standard deviations calculated at each SOC; the averaging process is illustrated by comparing Fig. 7c and Fig. 8a. The technique fidelity is supported by experimental trends that are universally consistent with the expectation that the starting SOC of lithium plating should be postponed with decreasing current rates (left to right within panels), decreasing loadings (left to right across panels), and increasing temperature (top to bottom), as seen in shifting irreversible Li curves in the x-direction.

Irreversible Li estimates from a previously reported Newman EChem model[11,35,58,59] are overlaid with experiment in Fig. 8a-f. The lithium plating reaction is modeled using the formulation proposed by Ren et al.[26], with a plating exchange current density of 10 A/m^2 and fixed plating reversibility of 70%, both estimated using titrations and voltage profiles from an experiment with similar Li plating conditions (electrode, charge rate, electrolyte, and Li plating capacities)[39] to the present study. Specific parameters for these electrodes and electrolyte transport properties have been extensively reported and are in Supplementary Table S4 along with experimental and modeled voltage profiles in Supplementary Fig. S14-15. The excellent qualitative agreement in irreversible Li curve shape between model and experiment increases confidence in both the exponential Butler-Volmer kinetic expression used for lithium plating/stripping as well as the assumption that experimental capacity loss is mostly due to irreversible Li instead of other slower degradation processes.

3.3. Mapping plating onsets for varied rate, temperature, and electrode loading

From this dataset we extract the SOC at which irreversible Li starts to form, or 'plating onset', as a metric to inform safe charge durations and assess the quality of our experiment-model agreement. Here we define the plating onset threshold as 0.05% irreversible Li, or 1.0-1.5 μAh/cm^2 for the respective electrode loadings, which is represented by the horizontal lines in Fig. 8a-f. This is the lowest value after which clear plating increases are observed and also avoids uncertainty from experimental noise at low SOC (Fig. 8d, low SOC). The SOCs at which plating begins for all 20 conditions are shown in Fig. 8g. Reasonably linear relationships between onset and C-rate are observed at a given temperature and loading. Additionally, experiment uniquely shows that temperature has nearly double the effect on plating onsets for the higher loading electrodes than lower loading electrodes (3.1 vs. 2.1 mAh/cm^2), as indicated by the larger vertical shift in the curves. Physically, this could mean that for the thin electrodes with onsets above 50% SOC, the accumulation of bulk Li$_1$C$_6$ and its low open-circuit potential throughout the electrode promotes lithium deposition regardless of improved Li transport or intercalation kinetics with temperature. In the thicker electrodes with plating at low SOC, the strong temperature effect suggests that porous electrolyte Li$^+$ transport determines Li plating by controlling the uniformity of graphite lithiation and therefore the SOC at which Li$_1$C$_6$ forms at the graphite|separator interface[11]. These explanations are consistent with optical microscopy that shows Li plating first appears on top of gold-colored Li$_1$C$_6$ particles[60].

Given that the plating onset varies somewhat linearly with changes in other variables, we propose an empirical equation, separate from the physics-derived EChem model, to relate the variables as a step towards data-driven Li plating models. The plating onset SOC, y, is written as a linear function of the C-rate (c), loading (x), and temperature (T), with coefficients α, β, and γ^*

respectively, and intercept ε (Eqn. 4). The (1-y) correction for γ within γ^* was added to account for the variable temperature effect with loading in Fig. 8g, noting that T has a smaller impact for

$$y(c, x, T) = \alpha c + \beta x + \gamma^* T + \varepsilon \quad \text{where } \gamma^* = \gamma (1 - y) \quad (4)$$

$$y(c, x, T) = \frac{\alpha c + \beta x + \gamma T + \varepsilon}{1 + \gamma T} \quad (5)$$

plating onsets at higher onset SOC. Rearrangement to solve for y yields Eqn. 5. Applying the empirical fitting to the 20 [y, c, x, T] plating onset pairs with 4 parameters unsurprisingly gives a much-improved onset prediction compared to the Newman model (Fig. 8h), and nearly 60% reduction in the residual sum of squared errors (SSE). Table 2 highlights the benefits for interpreting the data using an analytically differentiable equation, which can provide heuristics for how Li plating should vary with design parameter changes. Starting from 30°C, 3.1 mAh/cm^2, and 4C rate, for example, a 1C rate increase would cause a 9% SOC earlier plating onset and a 1°C increase would postpone the onset 0.7% SOC. This analysis complements recent work that found a linear correlation between the plating onset and electrode ionic resistance, elucidating the effects of electrode structure and loading[61]. We also investigated the model's predictive capabilities by studying a graphite electrode with identical composition but 3.75 mAh/cm^2 loading, well above the previous experimental range, and observe that it impressively predicts the plating onset within 4% SOC at moderate rates and temperatures (Supplementary Fig. S20). Finally, the equation is useful for visualizing battery design tradeoffs, and Supplementary Fig. S21a shows the charging temperature required to avoid plating for a constant-current (CC) charge to 40% SOC for various combinations of rates and loadings. Additional visualizations of the empirical fitting and a discussion of its limitations are in Supplementary Fig. S21b-d and Supplementary Note 1.

Table 2. Quantifying parameter effects on the plating onset SOC

Empirical Expression	Values at base conditions[†]
$\left(\dfrac{\partial y}{\partial c}\right)_{x,T} = \dfrac{\alpha}{1 + \gamma T}$	-9 % SOC/1C
$\left(\dfrac{\partial y}{\partial x}\right)_{T,c} = \dfrac{\beta}{1 + \gamma T}$	-18 % SOC/(mAh·cm^{-2})
$\left(\dfrac{\partial y}{\partial T}\right)_{c,x} = \dfrac{\gamma}{1 + \gamma T}(1 - y)$	0.7 % SOC/1°C

†Partial derivatives of Equation 5 are evaluated at 30°C, 3.0 mAh/cm^2, and 4C with fitted parameters reported in the Fig. 8h caption.

22

3.4. Designing electrolytes for improved plating reversibility

Lithium plating is harmful because the reaction is poorly reversible, which causes loss of cell lithium inventory, capacity fade, and accumulation of reactive metallic lithium. While the impact of electrolyte on reversibility is at the forefront of Li metal battery research[62], few have considered electrolyte engineering as a plating control strategy for graphite anodes under fast charging. If the reversibility of plating could be improved from 70% to 90%, for example, then the amount of irreversible plating would be decreased by a factor of 3 (30% to 10%), drastically reducing the impact on performance and safety. In this section, we quantify irreversible Li for different electrolytes using the SOC-sweep of Fig. 7, demonstrate a rigorous method to estimate plating reversibility on graphite, and argue that plating reversibility is an important electrolyte design criteria for fast charging.

Fig. 9a shows the effect of swapping ethylene carbonate (EC) for varied weight percent (wt%) fluoroethylene carbonate (FEC) on irreversible plating. These compositions were inspired by Li metal battery studies that repeatedly show FEC can decrease dead Li formation[49,63]. The notable shift in the curve from 0% to 5% FEC indicates a delayed onset of lithium plating, and the decreasing slopes with increasing FEC suggest a beneficial concentration effect for reducing dead Li. This observation arises despite decreasing bulk electrolyte conductivity with increasing FEC (Supplementary Fig. S22), which led us to hypothesize that enhanced interfacial properties or fractional plating reversibility may alternatively explain this result.

To systematically explore whether Li plating reversibility plays a role in improved performance with FEC, we sought a rigorous high throughput method to quantify the value at conditions relevant to fast charging. The estimation of plating reversibility on graphite at standard SOC (below 100%) and ambient temperatures is challenging due to the rapid dissolution of reversible Li deposits that supports Li^+ re-intercalation into the graphite.[23,60,64] A workaround to this is to study plating during graphite overcharge (above 100% SOC)[17,32], which has also emerged in the context of hybrid graphite/lithium anodes[65–67], but reversibility estimates have only been reported at low current rates (< 0.5C) and/or are deduced from qualitative voltage plateau transitions.

The framework we apply to carefully and efficiently estimate the reversibility of Li plating (η) on graphite during fast charge is summarized in Fig. 9b. After formation cycling, the first step is to estimate the coulombic efficiency for graphite intercalation (CE$_{int}$) without lithium plating (Fig. 9b 'Baseline Cycle', value ~99.7% see Table S5, Fig. S23). Next, that same cycle is repeated with an added overcharge step to induce a known capacity of lithium plating, P. The capacity lost due to lithium plating is then isolated by subtracting the baseline capacity loss of intercalation from the total irreversible capacity from the overcharge cycle (Q$_{irrev}$, Fig. 9b), which allows the calculation of η from Equation 6. Repeating the overcharge cycle 4x on the same cell gives reproducible calculated reversibility values for the first three overcharge cycles, increasing confidence in the method and allowing error bar estimation with a single cell (see Fig. S24).

$$P(1 - \eta) = Q_{irrev} - (1 - CE_{int})Q_{int} \quad (6)$$

Fig. 9c shows the calculated lithium plating reversibility for various FEC-containing electrolytes when the overcharge amount is varied at a fixed 4C rate (left) and the deposition rate is varied at
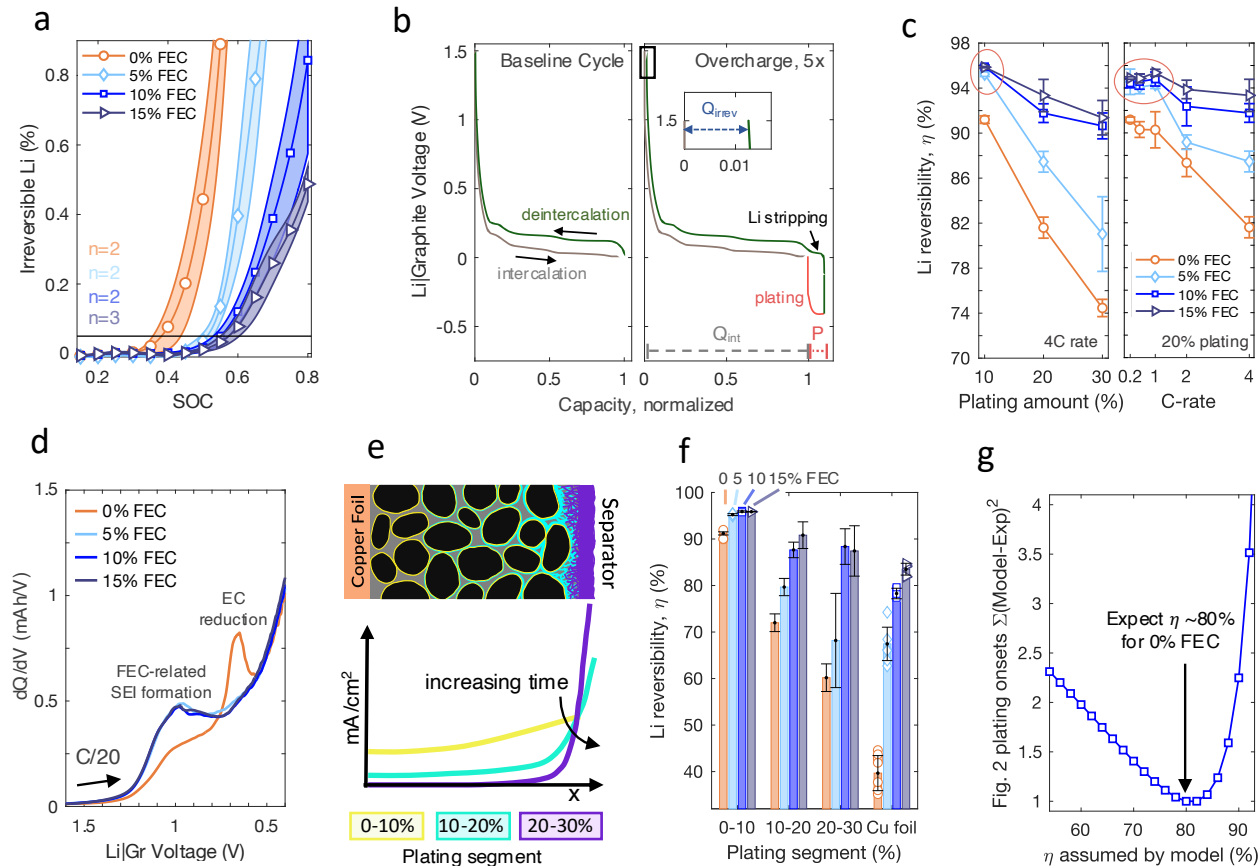
Fig. 9. Electrolyte engineering to reduce irreversible Li plating. **a**, Irreversible Li in Li|Graphite cells using the Fig. 7 protocol for varied weight percent (X) FEC in 1.2 M $LiPF_6$ electrolyte, resulting in FEC:EC:EMC wt% ratios of X:(30-X):70. Conditions: 4C rate, 3.1 mAh/cm^2, 25°C. **b**, Overcharge protocol to rigorously determine the lithium plating reversibility for high-rate plating. The intercalation capacity (Q_{int}), plating capacity (P), and overcharge irreversible capacity (Q_{irrev}) are used in Equation 6 to calculate the reversibility. See Methods for additional protocol details. **c**, Li reversibility varying the amount of 4C plating (left) and varying C-rate (right) for 20% plating, where 10% is 0.31 mAh/cm^2. Error bars represent standard deviation for n=3 cycles on the same coin cell. **d**, Differential capacity curves from the first graphite lithiation at C/20 rate. **e**, Temporospatial schematic of Li plating location during 30% overcharge and sketch of associated Li plating current densities. **f,** Plating reversibility by each segment in (e) for each electrolyte composition, calculated from data in (c), compared with reversibility for the same plating capacity and rate on copper foil. Error bars for 10-20% and 20-30% are estimated with uncertainty propagation (Supplementary Fig. S24). **g,** The sum of squared errors (SSE) for Li plating onsets from experiment and the electrochemical model (Fig. 8g) across all conditions vs. the plating reversibility assumed by the model.

20% overcharge (right). The plating overcharge amount is defined as the percentage of total graphite capacity (here, 3.1 mAh/cm^2) that the electrode is charged beyond complete lithiation. For all conditions, FEC-free electrolyte exhibits the lowest η, ranging between 74-91%, and for all electrolytes, the expected trends of decreasing η with increasing plating amount and rate are apparent. The beneficial concentration effect in FEC-containing electrolytes from Fig. 9a is again observed with the exception of low-rate or low-amount conditions, circled in Fig. 9c. We ascribe this observation to plating occurring primarily beneath the graphite SEI[68], which we believe has similar composition across concentrations due to overlapping differential capacity curves during the first graphite intercalation (Fig. 9d) when the majority of SEI is formed.

Finally, we try to connect these η determined from overcharge experiments to the true η range observed during fast charging. In the latter, plated lithium is observed within microns of the

graphite/separator interface[10,58] due to developed concentration and potential gradients, but the overcharge protocol differs because it begins without gradients and thus should initially yield more uniform Li deposition, as imaged at low rates[66]. Consequently, Fig. 9e is a sketch of how lithium plating likely accumulates during 4C overcharge, a hypothesis consistent with intuition about gradient development, effective porosity decreasing as Li deposits grow, and the observed decrease in η with plating amount as these effects lead to higher local current densities and non-uniform deposits near the separator interface. To better understand the effect of location on η, an incremental plating reversibility $\Delta\eta$ for each subsequent 10% of plating is calculated directly from data in Fig. 9c (see Methods) and shown in Fig. 9f.

An interesting feature arising from this analysis is that for 30% overcharge, the reversibility for the final segment of plating $\Delta\eta_{20-30}$ is drastically lower for the 0 and 5% FEC electrolytes, suggesting that the η for the 10% overcharge experiment, equivalent to $\Delta\eta_{0-10}$, is artificially high due to uniform plating deposition throughout the electrode. The 10-15% FEC samples, in comparison, show less performance decline with plating amount, perhaps due to bulk electrolyte effects such as enhanced Li^+ solvation by FEC[69]. As depicted by the Fig. 9e diagram, this last plating segment may occur in a planar manner after protruding through the graphite SEI, with growth constrained by the separator. Thus, we might expect comparable reversibility for Li plating on a planar substrate such as copper foil, and indeed similar trends are observed using identical plating amounts and current densities (Fig. 9f, see Fig. S25 for details).

Despite the illustrative range of possible plating reversibilities, it remains unclear which is most representative of plating under standard charging conditions, i.e. which can best predict irreversible Li with models or quantify electrolyte improvements. Leveraging our comprehensive experimental and modeling datasets for the 0% FEC electrolyte, we determine the single η that minimizes the plating onsets error across all conditions (Fig. 9g, Supplementary Fig. S17-18). The η from this analysis is 80%, but most importantly, the SSE divergence above 90% provides strong evidence that the plating reversibility does not exceed this value in practice, highlighting the need for careful interpretation of overcharge plating data. Looking at 0% FEC data in Fig. 9f, η=80% is between the values for $\Delta\eta_{0-10}$ and $\Delta\eta_{10-20}$, suggesting that – if an average of the $\Delta\eta_{0-10}$ and $\Delta\eta_{10-20}$ values are representative of true plating reversibility – this electrolyte would produce 2-3x as much irreversible lithium (1-η) compared with the FEC electrolytes (for 5-15% FEC, average $\Delta\eta$ are 88-93%). Holistically, this evidence suggests that η is an important electrolyte/interphasial design property for systems susceptible to Li plating. Going forward, we expect the technique of Fig. 9b to be useful for characterizing additional electrolytes and assessing innovative methods to mitigate irreversible plating such as separator design[70].

3.5. Electrolyte testing in Graphite|NMC532 full-cells with titration

This section first shows that previous half-cell plating onset and electrolyte studies are valuable for informing commercial full-cell design, which instead use a porous, high-voltage cathode material with limited lithium inventory. Next, ex-situ titrations are used to verify Li plating and identify cycling data features from full-cells that are quantitative predictors of plating. Finally, the insights are applied to design a validated, highly sensitive, in-situ method for Li plating quantification.

To compare lithium plating behavior across electrolyte compositions, a Graphite|LiNi$_{0.5}$Mn$_{0.3}$Co$_{0.2}$O$_2$ (NMC532) was cycled 140 times, alternating 5 moderate 1C CCCV (constant current constant voltage) charging cycles to 4.2V, holding until C/5 current, with 2 6C CCCV fast charging cycles to 4.2V, holding until 80% capacity. We selected this protocol to help isolate fast charging-related capacity loss, expected only during the 6C cycles, from other cell aging effects such as FEC degradation[71]. Fig. 10a shows that the 5-15% FEC full-cells, similar to half-cells, outperform the FEC-free electrolyte, undergoing on average only about 30% of the capacity fade over the 100 1C cycles, with similar 6C CCCV charge times compared to 0% FEC (Supplementary Fig. S26-27). The 2% FEC electrolyte, included for the common use of FEC as an additive, performed only slightly worse than the higher concentrations. From our Li reversibility analysis, the lack of a clear concentration effect on performance may indicate small amounts of plating occurring mostly beneath the FEC-derived SEI. It may also indicate the importance of SEI in delaying the plating onset SOC, which is seen in Fig. 9a and suggested by others[72] to explain better rate performance with an artificial graphite SEI coating. Significant sample variability is expected due to the heterogeneous nature of lithium plating and is depicted by the representative error bars obtained from replicate trials on multiple cells.

We then use the cycling data to quantify degradation from fast charging and compare results with Li titrations of the extracted electrodes. Others have reported that irreversibly plated lithium is linearly correlated to cell capacity loss[73], so we expect the abrupt capacity changes after the 6C cycles (Fig. 10a, box) to correlate with titrated Li capacity from mass spectrometry titration (MST). MST[39] accurately quantifies the combined H$_2$-evolving species on graphite such as isolated 'dead' Li^0 and inactive Li$_x$C$_6$ with exceptional resolution (see Methods, Supplementary Fig. S28-Fig. S30). However, the titrated Li slightly exceeds the capacity loss for most of the 0% FEC samples despite controls that show minimal Li$_x$C$_6$ contribution, suggesting that plating is not fully quantified by this metric (Supplementary Fig. S32-33). The source of this error may be visualized
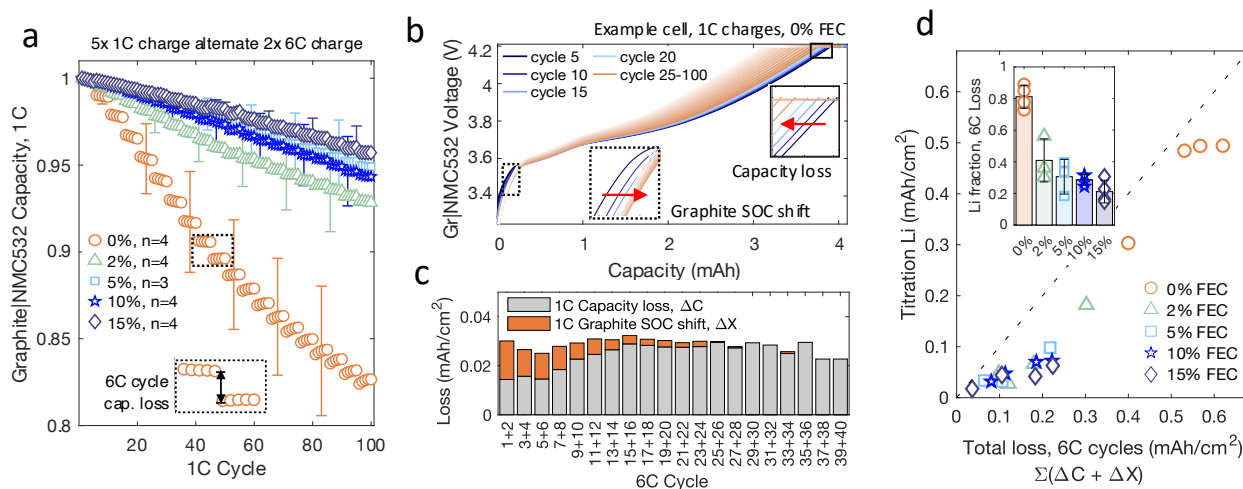
Fig. 10. Full-cells electrolyte testing with dead Li estimation and titration a, Graphite|NMC532 1C discharge capacity normalized to the initial (Cycle 1) value vs. cycle number, with cells undergoing two cycles of 6C CCCV to 4.2V charging to 80% SOC after five 1C cycles. The inset emphasizes capacity jumps between groups of 1C cycles due to the intermittent 6C cycles that induce Li plating. Error bars depict standard deviations across n cells. **b,** Representative 1C charging profiles throughout cycling. Insets show how the profile shifts during cycling, and phenomena associated with the shifts. **c,** Loss quantified from capacity change and graphite SOC shift. The data for 6C Cycles 1+2 is determined by analyzing 1C Cycles 3-5 (before 6C) and 7 (after, see Methods for details). **d,** Titrated Li (Li^0 and Li$_x$C$_6$) vs. the sum of the data in (c) for all cells tested in (a). The inset shows the fraction of the estimated loss accounted for by titrated Li, the position of each point relative to the dotted parity line.

in the 1C charging profiles for a representative cell in Fig. 10b, recalling that 1C cycle 5 is followed by 6C cycles 1 and 2 then 1C cycle 6, and that 1C cycle 10 is followed by 6C cycles 3 and 4, and so forth.

The profiles show that for the first few fast charging cycles, the voltage segment corresponding to early graphite lithiation shifts to the right (dashed box). Physically, the shift indicates a change in the electrode potential windows during charge and the removal of additional cyclable lithium[7] from the graphite to compensate lithium losses from plating. Thus, we believe this graphite SOC shift should estimate losses not captured by the 1C capacity loss, which conversely manifests by the high-voltage capacity shifting to the left (solid box).

The SOC shift (ΔX) and capacity loss (ΔC) are reported for each pair of 6C fast charging cycles in Fig. 10c (see Methods for detailed calculation, Supplementary Fig. S34-35). The combined loss for each pair of cycles is about the same, which is reasonable because i) the amount of loss per pair is small, ~1% of the total capacity, and ii) the cell aging that might promote increased plating over time is counterbalanced by increasing CCCV charge times, which lowers the average C-rate (Supplementary Fig. S26-27). The graphite SOC shift contribution decreases from about 50% of losses for 6C Cycles 1-2 to ~0% for Cycles 25-26 and beyond as the residual lithium in the graphite is consumed, highlighting the importance of this metric for accurate early plating quantification. Supplementary Fig. S36 shows Fig. 10c for all cells, an impressive visualization that indicates accurate loss quantification with single cycle resolution.

Fig. 10c shows significantly less titrated Li for the FEC electrolyte cells compared to the 0% FEC cells, as anticipated from Fig. 9 and Fig. 10a electrochemical measurements and electrode images (Supplementary Fig. S37). There is also a strong correlation between the sum of the 6C losses (from Fig. 10c) and titrated Li. For the 0% FEC electrolyte, the fraction of the loss accounted for by titrated Li is about 81% (Fig. 10d inset), comparable to other studies of dead Li using similar electrolytes[39,49]. This leads us to suspect that the majority of the 6C losses are indeed due to irreversible Li plating but note that this metric may include losses from other fast-charging degradation such as SEI formation or electrode active material loss. The Li fraction with FEC is lower and decreases slightly from about 40% to 20% with increasing concentration, again highlighting the potential FEC advantage for avoiding metallic Li buildup during cell malfunction. Still, these values are notably higher than the ~10% fractional dead Li that others have observed for slow Li deposition on Cu for similar FEC electrolytes[49,63,74], emphasizing phenomena unique to fast charging and the need to understand loss mechanisms besides dead Li formation.

3.6. Quantifying Li plating accumulation during charge, Graphite|NMC532 cells

Finally, the titration results unveil a route for estimating irreversible Li as a function of SOC in full-cells to allow direct comparison with half-cell results. The combined 1C capacity loss and 1C graphite SOC shift ($\Delta C + \Delta X$) was a strong predictor for titrated Li for the 0% FEC electrolyte, so we then designed a protocol alternating two 1C charge cycles with two fast charging cycles to X% SOC, where X is increased by 5% for each iteration (Fig. 11a, Supplementary Fig. S38). Two cycles of each step were performed to benefit the technique sensitivity and reliability (see Supplementary Fig. S39-40). The 1C capacity changes between fast charging steps (ΔC) correspond to losses from only those X% SOC cycles. Similarly, the 1C graphite SOC shift (ΔX) is calculated for each X% SOC fast charge step, and the combined loss is shown in the bottom of Fig. 11a, as in our previous analysis. This metric is shown for representative cells at various C-
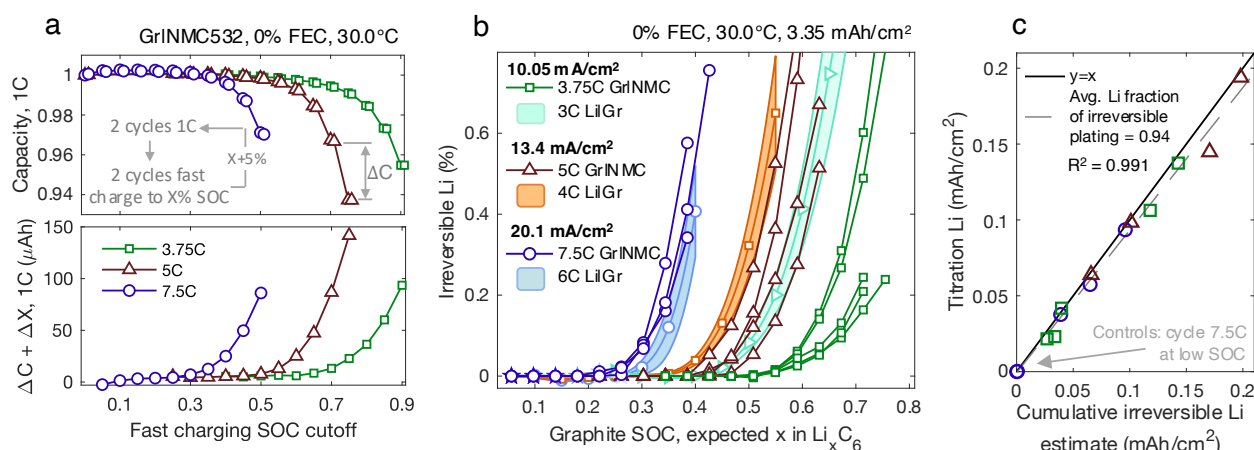
Fig. 11. Determining irreversible Li in full-cells, comparison with half-cells, and titration validation. a, Characterizing irreversible Li in full-cells by monitoring the normalized 1C discharge capacity with intermittent 2 cycles of constant-current fast charging to progressively higher SOC. The sum of capacity loss (ΔC) and graphite SOC shift (ΔX) from each set of fast charge cycles is shown and used to calculate the irreversible Li (see Methods). **b,** Comparing irreversible lithium on graphite with NMC (connected points, individual cells) and Li (shaded regions, averaged 3 cells) counter electrodes as a function of the expected graphite lithiation at the end of charge (graphite SOC). The full-cell SOC, the x-axis of (a), is converted to graphite lithiation as described in the Methods. The Gr|NMC532 C-rates were selected to fix the average geometric current densities experienced by graphite (10.05, 13.4, 20.1 mA/cm²) across cell formats, see Supplementary Note 7. **c,** Titrated Li vs the total irreversible Li plating estimates for the graphite electrodes extracted from the Gr|NMC532 cells in (b).

rates, and the x-axis denotes the SOC cutoff of the previous 2 fast charge cycles that are analyzed. For the full-cells, the rates and SOC are defined with respect to the nominal 3-4.2V C/10 charge capacity, and were selected so that identical graphite current densities are applied for comparison with 3C to 6C rates in the half-cells (see Supplementary Note 2).

We then transform the data in Fig. 11a to estimate irreversible Li plating in full-cells and provide a direct comparison with the half-cells in Fig. 11b. The transformation entails i) subtracting baseline losses observed for fast charging at low SOC prior to the plating onset, as in Fig. 7b (Supplementary Fig. S41-43), ii) normalizing the loss to the active graphite capacity, as in Fig. 7c, and dividing by 2 to account for 2 cycles to each SOC, and iii) converting the x-axis from full-cell SOC to graphite lithiation (avg. x in Li_xC_6) by differential voltage profile analysis (see Supplementary Fig. S44). We assume that 100% of the baselined ΔC+ΔX data corresponds to irreversible Li plating capacity. A striking similarity is the shape of the Li|Gr and Gr|NMC curves, which extends our hypothesis from Supplementary Fig. S19 of universal physics for Li plating regardless of counter electrode selection. Another interesting observation is that the spacing of the Li|Gr curves have a similar C-rate dependence as those of the Gr|NMC, which reveals a route for empirically scaling the half-cell data to predict full-cell behavior with limited full-cell measurements (Supplementary Fig. S45). Even without this adjustment, however, the half-cells show average Li plating onset SOC (defined again as 0.05% irreversible Li) within 3% of full-cells for the 20.1 mA/cm² rate and within 6% for 13.4 mA/cm², suggesting the Fig. 8a-b Li|Gr measurements at the higher current densities (4C and above) are the most translatable for full-cells. We also offer some physical explanations for the plating onset differences based on prior modeling in Supplementary Note 3.

As the final step of technique verification, the graphite electrodes were titrated for comparison with the cumulative irreversible Li estimated for each cell (Fig. 11c), determined by summation of the $\Delta C + \Delta X$ values of Fig. 11a for each curve after the described baselining. The strong linear correlation ($R^2 = 0.991$) with near unity slope further suggests that the method accurately predicts plating amounts and estimates that, on average, 94% of irreversible Li plating exists in the form of electrically isolated Li^0 and other titration Li, with the remaining 6% as Li^+-containing SEI species. The application of this protocol for electrolyte engineering in full-cells should be investigated in future works, but we note that this 1.2 M $LiPF_6$ in 3:7 EC:EMC electrolyte offers favorable Li detection properties and is well-suited for immediate subsequent studies. One application is to quantify the sensitivity of proposed onboard plating detection technologies such as cell pressure monitoring[48]. Another is to quantify the effects of electrode porosity, loading, temperature, composition, and heterogeneity on Li plating to inform cell manufacturing.

3.7. Methods

Materials. Electrolytes were made with ethyl methyl carbonate (EMC), ethylene carbonate (EC), fluoroethylene carbonate (FEC), and lithium hexafluorophosphate (LiPF$_6$) from Gotion Inc and used within a week of preparation. Composite graphite electrodes were obtained from the Argonne National Laboratory CAMP facility with 91.83 wt% Superior Graphite SLC 1506T, 2 wt% Timcal C45 carbon, 6 wt% Kureha 9300 PVDF binder, 0.17 wt% Oxalic Acid on Cu foil (10 μm). Various combinations of [thickness, loading, porosity] were used based on application and availability, A1 = [47 μm, 2.1 mAh cm^{-2}, 37.4%], A2 = [70 μm, 3.1 mAh cm^{-2}, 38.2%], A3 = [70 μm, 3.35 mAh cm^{-2}, 34.4%], A4 = [85 μm, 3.75 mAh cm^{-2}, 35.4%]. Plating onset and temperature experiments (Fig. 7, Fig**. 8**) used anodes A1 and A2. Plating reversibility experiments (Fig. 9) used A2. Full-cell plating experiments and Full-cell/half-cell validation (Fig. 10, Fig. 11) used A3. Empirical fit prediction testing (Fig. S20) used A4. The composite LiNi$_{0.5}$Mn$_{0.3}$Co$_{0.2}$O$_2$ cathode was 90 wt% Toda NMC532, 5 wt% Timcal C45 carbon, 5 wt% Solvay 5130 PVDF binder, with 2.8 mAh cm^{-2} and targeted P:N ratio 1:1.2 with anodes A2-A3, 71 μm coating on 20 μm Al foil, 35.6% porosity. All electrodes were dried at 120°C under vacuum overnight before transferring directly to the glovebox.

Hohsen CR2032 coin cells were used for all experiments, with 30 μL total electrolyte added quickly in 3 separate 10 μL aliquots to ensure uniform wetting while avoiding evaporation. Graphite electrodes were 15 mm diameter punches, paired with either 14 mm dia. Li foil (0.7 mm thickness, MTI Corp) or 14 mm dia. NMC and separated by a single 18 mm dia. Celgard 2500 separator (25 μm monolayer polypropylene). The molar ratio of Li:Gr in half-cells is greater than 30:1 for all loadings (see Supplementary Note 4). All assembly/disassembly was performed in an argon-filled glovebox with O$_2$ < 1.0 ppm, H$_2$O < 0.5 ppm. Electrochemical testing used Biologic MPG-200, VMP3, and BCS-810 potentiostats with CCH-8 coin cell holders at temperature control in Thermotron environmental chambers. Coin-cell temperature rise from the chamber setpoint is expected to be minimal (< 5 ºC) during cycling (see Supplementary Note 5). Cycling protocols were implemented with Biologic's EC-Lab software.

SOC-sweep testing for Li|Graphite cells (Fig. 7, Fig. 8, Fig. 9a, Fig. S20). One slow formation cycle entails C/10 intercalation to 0.01 V and C/5 deintercalation to 1.5 V with 5-minute rest between each step. The experimental graphite capacity is determined from the discharge capacity of the 3rd and final C/10 formation cycle and used to set the C-rates and SOC cutoffs for subsequent cycling. We refer to graphite intercalation as 'charging' and deintercalation as 'discharging' for consistency with language used for full-cell commercial lithium-ion batteries, even though the intercalation process is spontaneous in the Li|Graphite cell configuration. Next, each cell underwent 5 fast formation cycles of 4C charge to 10% SOC and C/5 discharge to 1.5V with 15-minute rest between current steps (see Fig. S11). Last, the cell undergoes the SOC-sweep cycling in which the charge capacity is increased 5-10% SOC for each subsequent cycle, with each charge step alternated with C/5 discharge to 1.5V, and a 30-minute rest between current steps. The SOC window and step size was selected based on the expected plating onset SOC; for later expected onsets, a step size of 10% was selected to cover large SOC range while minimizing experiment time (see Table S3). For high-temperature experiments, the oven temperature was increased from 25°C to the target temperature during the 5 fast charging formation cycles. For Fig. 9a comparing electrolyte compositions, the first formation cycle used C/20 instead of C/10 to clearly articulate

dQ/dV features, seen in Fig. 9d. Typically 3 cells were run initially at each condition in Fig. 7, Fig. 8, Fig. 9a, and Fig. S20, but the number of cells reported varies between 2 and 5 (e.g., see Fig. 8a-f, bottom left of each panel). An additional set of 2-3 cells may have been run for better data statistics or to make up for data that was excluded due to indicators of poor cell performance resulting from imperfections in manual cell preparation. For a description of such 'bad cells,' see Fig. S10.

Electrochemical Modeling (Fig. 8, Fig. 9g). Additional notes to supplement the main text model description: The universal plating reversibility was previously estimated to be roughly 70% ($\eta = 0.7$) under fast charge conditions and modest amounts of plating[39] and is a value previously observed at low temperature (-20ºC) and overcharge rate (C/10) plating conditions[17]. Irreversible lithium plating is determined from multiplying (1- η) by the modeled plating amount. All electrolyte transport properties are taken from Idaho National Laboratory's Advanced Electrolyte Model (AEM)[49] and use empirical fits as a function of salt concentration and temperature[11]. The anode and separator Bruggeman coefficient are estimated as 2.2-2.3 and 2.0, respectively, based on detailed microstructure characterization/modeling and impedance spectroscopy using a blocking electrolyte[50]. The exchange current density and solid-state diffusion are estimated based on extensive fitting to electrochemical data including full-cells, half-cells, and 3-electrode test setups from within the US Department of Energy XCEL fast charge program[11,35,58]. The exchange current density for the lithium working electrode and lithium plating within the graphite anode are both set to 10 A/m^2 as in our prior report[39]. The half-cell and full-cell models are written in C++ and use the SUNDIALS Suite of Nonlinear and Differentiable/Algebraic Equation Solvers[51].

Lithium plating reversibility on graphite protocol (Fig. 9b). After 3 C/10 formation cycles and determining the experimental capacity, the graphite is intercalated at C/3 to 0.01 V and held 1 h or until current drops below 10 µA (C/500) followed by immediate C/5 discharge to 1.5V. This cycle is to determine the coulombic efficiency for complete graphite lithiation in the absence of lithium plating. The following 5 cycles are identical except after the intercalation, intentional overcharge (Li plating) occurs at the selected C-rate (0.2C-4C) and capacity (10-30% SOC), both specified relative to the experimental full graphite intercalation capacity. A representative voltage profile for this cycling protocol is provided in Fig. S23. The specific plating reversibility calculation is detailed in Eqn. 6 and corresponding text.

Incremental plating reversibility calculation (Fig. 9f). The data from Fig. 9c report the plating reversibility for 10%, 20%, and 30% overcharge (η_{10}, η_{20}, η_{30}) collected with separate coin cells and these values can be algebraically manipulated to estimate the reversibility for Li deposited between 10-20% SOC (η_{10-20}) and 20-30% SOC (η_{20-30}):

(reversible plating 0-20% SOC) = (reversible plating 0-10% SOC) + (reversible plating 10-20% SOC)

$$\eta_{20}(20\% \, SOC) = \eta_{10}(10\% \, SOC) + \eta_{10-20}(10\% \, SOC) \quad (7)$$

$$\eta_{10-20} = \frac{0.2 \, \eta_{20} - 0.1 \, \eta_{10}}{0.1} \quad (8)$$

Similarly,

31

$$\eta_{20-30} = \frac{0.3\,\eta_{30} - 0.2\,\eta_{20}}{0.1} \quad (9)$$

And error bars were estimated by standard propagation of uncertainty (see Supplementary Methods).

Lithium plating on copper foil (Fig. 9f). Lithium was deposited on 15 mm Cu foil (25 μm, MTI Corp) from a 14 mm Li metal electrode at a current density of 4C with respect to anode A2 capacity (3.1 mAh cm^{-2}) for 1.5 minutes (0.31 mAh cm^{-2}, 10% SOC) to mimic plating at the Graphite|separator interface during the graphite plating reversibility experiments. Immediately after Li deposition, an oxidative C/5 current was applied until the cell voltage exceeded 1.0V. The capacity ratio of the current stripping and plating steps is the reported reversibility. This cycle was repeated 5 total times with 10 minutes rest in between, and the reversibility reported is an average value from cycles 3-5 (2+ cells for each electrolyte), which exhibit stabilized CE value relative to the first 2 cycles (Fig. S25).

Graphite|NMC532 full-cell electrolyte testing (Fig. 10a-c). The experimental full-cell capacity is determined from the discharge capacity of the 3rd and final C/10 formation cycle and used to set the C-rates and capacity cutoffs for subsequent cycling. One slow formation cycle entails C/10 charge to 4.2 V and C/5 discharge to 3.0 V. All full-cell cycles include 5-minute rests between current steps. Next, 20 additional formation cycles are performed with 1C charge to 4.2V and 1C discharge to 3.0 V, holding until the current drops below C/5 on discharge (~5 min). Cell performance is analyzed from the following sequence: 5 cycles of **a)** 1C CCCV charge to 4.2V, holding until C/5 (~10 min), and 1C discharge to 3.0 V holding until C/5, alternating with 2 cycles of **b)** 6C CCCV charge to 4.2V, holding until 80% SOC (about 12 min total charge), then 1C discharge to 3.0 V holding until C/5. This sequence is repeated 20 times for a total of 100 1C cycles and 40 6C cycles. To prepare full-cells for titrations, the final step is a C/5 deep discharge down to 0.1 V to remove residual active lithium from the graphite. **Electrochemical data analysis** (Fig. 10b-d). Electrode voltage (V) shifts or capacity (Q) changes in full-cells are often characterized by monitoring the capacity (x-position) at which local extrema in differential voltage curves (dV/dQ, y-axis) occur[52]. Here, the dV/dQ vs. Q curve shift is alternatively calculated from the capacity at which $Q_0 \cdot dV/dQ = 1.0$ V, defined as X, where Q_0 is the initial cell capacity (Fig. S34, Supplementary Note 6). The graphite SOC shift (ΔX) between Cycles 5 and 6, which corresponds to 6C Cycles 1+2 in Fig. 10c, is calculated with the following equation, and the subscript denotes the 1C cycle number:

$$\Delta X_{6C\ cycles\ 1\ \&\ 2} = (X_7 - X_5) - (X_5 - X_3) \quad (10)$$

This equation is used instead of $\Delta X = (X_6 - X_5)$ to account for transient behavior of the 1st 1C cycle after fast charging (here, Cycle 6) and to subtract nominal SOC shift that would also occur in 1C cycles, $(X_5 - X_3)$, reducing contributions from cell aging unrelated to fast charging. Supplementary Fig. S35 provides thorough justification for this formula. Generalizing to determine ΔX that occurs for the 2 6C cycles n and (n+1) that occur between 1C cycles N and (N+1) yields:

$$\Delta X_{6C\ cycles\ n\ \&\ (n+1)} = (X_{N+2} - X_N) - (X_N - X_{N-2}) \quad (11)$$

For 1C cycle numbers: N = [5, 10, 15, …, 90, 95] and
Corresponding 6C cycle numbers: n = (2N/5) - 1 = [1, 3, 5, …, 35, 37]

Similarly, the changes in 1C discharge capacity reported in Fig. 10c, ΔC, are calculated by the following where C is the discharge capacity for the Nth 1C cycle:

$$-\Delta C_{6C\ cycles\ n\ \&\ (n+1)} = (C_{N+2} - C_N) - (C_N - C_{N-2}) \quad (12)$$

For both ΔX and ΔC, the values for 6C cycles 39&40 are assumed identical to cycles 37&38 because additional 1C cycles were not performed after the 2 final fast charge cycles.

Graphite|NMC532 SOC-sweep Li plating quantification (Fig. 11a-c). For these cells, the experimental full-cell capacity, $C_{full-cell}$, was fixed at 4.30 mAh (100% SOC, 2.80 mAh/cm², average of previous experiments) to fix the current density applied to the graphite electrodes for comparison with Li|Graphite cells. **1. Cycling Protocol. a)** 3x slow formation cycles 3.0-4.2V as described above. **b)** 10x 1C formation cycles CC charge to 4.2V, 1C CCCV discharge to 3.0V hold until C/20. Holding until C/20 was selected to minimize the graphite lithiation at the start of charge for the best comparison with Li|Graphite cell measurements. **c)** 1x cycle C/10 charge to 4.2V, 1C discharge to 3.0V hold until C/20. The charging step is used for dV/dQ analysis to determine the active graphite capacity and graphite lithiation at the start of charge (Supplementary Fig. S44). **d)** Cell performance was analyzed from the following sequence (see Supplementary Fig. S38 for representative voltage profiles during this protocol): 2 cycles of **i)** 1C CCCV charge to 4.2V, holding until C/5 (~10 min), and 1C discharge to 3.0 V holding until C/20, alternating with 2 cycles of **ii)** fast charge at the specified C-rate constant-current until X% SOC, then 1C discharge to 3.0 V holding until C/20 and **iii)** repeating from sequence i) except increasing the fast charging SOC cutoff of ii) by 5%. After the final set of fast charging cycles, 2 additional 1C cycles are performed. **iv)** C/5 deep discharge to 0.1V to prepare for titrations. **2. Data analysis. a)** The graphite SOC shift ΔX and capacity loss ΔC for each pair of fast charging (FC) cycles was calculated by taking the difference of the 2nd cycle of each pair of 1C cycles. Only the 2nd cycle was analyzed due to transient capacity and coulombic efficiency behavior for the 1st 1C cycle of each set after fast charge (Supplementary Fig. S39-40) . Inspired by the analysis described for the 140-cycle full-cell methods above:

$$\Delta X_{fast\ charge\ at\ XC\ to\ X\%\ SOC} = \left(X_{2nd\ 1C\ cycle\ after\ FC} - X_{1C\ cycle\ before\ FC} \right) \quad (13)$$
$$-\Delta C_{fast\ charge\ at\ XC\ to\ X\%\ SOC} = \left(C_{2nd\ 1C\ cycle\ after\ FC} - C_{1C\ cycle\ before\ FC} \right) \quad (14)$$

Note: in contrast to the 140-cycle full-cell equations for ΔX and ΔC, here there is no correction term that subtracts losses for 1C aging. **b)** This is because for the next analysis step, to estimate irreversible Li plating, the $\Delta C + \Delta X$ data from part **(a)** (seen in Fig. 11a) is baselined to subtract losses from aging that are not related to lithium plating. This process is illustrated and discussed thoroughly in Supplementary Fig. S41. **c)** Finally, to convert full-cell SOC at the end of charge (x-axis, Fig. 11a) to graphite lithiation at end of charge (x-axis, Fig. 11b), the following equation is used:

$$x\ in\ Li_x C_6 = x_{initial} + SOC_{full-cell} \cdot \frac{C_{full-cell}}{C_{active\_graphite}} \quad (15)$$

Where $x_{initial}$ is the initial graphite lithiation at the beginning of charge and $C_{active\_graphite}$ is the active graphite capacity, both determined from dV/dQ analysis (Fig. S44). Uncertainty propagation analysis indicates that the error induced by this transformation is no larger than 1% lithiation (see Supplementary Note 7).

Electrode extraction, imaging, mass-spectrometry titration, and titration calibrations (Fig. 10c, Fig. 11c). Graphite electrodes from full-cell experiments were extracted with a Hohsen Coin Cell Disassembling Tool in the glovebox and imaged with a wireless handheld microscope (TAKMLY) before transferring to individual 6 mL vials (Metrohm). The vials were placed under active vacuum for 5 minutes before crimp-sealing the septum caps. Electrodes were extracted within 24 h of cycling completion and were stored in the glovebox for up to 3 days before titration. Rinsing the electrodes 2x with dimethyl carbonate before vial storage was found to have minimal effect on dead Li measurements, so the majority of samples were not rinsed (Fig. S33).

The Ar-filled sample vials were removed from the glovebox, quenched with 0.5 mL of nitrogen-sparged deionized water, swirled for 10 seconds, and then attached to the mass spectrometry titration (MST) system using a novel syringe needle attachment featuring an adapter (Valco, part # ZBUMLPK) from 1/16" stainless steel tubing to Luer-lock (Fig. S28). The MST system draws 2 mL of the vial headspace every 2 minutes, refilling the balance with ultra-high purity Argon, using a constant system pressure of 1030 ± 10 Torr. After about 40 minutes, or when the H_2 signal (m/z = 2) had decayed to its initial value (Fig. S29), the next vial was attached. This improved vial-swapping design along with smaller vial volume resulted in a three-fold throughput increase from our previous work[39], and the signal strength suggests that 50 ng of Li metal (equivalent to 0.2 μAh total capacity) can be confidently quantified with each headspace sample precise to 10 ng (Supplementary Fig. S31). The calibration process that quantifies the linear relationship between the H_2 signal and the partial pressure of H_2 is detailed in Supplementary Note 8 and Fig. S29. To safely and precisely generate small quantities of H_2 in the 6 mL vials, graphite electrodes were formed and lithiated to known SOC (10-30%) in half-cells, extracted as detailed above, cut into pieces with known mass fractions of the entire 15 mm electrode, and titrated, assuming the complete conversion of the following reaction:

$$Li_xC_6 + xH_2O \rightarrow C_6 + 0.5xH_2 + xLiOH \quad (16)$$
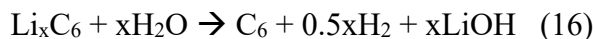
The amount of titrated Li in the manuscript is presented as a capacity by converting the moles of H_2 assuming 1 mol oxidizable Li species per 0.5 mol H_2, and 1 mol e^- per mol Li.

Even in the absence of lithium plating, cycled graphite electrodes are expected to have nonzero titrated Li due to the presence of residual Li_xC_6[39] that is either electrically isolated or not fully removed during the deep discharge step. This nonzero amount was quantified with controls for each type of experiment and subtracted from the values reported in Fig. 10 and Fig. 11. For Fig. 10 experiments, the value was 0.012 ± 0.002 mAh/cm^2 (see Fig. S32), and for Fig. 11 experiments it was 0.019 ± 0.001 mAh/cm^2 (Supplementary Fig. S43), both of which are <1% of the total graphite lithiation capacity of 3.25 mAh/cm^2.
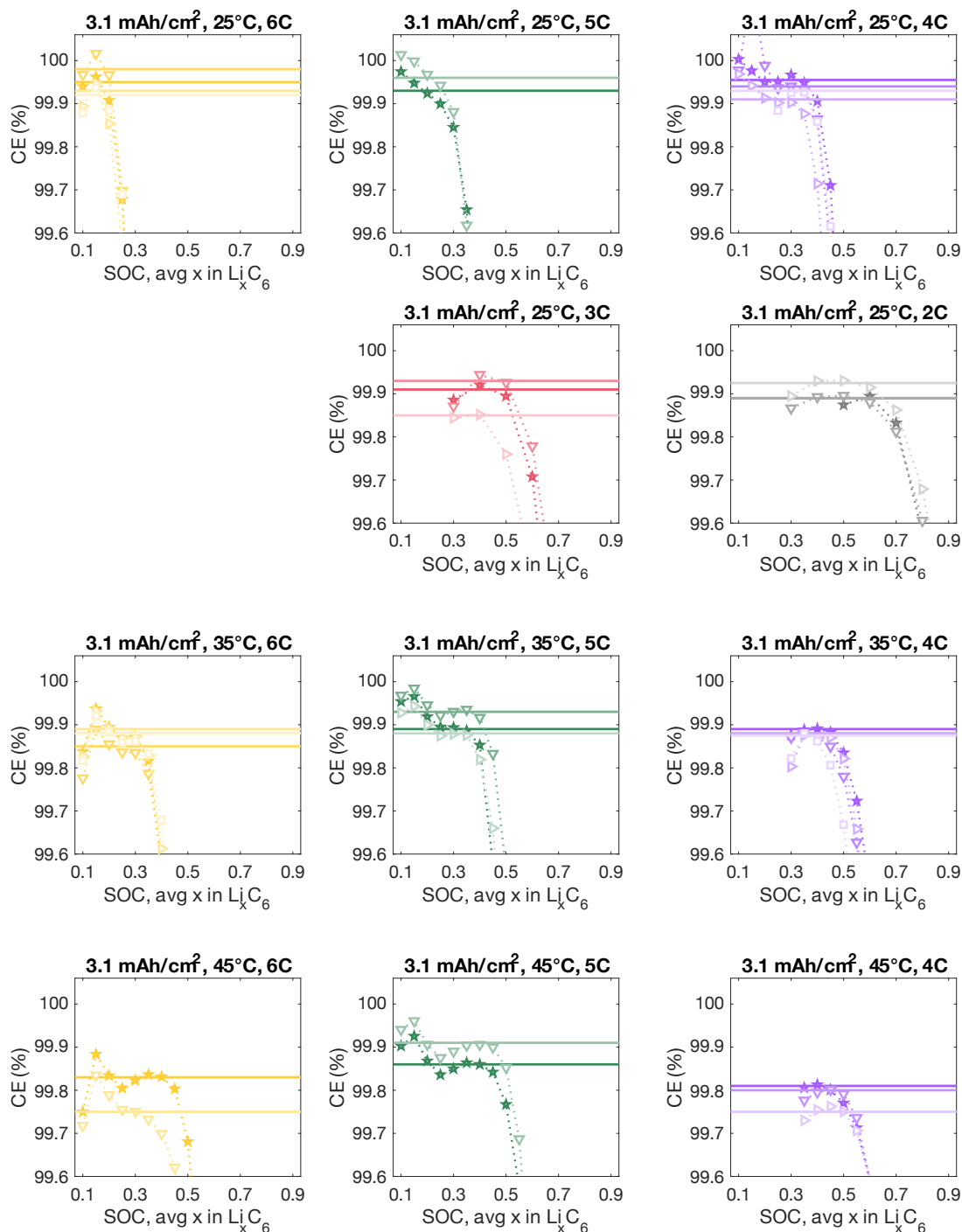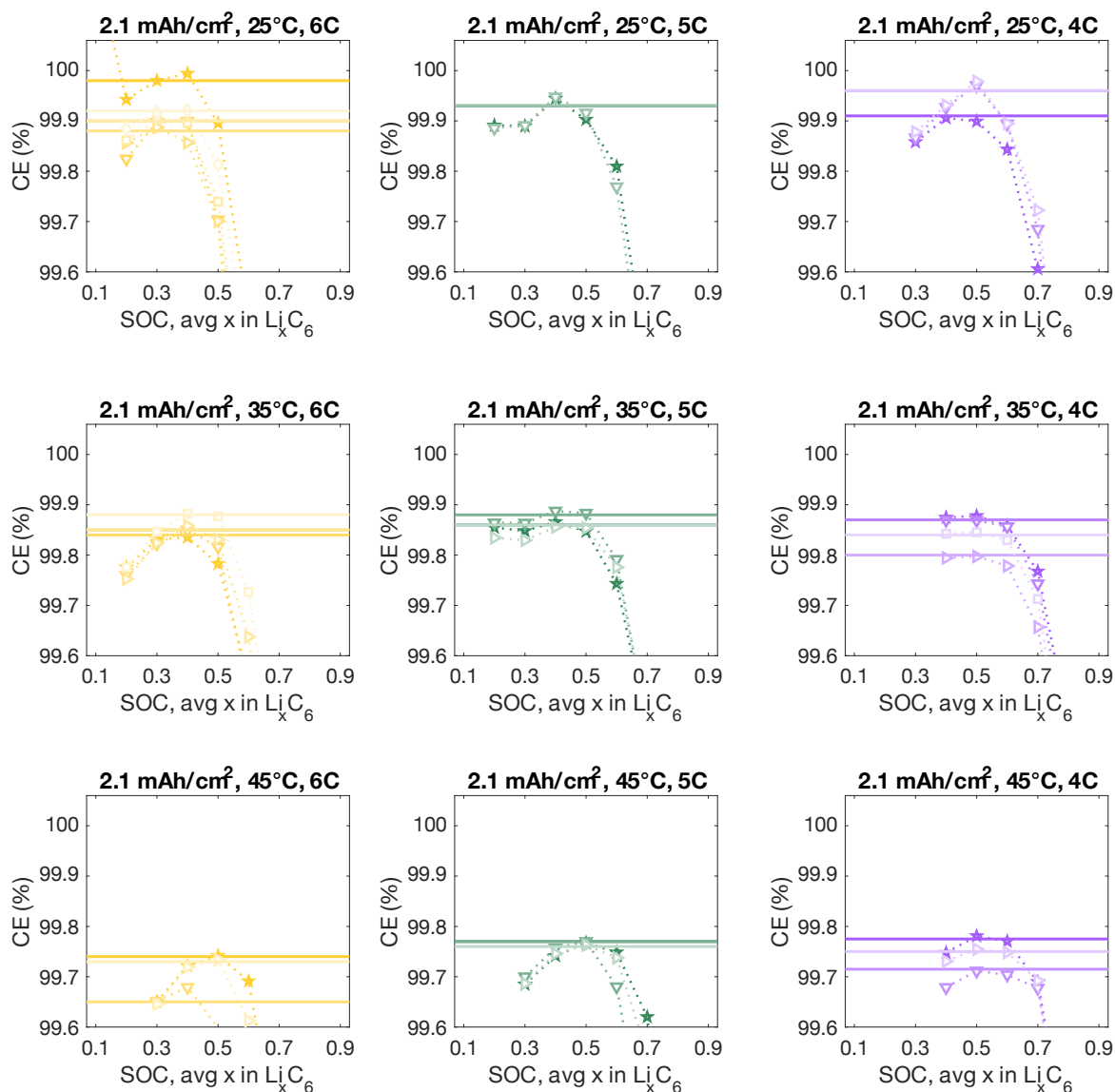
Fig. S8. Coulombic Efficiency Baseline Fitting for all Fig. 8a-f data – 3.1 mAh/cm². The CE baselines, shown as horizontal lines, were unique to each cell and fit manually due to some transient CE behavior sometimes observed during the first 1-3 cycles.

Discussion of Fig. S8-S9: The SOC for which CEs are collected is described in the Methods and Table S3. The baseline is either assigned near a) the y-value of an observed CE plateau (repeated CE measurements within ~0.02% even as cycle capacity/SOC varies) or b) near the maximum measured CE value. Sometimes the first 3 fast charging cycles (leftmost 3 datapoints in a series)

exhibit increasing (Supplementary Fig. S9, middle row left column) or decreasing (Fig. S8, top row middle column) trends with SOC. We first note that the magnitude of these drifts are very small, typically <0.02% CE per cycle, whereas the clear CE drops near the onset of plating are >0.1% CE. Second, those first cycles have the lowest intercalation capacities (SOC or mAh), which is the denominator of CE, so those CE values are most sensitive to small changes in deintercalation capacity (the numerator). Physically, we attribute the increasing CE to additional SEI formation losses on the first few cycles. The decreasing CE may occur due to slight electrode de-wetting or active material loss in coin cells due to experimental error in fabrication. However, for all these slight variations, the expected trends of lithium plating are still observed, giving us confidence in the robustness of the method, as discussed related to Fig. 7c, Fig. 8a-g in the main manuscript.


Fig. S9. Coulombic Efficiency Baseline Fitting for all Fig. 8a-f data – 2.1 mAh/cm². The CE baselines, shown as horizontal lines, were unique to each cell and fit manually due to some transient CE behavior sometimes observed during the first 1-3 cycles.

	25℃	35℃	45℃
3.1 mAh/cm^2	99.92 ± 0.03	99.88 ± 0.02	99.82 ± 0.06
2.1 mAh/cm^2	99.93 ± 0.02	99.85 ± 0.02	99.74 ± 0.04

Discussion of Table S3: The baseline coulombic efficiency corresponding to the absence of Li plating is visually observed to decrease with temperature in Fig. S8, so here we quantify the dependence across all cells, grouped by loading and T. The clear temperature dependence, regardless of loading and rate, may suggest increased continual SEI dissolution during the long C/5 discharge steps that results in lost capacity to additional SEI formation on the next cycle. It is important to remember that all cells are cycled fewer than 20 times, so we expect the SEI to be fairly thin and undergo slight continued growth throughout the protocol. Especially for the first few fast charge cycles, capacity loss to additional SEI formation is expected because the rapid graphite expansion with phase change is likely to compromise some parts of SEI. High temperature is known to promote battery self-discharge, and at the graphite electrode many parasitic reactions form new SEI, so we believe this is a reasonable hypothesis. The slow C/5 deintercalation and 30 min rest between current steps means the cycles last ~3-5 hours, sufficient time for additional ~0.04% self-discharge at elevated temperature with nascent SEI.
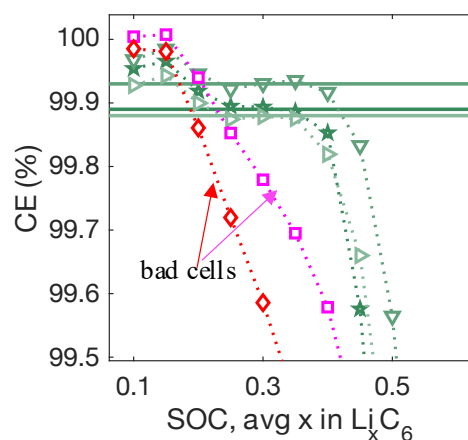
Fig. S10. Removing data from 'bad cells' and ensuring experiment fidelity by CE inspection

Discussion of Fig. S10: Typically 3 cells were run initially at each condition in Fig. 8a, but the number of cells reported varies between 2 and 5 (Fig. 8a-f, bottom left of each panel). An additional set of 2-3 cells may have been run for better data statistics or to make up for data that was excluded due to indicators of poor cell performance. The above figure shows 2 cells in red diamonds and pink squares, for example, at the [5C, 3.1 mAh/cm^2, 35°C] condition, that were excluded. Compared with the other data, the coulombic efficiency decreases linearly and continuously with increasing SOC, either indicating an outlier for the onset of irreversible lithium plating by 15-20% SOC or other rapid cell aging mechanisms. Given the experimental imperfections in manual cell fabrication, we attribute this behavior to bad electrode alignment which may result in early lithium plating on the conductive spacers or other cell parts instead of the graphite electrode. Observing these anomalies, however, increases the fidelity of the 'good' data used for analysis and also motivates the need for automated cell manufacturing methods to reduce human error. It is

important to note that the extreme conditions of fast charging and the heterogeneous nature of lithium plating exacerbate the smallest cell defects, so some bad data should be expected, further motivating the need for adequate statistics of Li plating studies.

**Table S3. SOC-sweep range selection for Li|Graphite plating onset experiments**

	25℃	30℃	35℃	45℃
Anode A1	6C [20:10:80]		6C [20:10:70]	6C [30:10:90]
(2.1 mAh/cm²)	5C [20:10:80]		5C [20:10:80]	5C [30:10:90]
	4C [30:10:90]		4C [40:10:90]	4C [40:10:90]
Anode A2	6C [10:5:35]		6C [10:5:60]	6C [10:5:70]
(3.1 mAh/cm²)	5C [10:5:50]		5C [10:5:60]	5C [10:5:70]
	4C [10:5:55]		4C [30:5:80]	4C [30:5:80]
	4C [10:5:80]	Fig. 9a		
	3C [30:10:90]			
	2C [30:10:90]			
Anode A3		6C [10:5:40]	Fig. 11b	
(3.35 mAh/cm²)		4C [10:5:55]		
		3C [25:5:70]		
Anode A4		5.5C [10:5:40]	Fig. S20	
(3.75 mAh/cm²)		3.5C [10:5:60]		

Discussion of Table S3: These are the SOC cutoffs tested for the fast charging cycles, in order of low to high SOC (see manuscript methods) for all loadings, temperatures, and C-rates reported for Fig. 8 (white), Fig. S20 (orange), Fig. 9a (green), and Fig. 11b (blue). The nomenclature [20:10:80] means that the first cycle charged to 20%, the last cycle charged to 80%, and the intermediate cycles were incremented by 10% SOC. For conditions with anticipated Li plating onsets at high SOC, larger SOC increments were selected (10% instead of 5%) to i) reduce experiment time given slow C/5 graphite deintercalation to 1.5V and ii) limit Li metal electrode aging effects.
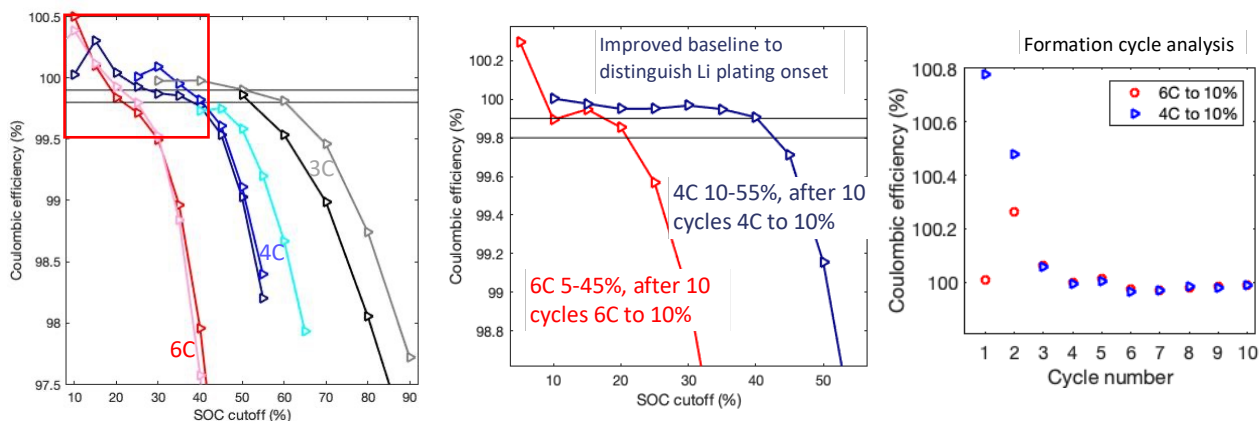
Fig. S11. Motivation for Li|Graphite cell Fast Formation before SOC-sweep. Left: Results from the fast charging SOC-sweep protocol for Li|Graphite cells with 3 C/10 formation cycles only shows drifting, noisy CEs that make it difficult to baseline and quantify Li plating (red box). **Center:** Fast charging SOC-sweep results after 10 cycles of 6C to 10% SOC (red) and 10 cycles of 4C to 10% SOC (blue) were added to the standard formation protocol. **Right:** The CEs for the fast-formation cycles to 10% show stabilization near Cycle 4, justifying the selection of 5 cycles of 4C intercalation to 10% as the added fast formation protocol.

Discussion of Fig. S11: We emphasize the importance of having stable baseline CEs prior to the Li plating onset for accurate irreversible Li quantification from the coulombic inefficiency, and note that the optimal formation protocol may differ depending on specific cell geometry. This is one reason why the SOC-sweep protocol should have multiple (>3) cycles to low SOC before the expected Li plating onset, to enable clear baseline CE fitting. This rule of thumb helped inform the SOC-sweep range selection above.
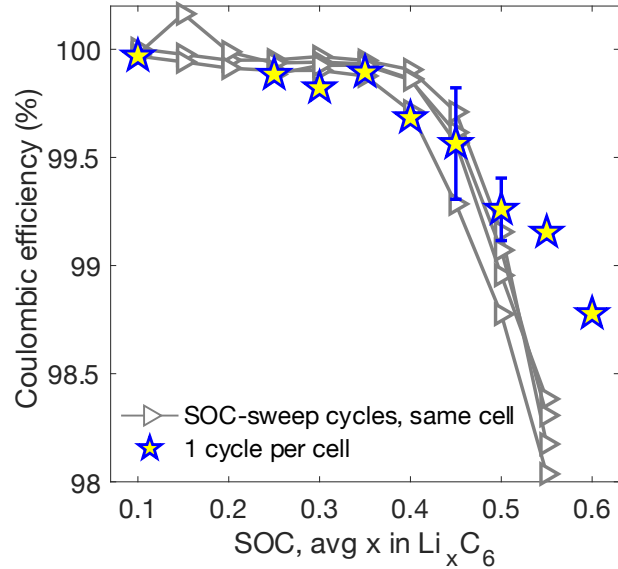
Fig. S12. Control experiments to understand SOC-sweep protocol cell aging effect. An initial concern with the SOC-sweep protocol was whether the early SOC cycling affected the onset and amount of irreversible Li plating, which would be an undesirable aging effect for comparing results across cells with Li plating at different conditions. Here we show that for the [4C, 3.1 mAh/cm^2, 25°C] condition, coulombic efficiencies recorded from the SOC-sweep, in which cycles were all performed on the same cell (grey, n=4 cells), match very closely with CEs taken with only 1 fast charging cycle per cell (stars, n=13 cells, replicates recorded for 0.40-0.55 SOC, standard deviation shown although too small to see for 0.4 and 0.55 SOC).

Discussion of Fig. S12: Despite some expected transient behavior for the CE of the first fast charging cycle (leftmost data points in Supplementary Fig. S8 and Fig. S9 curves, at low SOC), the data show excellent agreement for the onset of CE drop and irreversible Li plating from 40-50% SOC. For cycles to higher SOC far beyond the plating onset, more loss is observed for the SOC-sweep cells that have a history of Li plating. This is expected as the accumulation of small amounts of dead Li plating can provide nucleation sites for increased Li plating on future cycles and/or disrupt Li$^+$ electrolyte transport through the porous electrode, leading to increased plating. However, this work performs quantitative analysis only on the plating onset region and small irreversible Li amounts, so we believe this aging effect is not a concern to the present study. In commercial cells, of course we expect cell aging and changes in cell resistances to affect Li plating onsets, but those effects become significant on the order of 10^2-10^3 cycles instead of the ~7-12 cycles performed here.
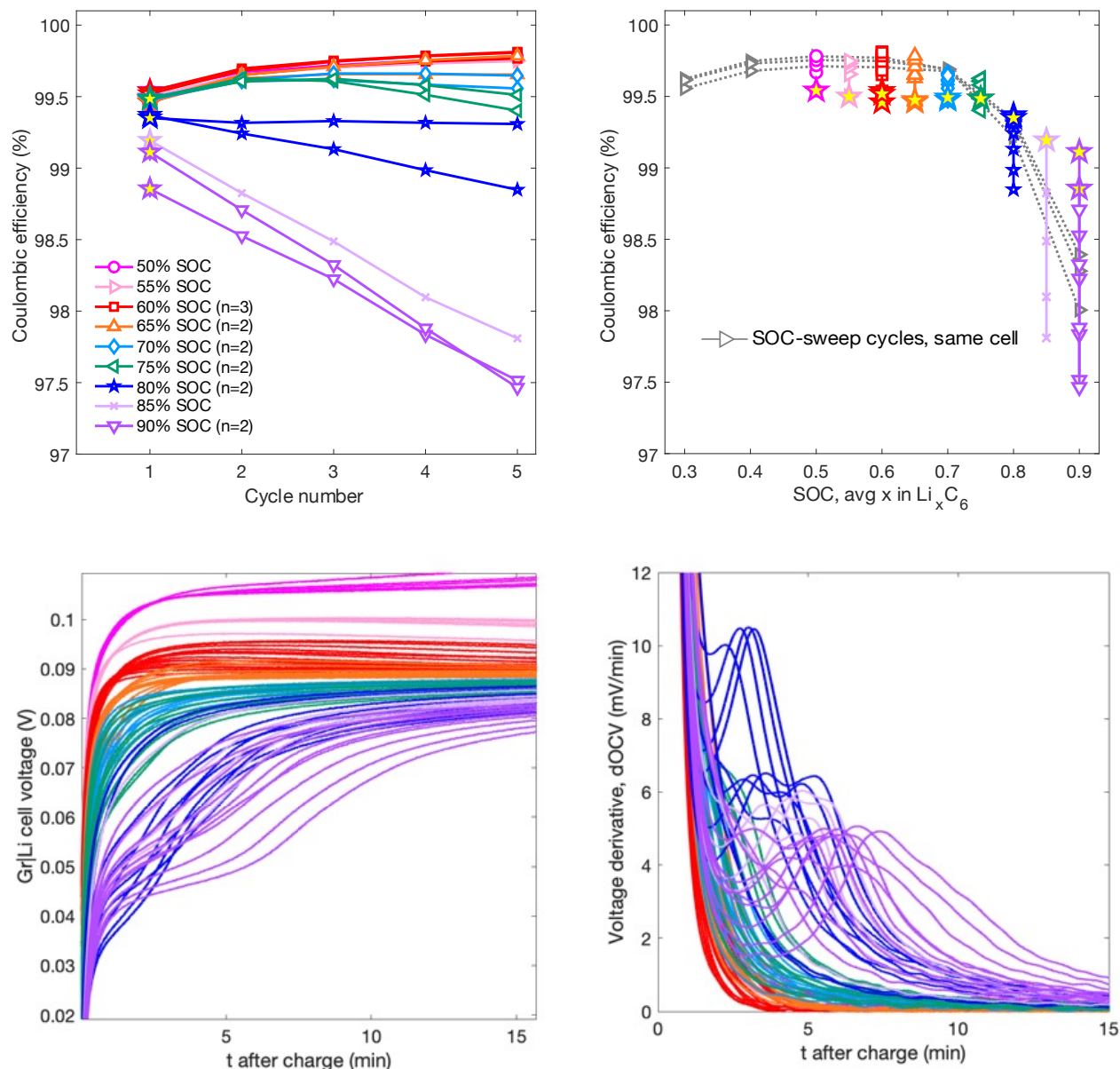
Fig. S13. Confirming the presence of Li plating and experiment validation at 45°C. Here we confirm that Li plating is the dominant mechanism of capacity loss at high temperatures instead of other possible cell degradation or Li metal electrode aging. For the [4C, 2.1 mAh/cm^2, 45°C] condition, we cycled cells 5 times to a single SOC, ranging 50-90% SOC, and the CEs are plotted in the top left. A star represents the efficiency for the first fast charging cycle. The first sign that cell aging related to the Li metal electrode is not causing the drop in CE is that for 50-65% SOC, the coulombic efficiency continually increases with cycling. This suggests no Li plating at these SOC and the continual formation of a more temperature-resistive SEI. Next, we compare the CEs for each cell with CEs recorded from the SOC-sweep method (top right panel), data presented in Fig. 8a-f. The overlay shows excellent agreement between the single-SOC and SOC-sweep efficiencies. For Li plating conditions, it is expected that the CE decrease with cycling to that SOC due to previously discussed aging effects in Supplementary Fig. S9. The earliest SOC at which this behavior occurs is 70-75%, which agrees well with the plating onset of ~71% SOC reported for this condition using the SOC-sweep in Fig. 8g. To confirm the presence of Li plating, the voltage relaxation after charge (bottom left) and corresponding derivative (bottom right) are plotted and show the characteristic voltage plateau/derivative peak feature that signals Li^0 re-intercalation[23,24,60] at 80% SOC and above, consistent with the method's sensitivity for Li plating detection[56].

41
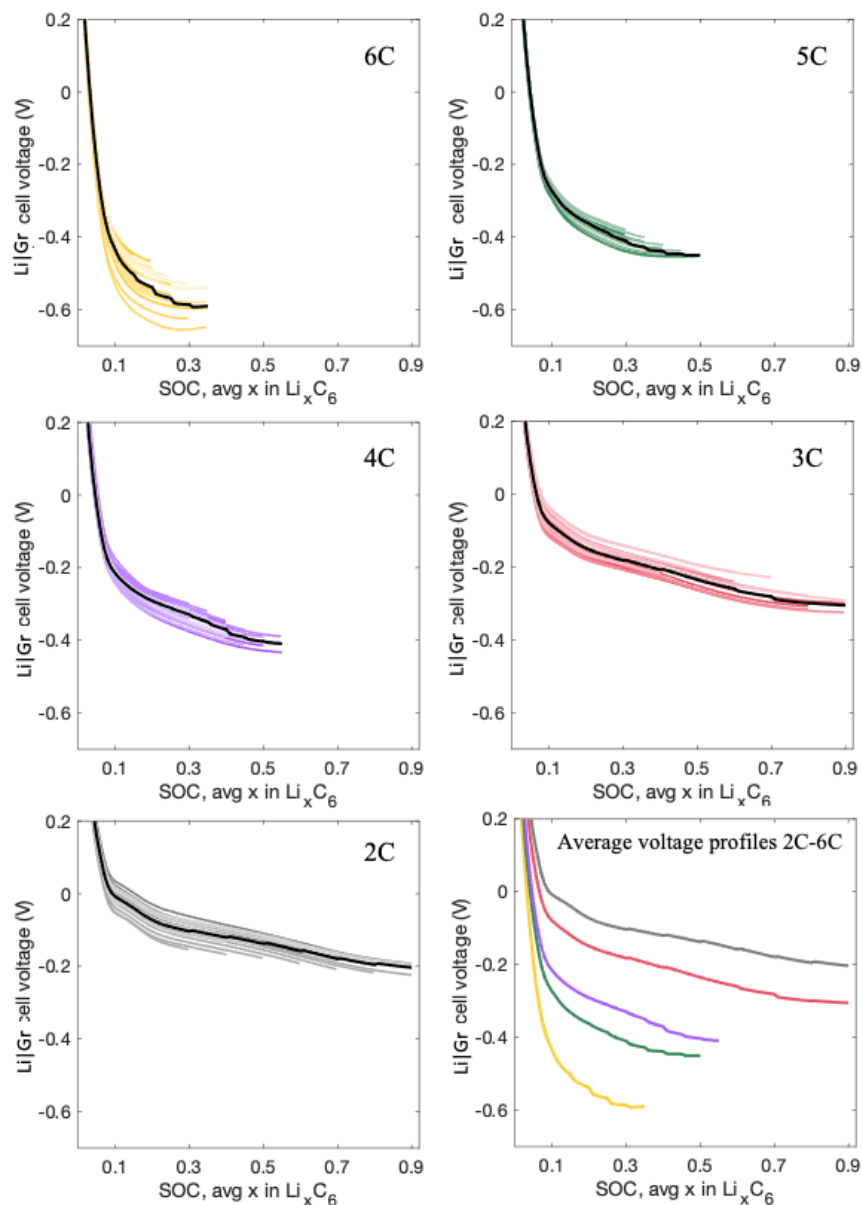
Fig. S14. Calculating average experimental voltage profiles for model comparison. We calculate average experimental voltage profiles for each [rate, loading, temperature] combination across all cells and fast charging cycles. Shown here is the averaging for the 3.1 mAh/cm² and 25°C data from Fig. 8a. The average voltage profiles are shown in the bottom right, and note that the discontinuities every 5-10% SOC are artefacts of cell resistance drifting with aging.

Discussion of Fig. S14: Due to variability in cell-to-cell preparation, resistances vary slightly by sample. We do not observe any correlation with cell resistances and Li plating behavior within data for a given C-rate. For example, 2 identically constructed and cycled cells may have slightly different resistances, and the one with a larger overpotential (more negative average voltage) does not necessarily show an earlier plating onset or larger amount of irreversible Li plating.

Table S4. Model parameters for Li|Graphite cells. C_e is the local salt concentration in mol/L and x is local graphite intercalation fraction.

| Parameter	Graphite Electrode 2.1 mAh/cm^2 / 3.1 mAh/cm^2	Separator	Lithium
Thickness (µm)	47/70	25	N/A
Porosity (%)	37.4/35.4	55	N/A
Particle Radius, r_p (µm)	4	N/A	N/A
Bruggeman Exponent	2.1	2.0	N/A
Exchange current density, i_0 (A·m^{-2})	$0.3\,(C_e)^{0.5}(C_s)^{0.5}(C_s - C_s^{max})^{0.5}$	N/A	10
Activation energy for exchange current density (kJ/mol)	30	N/A	50
Solid-state Diffusion Coefficient, D_s (m^2·s^{-1})	3E-14$(1.5 - x)^{2.5}$	N/A	N/A
Activation energy for solid-state diffusion (kJ/mol)	15	N/A	N/A
Maximum Intercalated Lithium Concentration, C_s^{max} (kmol·m^{-3})	28.0	N/A	N/A
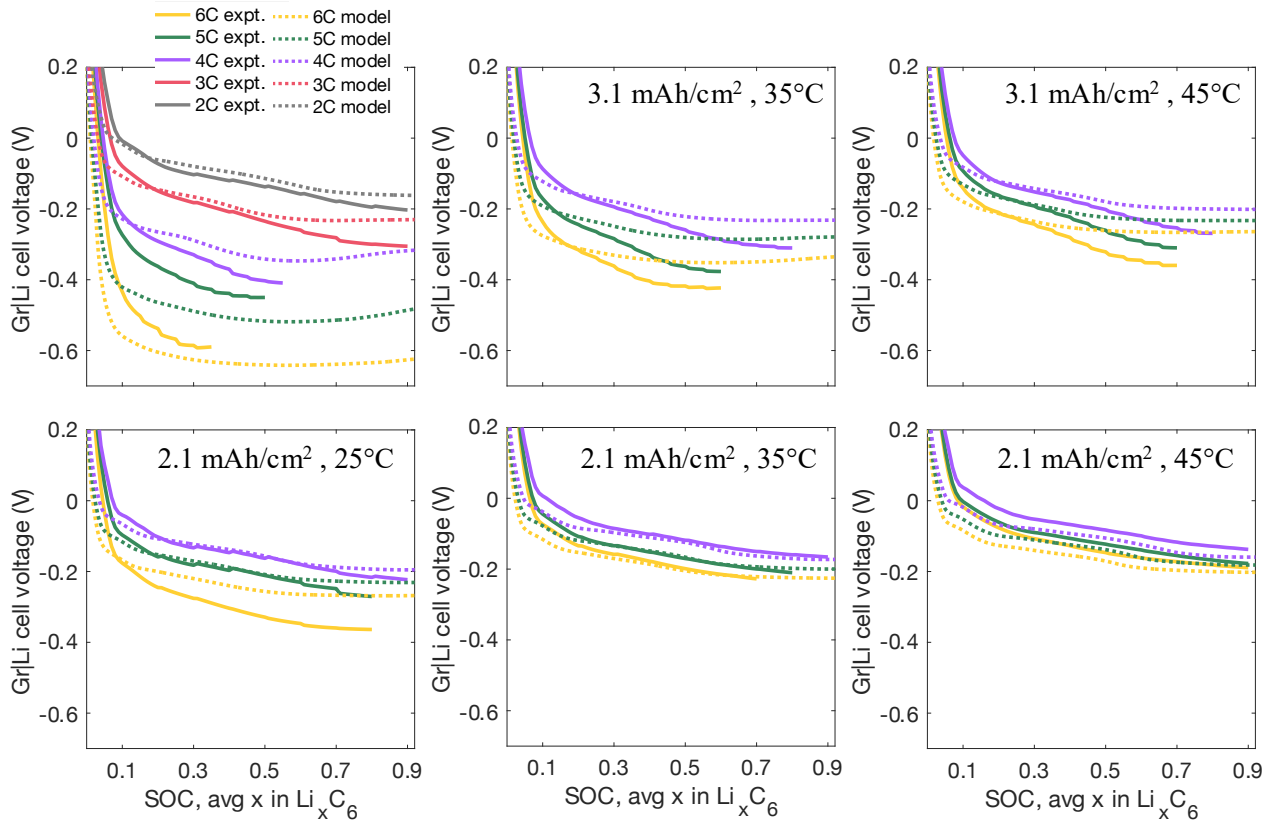
Fig. S15. Model-Experiment Voltage Profile Comparison. Experimental average voltage profiles in Li|Graphite cells (see Supplementary Fig. S14) show good agreement with simulated voltages from the Electrochemical Model. Discrepancies at higher SOC and temperature for the top right panels may be due to Li metal electrode resistance increase/drift with SOC-sweep cycling, seen in Supplementary Fig. S14. **Note:** At high rates, many time-varying overpotentials contribute to the total cell voltage, so the 0.05 V difference that distinguishes the graphite phase plateaus would be difficult to distinguish even with uniform graphite lithiation. Models and experiment show that many lithiation phases exist simultaneously during fast charging, with higher lithiation phases such as LiC$_6$ being formed near the graphite|separator interface due to electrolyte ion transport limitations.
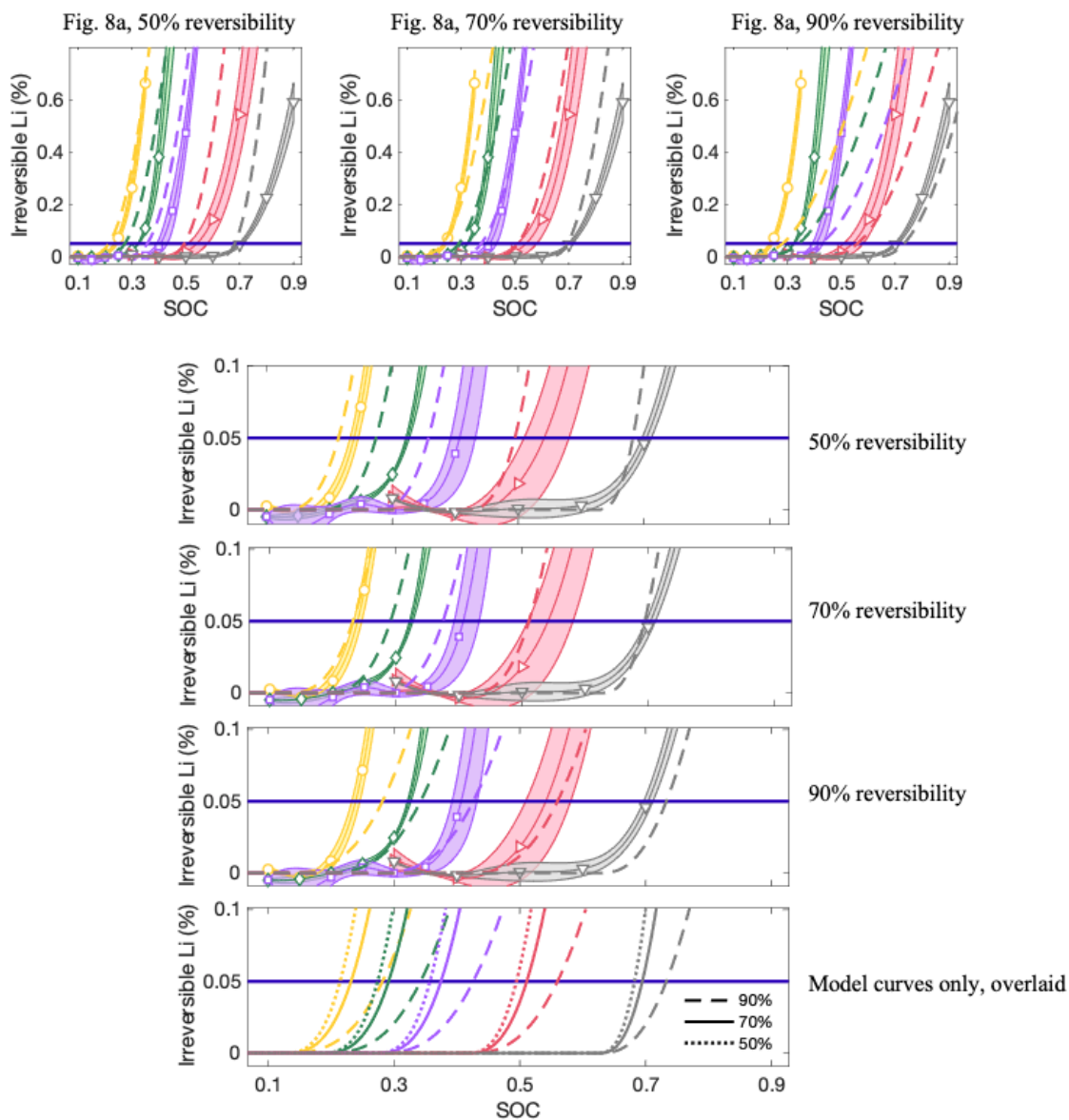
Fig. S16. Visualizing how varying the reversibility parameter affects simulated irreversible Li. The model outputs a quantity of total lithium plating, and a single reversibility parameter is used to scale that amount to plot the irreversible Li, as detailed in the Methods. At the top, Fig. 8a experiment data is shown for reference, and the model results are shown for varied Li plating reversibility. Increasing reversibility decreases the slope of the curve (left to right, dashed lines). The large panels below zoom in on the Li plating onset region, showing that a change in reversibility from 50-90% can change the onset of 0.05% Irreversible Li plating by up to ~7% SOC.
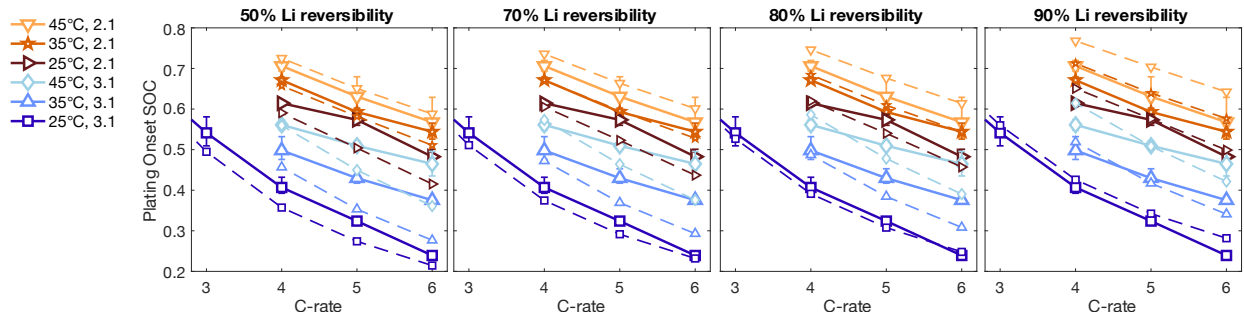
Fig. S17. Model-experiment plating onset comparison as model Li reversibility is varied. Computing the universal Li plating reversibility that minimizes Model-experiment error (Fig. 9f) requires first calculating new model Li plating onsets for each reversibility. Plotted above are the experimental Li plating onsets of Fig. 8g, fixed, compared with plating onsets from the model at different reversibilities. The sum of squared errors was calculated over all 20 [c, x, T] pairs, except [6, 3.1, 35] and [6, 3.1, 45], which were removed because they had nearly 10% SOC error in the initial plating onset analysis which was expected to skew the results towards high plating reversibility. Error bars are calculated in the same manner described in Fig. 8g.
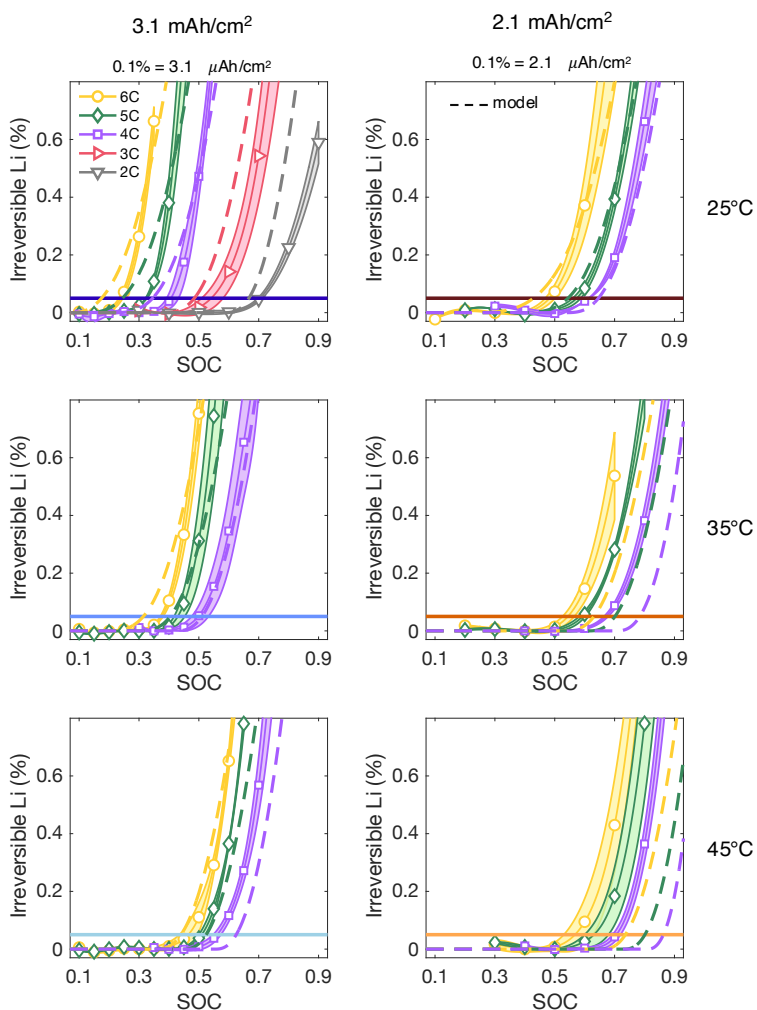
Fig. S18. Model-experiment comparison before changing solid-state Li diffusion parameters. The primary model change from previous works[35,39,58] to obtain Fig. 8a-f model outputs was incorporating intercalation fraction dependence on solid-state diffusion and decreasing the solid-state diffusion activation energy from 30 to 15 kJ/mol. Above are the experiment-model comparisons before those changes were applied. The most significant disagreement was observed at high temperatures for the low-loading electrodes.
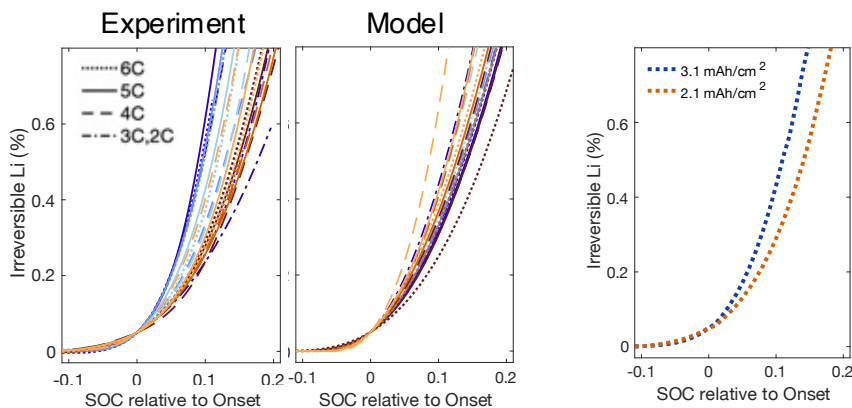
Fig. S19. Experimental and modeled irreversible Li plating curves overlaid. Experimental average and modeled irreversible Li plating curves from Fig. 8a-f shifted in the x-direction by their respective plating onset SOC. The colors correspond to the unique [temperature, loading] combinations as in Fig. 8a-f (colors also in Fig. S18 above), and the rate is depicted by the line style. The average experimental irreversible Li curve by loading is seen on the right. Irreversible Li accumulates faster (at lower SOC) for the 3.1 mAh/cm^2 electrode.
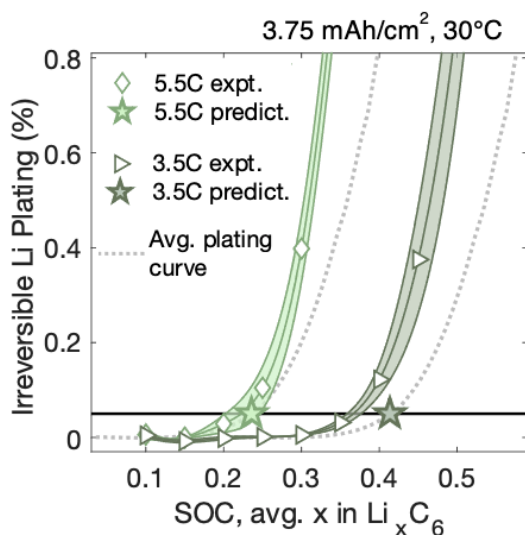
Fig. S20. Empirical fitting prediction accuracy for graphite loading outside of experimental range. The fitting predicts the lithium plating onset at 0.05% irreversible Li for a graphite electrode with loading of 3.75 mAh/cm^2, outside the loading range of the study in Fig. 8, within 5% SOC at moderate temperatures (30 °C) and rates (3.5-5.5C). The dotted lines are the average experimental universal Li plating curve from Supplementary Fig. S19 shifted by the predicted onsets.
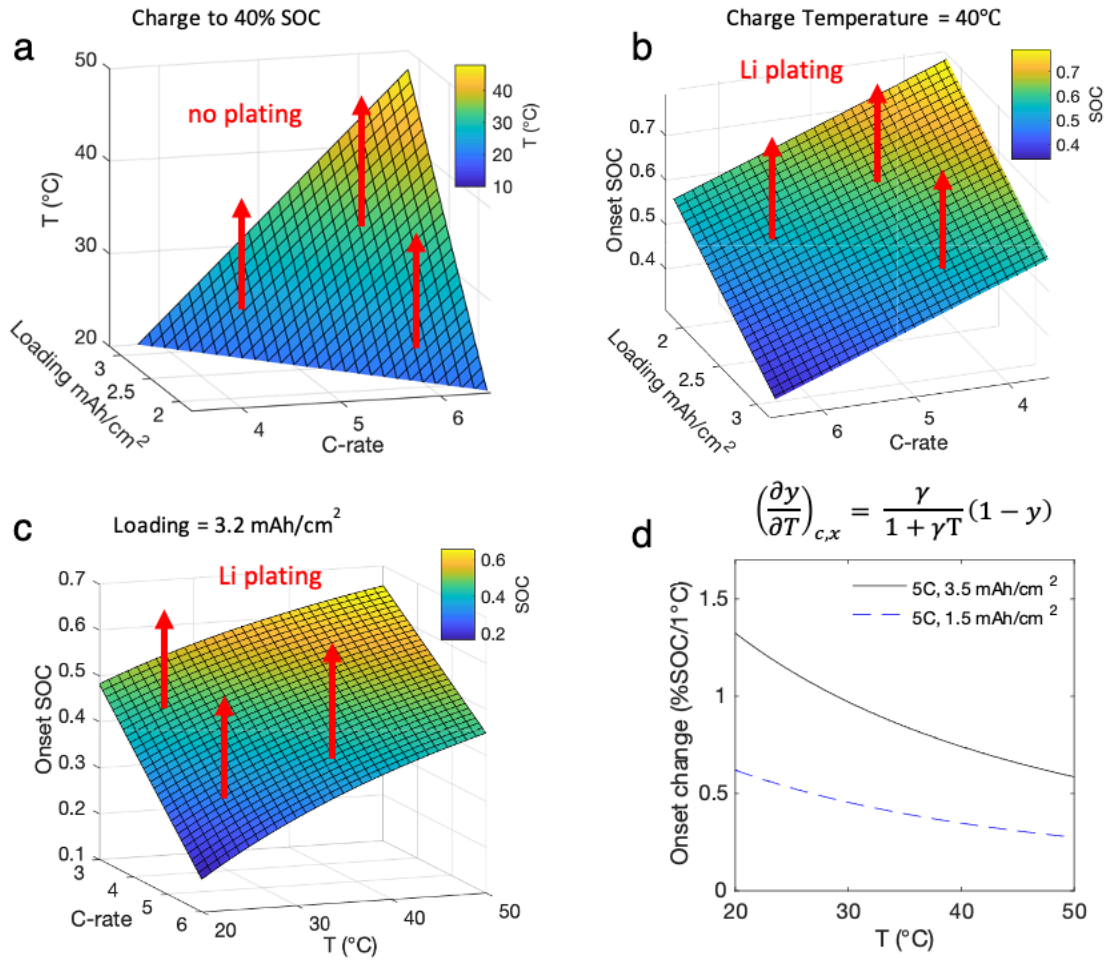
Fig. S21. Additional applications and insights from data-driven fitting for Li plating onsets. a) The charging temperature required to avoid plating for a constant-current (CC) charge to 40% SOC for various combinations of rates and loadings. b) Design tradeoffs to avoid lithium plating if the optimal charging temperature were fixed at 40°C, or c) if the graphite loading was required to be 3.2 mAh/cm² (middle). d) Another insight from the experimental data of Fig. 8g is that temperature has a smaller effect on the Li plating onset for the thinner electrodes with onsets at high SOC. The empirical fitting can quantify this effect to inform systems-level energy efficiency tradeoffs. Part d, for example, shows that as the charging temperature is increased, there are decreasing returns for postponing the Li plating onset. This analysis also quantifies the temperature effect on Li plating, and it is clear the effect is much larger for the high-loading (3.5 mAh/cm²) curve.

Supplementary Note 1. Empirical fitting limitations from Eqn. 5, Fig. 8h, Table 2

$$y(c, x, T) = \frac{\alpha\,c + \beta\,x + \gamma\,T + \varepsilon}{1 + \gamma T} \quad (5)$$

In general for this empirical fitting, it is not advisable to extrapolate results more than ~30% outside of the experimental parameter range. We explain the following limitations of model application for clarity, but emphasize that this fitting is to demonstrate the utility of large Li plating data sets, so if any significant extrapolation of the data is desired, researchers should be able to collect data for those conditions and construct their own model.

Temperature: In the limit of high temperature ($T \to \infty$), the plating onset, y, goes to 1, indicating no lithium plating. This makes physical sense but does not take into account electrochemical or

SEI degradation reactions that would increase at high temperature. For low temperature, at 4C rate and 3.0 mAh/cm^2 loading, non-physical negative y values are predicted for (T < -5°C), suggesting that model calculations within ~10°C of that limit, T < 5°C, should not be used. A more robust model may use a different temperature scale or a dimensionless temperature with respect to the electrolyte freezing point, which may be a suitable limit for the plating onset truly being 0, but this is beyond the scope of the work. **C-rate:** Physically, as (c → 0) the Li plating onset should go to 100% SOC. For 3.0 mAh/cm^2 loading and 30°C, the onset goes to 85% SOC, so only C-rates within the experimental range or close to it should be used. For these conditions, reasonable Li plating onsets may be expected up to 8-9C. **Loading:** Physically, as (x → 0) the Li plating onset should go to 100% SOC. For 4C rate and 30°C, the calculated onset for 0 loading is 104% SOC, which is not far off. Supplementary Fig. S20 experiments also suggest that 30% extrapolation of this parameter to higher loadings (3.75 mAh/cm^2) is effective, so we expect x within the range of approximately 1.2 to 4.0 mAh/cm^2 to give reasonable Li plating predictions.
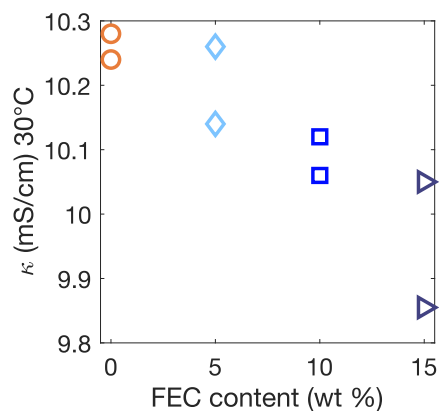
Fig. S22. Conductivity of carbonate electrolytes with varied FEC solvent content. Electrolyte solution conductivity data for 1.2 M LiPF$_6$ electrolyte with 0 to 15 wt% (X) FEC solvent, with total solvent wt% ratios of X:(30-X):70 FEC:EC:EMC. Conductivities were measured inside the glovebox using a Mettler Toledo InLab 751-4mm conductivity probe with blocking platinum electrodes. The probe was calibrated using 84 μS/cm, 1413 μS/cm, and 12.88 mS/cm aqueous standards (Mettler Toledo) prior to bringing inside the glove box. Electrolyte samples were maintained at 30°C using a dry block (Torrey Pines), and solution temperatures were verified using a temperature sensor inside the conductivity probe and were always within 0.2°C of the set point. Each datapoint corresponds to an independent preparation of that electrolyte; two electrolytes were made for each concentration.

Table S5. Baseline graphite intercalation cycle coulombic efficiencies (CE$_{int}$) for plating reversibility experiments. The number of baseline cycles, n, does not match the number of cells because some cells (3 for each electrolyte group) underwent 2 baseline cycles.

Electrolyte	Baseline CE (%)
70:30 EMC:EC	99.70 ± 0.11 (n=10, 7 cells)
70:25:5 EMC:EC:FEC	99.69 ± 0.03 (n=13, 10 cells)
70:20:10 EMC:EC:FEC	99.70 ± 0.03 (n=12, 9 cells)
70:15:15 EMC:EC:FEC	99.72 ± 0.04 (n=12, 9 cells)
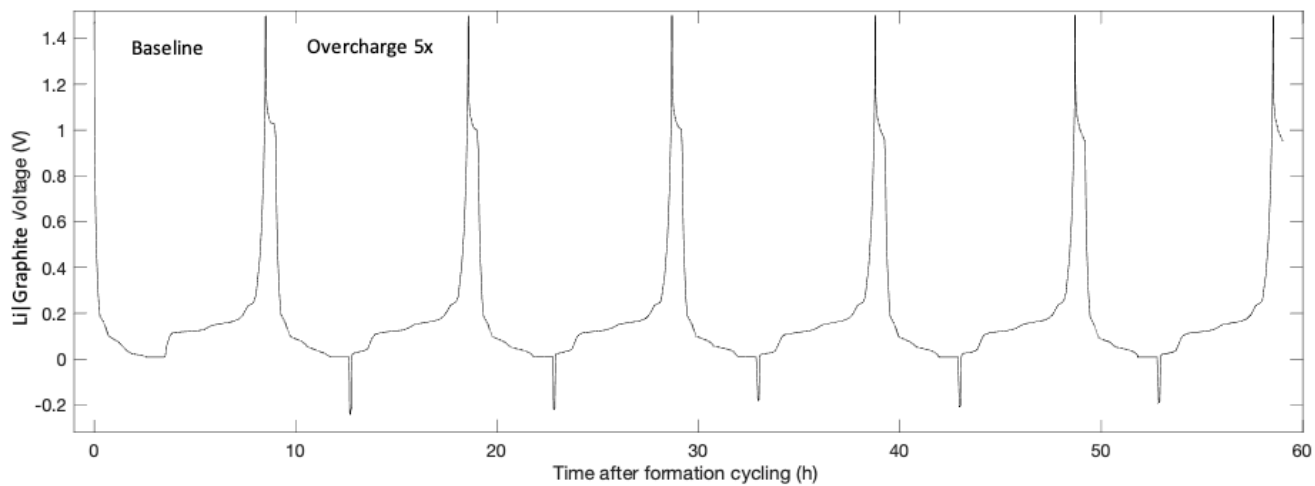
Fig. S23. Voltage vs time for representative Li plating reversibility on graphite experiment. Voltage profile vs. time after formation cycling for the 0% FEC cell that underwent 2C rate overcharge to 20%, the reversibility data for which is shown in Fig. 9c, Supplementary Fig. S24 bottom right plot.
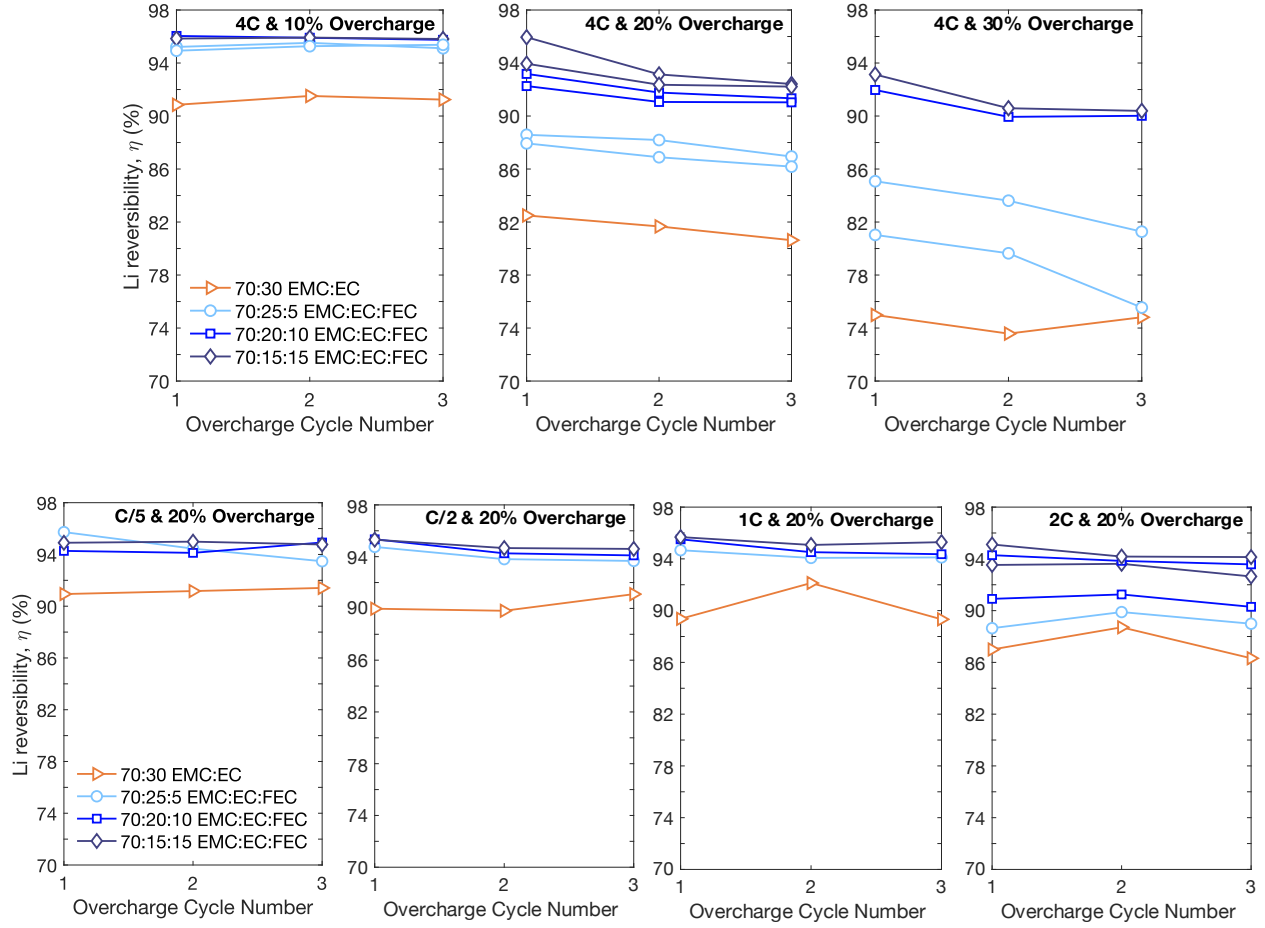
Fig. S24. Plating reversibility data from Fig. 9c dependence on overcharge cycle number. Calculated plating reversibilities are generally very constant for the first 3 overcharge cycles. The 4C, 30% overcharge (top right plot) shows that the 5% FEC (circles) reversibilities drift slightly with cycle number, which, combined with concerns of other cell aging effects, is why averages were only taken for cycles 1-3, shown here.

Supplementary Methods: The error bars for the incremental reversibility values in Fig. 9f were obtained from standard uncertainty propagation analysis below, where the $\sigma_{\eta_{20}}$, $\sigma_{\eta_{30}}$ were determined from multiple reversibility measurements recorded on the same cell (shown in Fig. 9c, above in Supplementary Fig. S24):

$$\sigma_{\eta_{10-20}} = \sqrt{\left(\frac{\partial \sigma_{\eta_{10-20}}}{\partial \sigma_{\eta_{20}}}\right)^2 \sigma_{\eta_{20}}^2 + \left(\frac{\partial \sigma_{\eta_{10-20}}}{\partial \sigma_{\eta_{10}}}\right)^2 \sigma_{\eta_{10}}^2} = \sqrt{4\,\sigma_{\eta_{20}}^2 + \sigma_{\eta_{10}}^2} \quad \text{(S3)}$$

$$\sigma_{\eta_{20-30}} = \sqrt{\left(\frac{\partial \sigma_{\eta_{20-30}}}{\partial \sigma_{\eta_{30}}}\right)^2 \sigma_{\eta_{30}}^2 + \left(\frac{\partial \sigma_{\eta_{20-30}}}{\partial \sigma_{\eta_{20}}}\right)^2 \sigma_{\eta_{20}}^2} = \sqrt{9\,\sigma_{\eta_{30}}^2 + 4\,\sigma_{\eta_{20}}^2} \quad \text{(S4)}$$
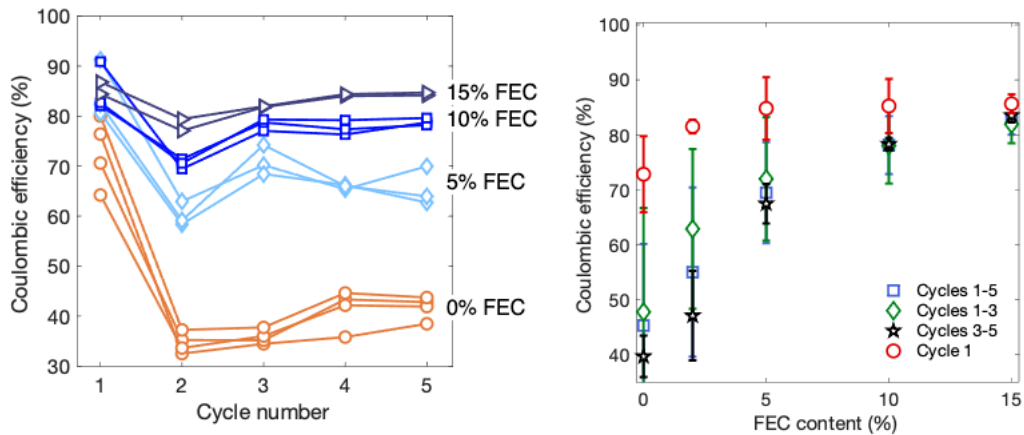
Fig. S25. Plating reversibility on copper foil dependence on cycle number. See Methods for cycling protocol.

Discussion of Fig. S25: To make a semi-quantitative comparison of lithium plating reversibility on copper foil vs. graphite in Fig. 9f, we decided to use the average of CEs from cycles 3-5 across all cells. This is because i) we expect the graphite surface at the separator interface to be more rough than pristine foil, so the transient high CE for cycle 1, which may pertain to a unique geometry or SEI formation effect, is probably best excluded, and ii) the standard deviation for averaging cycles 3-5 better depicts the reproducibility of the data set. **Right:** To show that the trends in CE are similar with respect to FEC content regardless of which cycle numbers are averaged, the plot on the right shows average CE if cycles 1-5, 1-3, and cycle 1 are considered for averaging.
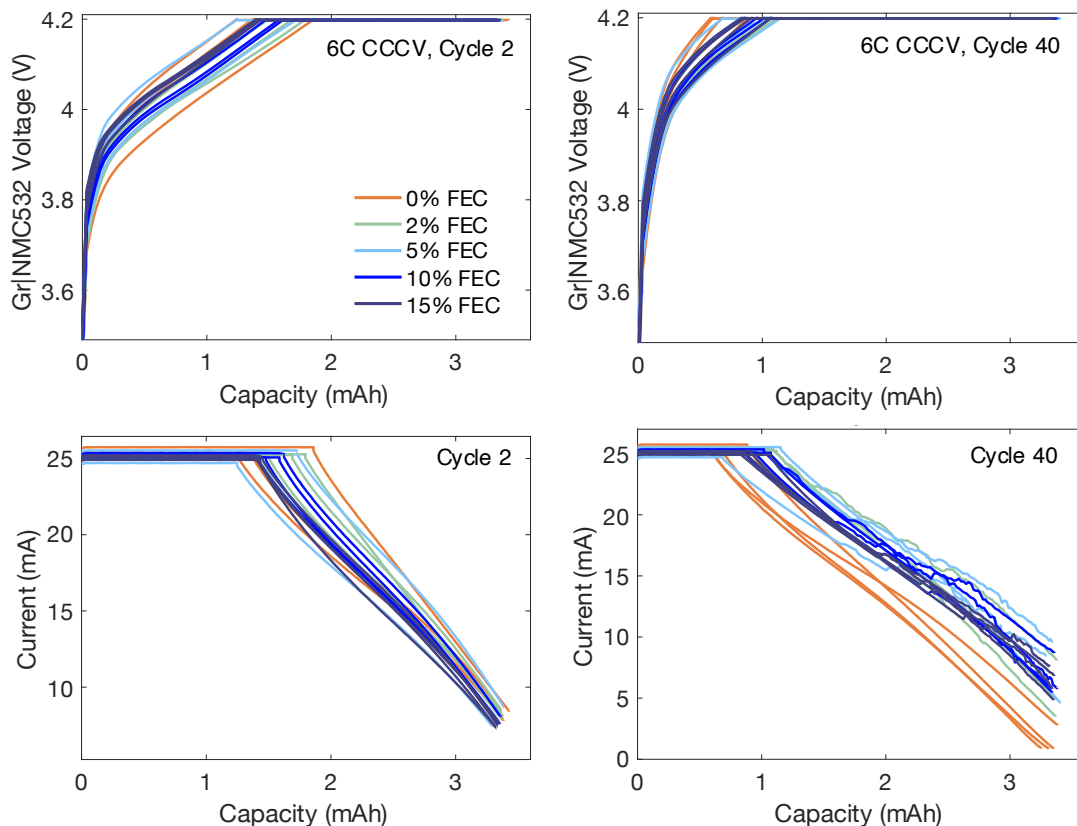
Fig. S26. 6C CCCV Fast charging voltage and current profiles, Cycles 2 and 40. The cell voltages and currents for the 2nd fast charge cycle of the Fig. 10a protocol (left) show experimental variability of overpotentials and current densities, included along with Supplementary Fig. S27 below to confirm that the performance enhancement with FEC is not an artefact of lower effective current densities (longer CCCV charge times). By cycle 40, Right, the effective charge rate for the 0% FEC electrolyte is lower due to the smaller CC portion of the charge, which arises from the significant loss of lithium inventory for those cells.
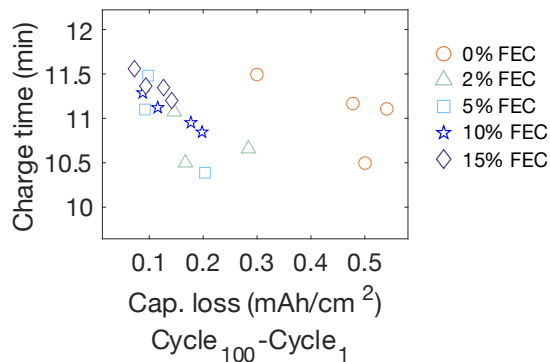
Fig. S27. CCCV fast charging times by FEC content. The charge times for the 2nd fast charge cycle of the Fig. 10a protocol, a metric inversely related to the average applied current density to 80% SOC during the CCCV charge, vs. the total 1C capacity loss of the cell. The times are reasonably constant across FEC concentrations, and the x-axis was selected to highlight that the poor 0% FEC performance is not explained by faster charge times (promoting more Li plating) compared to 2-15% FEC.
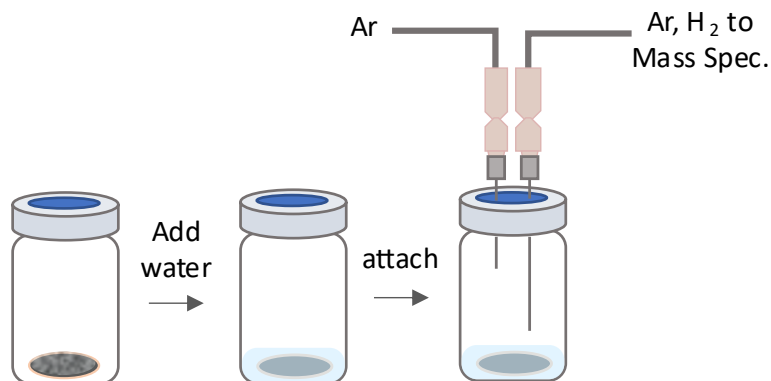
Fig. S28. Schematic of novel titration vial attachment method. Schematic of novel titration syringe attachment described in the Methods.

Discussion of titration vial attachment: Prior to each set of titrations, the system is leak tested with an in-line pressure sensor to ensure that the rate is equal to or lower than 3 Torr/min (nominal) when isolated from the gas inlet and outlet. This means that maximum 6 Torr is leaked for each 2 minute sampling period, which is less than 0.6% sample loss of the total 1030 Torr system pressure. This is an important safety and reproducibility feature. The 0.6% sample loss should be approximately constant across all vials, including the calibration data, so a correction for this is built into the calibration curve. Hamilton syringe needles with point style 5 (part # 7729-07) are used to minimize septa coring and the side port limits introduction of ambient gases during vial transfer (O_2 and N_2 mass spec signals, m/z = 32 and 28, do not increase significantly during vial swapping).
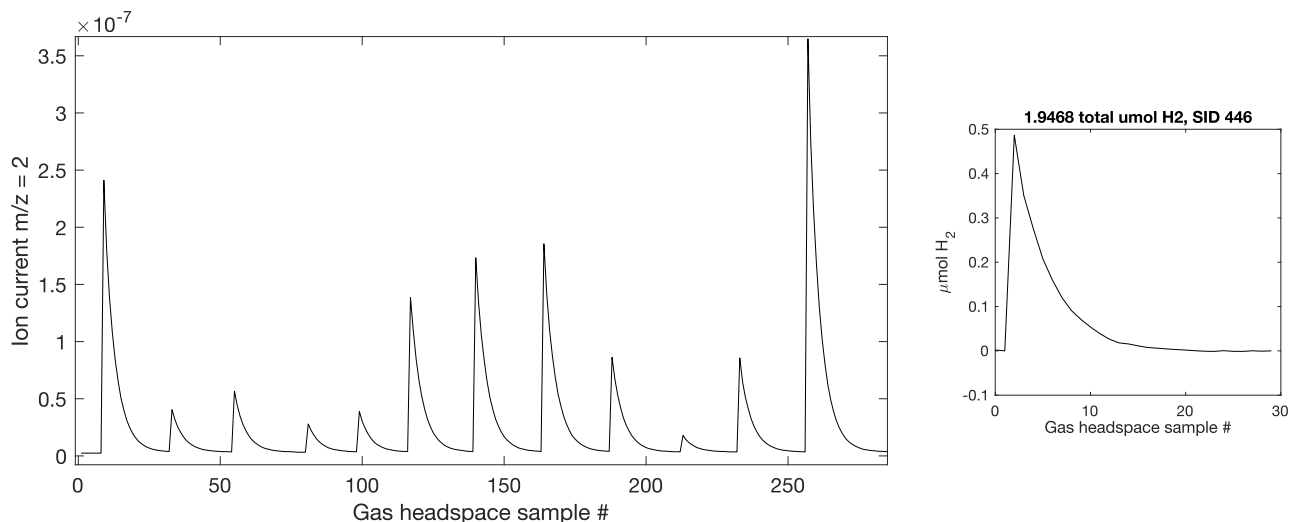
Fig. S29. Example titration data for vial-swapping method. Typical ion current for m/z = 2 (H_2) during a set of titrations. After ~99% decay of the signal for a given vial, the next vial is attached, resulting in a spike in the signal. The vial is typically swapped after about 20-25 gas headspace samples (every 2 min, total 40-50 min). To start the titration experiments, an empty Ar-filled vial is used to leak test and establish baseline ion current signals.
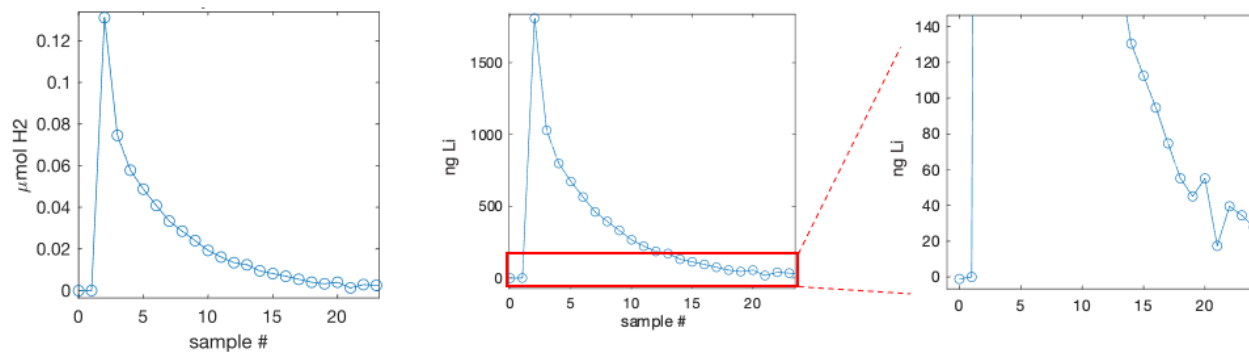
Fig. S31. Estimating the resolution of online Mass Spectrometry Titration for H₂, Li quantification. The left plot shows the μmol H_2 eluted in each of the 2 mL headspace samples for a total of 0.556 μmol. The middle plot is the same except with units of ng Li, obtained by multiplying the y-axis by (6.9·2·1000). Zooming in (right) shows that no significant signal noise is observed until approximately 30 ng Li, at which point still a mostly constant decrease is observed, suggesting that the resolution of the measurements is about 10 ng of Li.
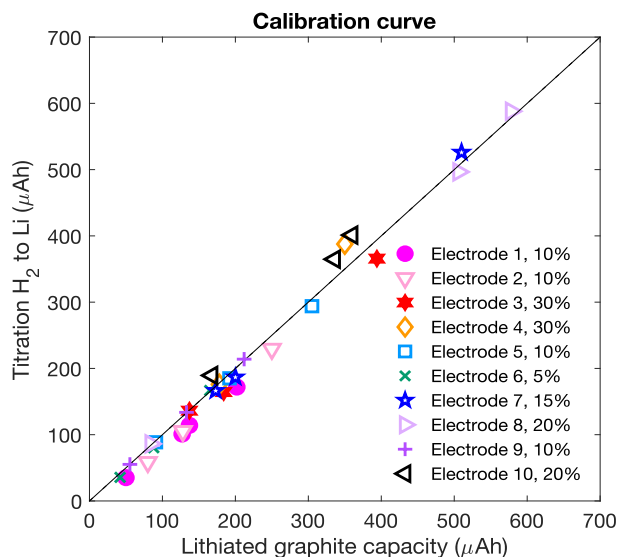
Fig. S30. Mass Spectrometry Titration calibration curve for m/z=2 generated from lithiated graphite chunks. Graphite electrodes were formed and lithiated to known SOC (10-30%) in half-cells, extracted, cut into pieces with known mass fractions of the entire 15 mm electrode, and titrated to generate the above calibration curve. Graphite pieces from the same electrode are grouped by point style. The strong linear correlation of graphite capacity with H_2, independent of graphite SOC or rinsing (filled data points were rinsed), suggests that quenching lithiated graphite is a high fidelity method for generating known amounts of H_2, and is not significantly affected by sample handling. The fluctuation around the y=x line could be due to uneven spatial lithiation of the electrode, but is not large enough to sacrifice efficiency gains by getting multiple data points per electrode. The calibration is also very consistent over months, as Electrodes 1-4 were analyzed November 2021, Electrodes 5-8 December 2021, and Electrodes 9-10 in March 2022.

54
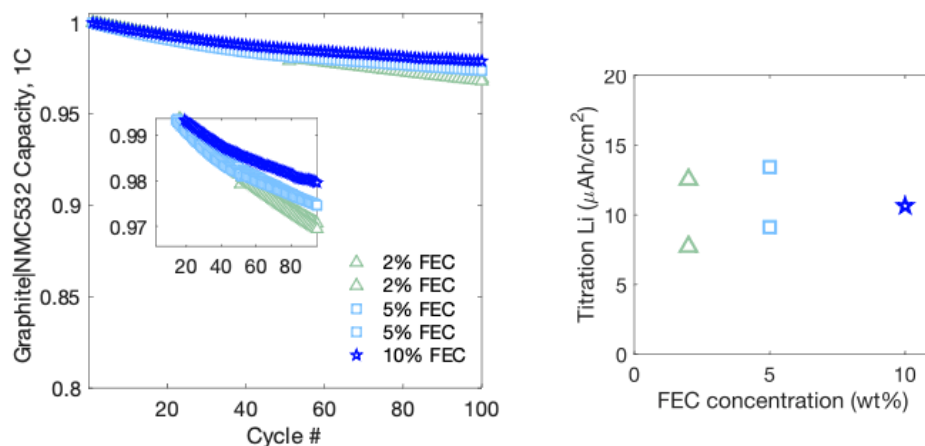
Fig. S32. 100-cycle 1C control experiments and titrations. **Left:** Only 2-3% capacity fade is observed for cells that underwent 100 1C cycles without intermittent 6C fast charging. No significant lithium plating is expected under these conditions. **Right:** Li titrated from graphite electrodes extracted from the cells in the left panel after the 100th cycle, indicating very little titrated Li, as expected. These controls averaged 10.9 ± 2.3 μAh/cm^2 (plotted with respect to 15 mm graphite electrode area, but 12.1 ± 2.6 μAh/cm^2 when normalized to active graphite material area, which is used in all other figures, see later discussion). This controls 'baseline' value is expected to be predominantly residual Li_xC_6 remaining after deep discharge and is assumed to be constant across all cells, and is thus subtracted when comparing losses ascribed to Li plating in Fig. 10c.
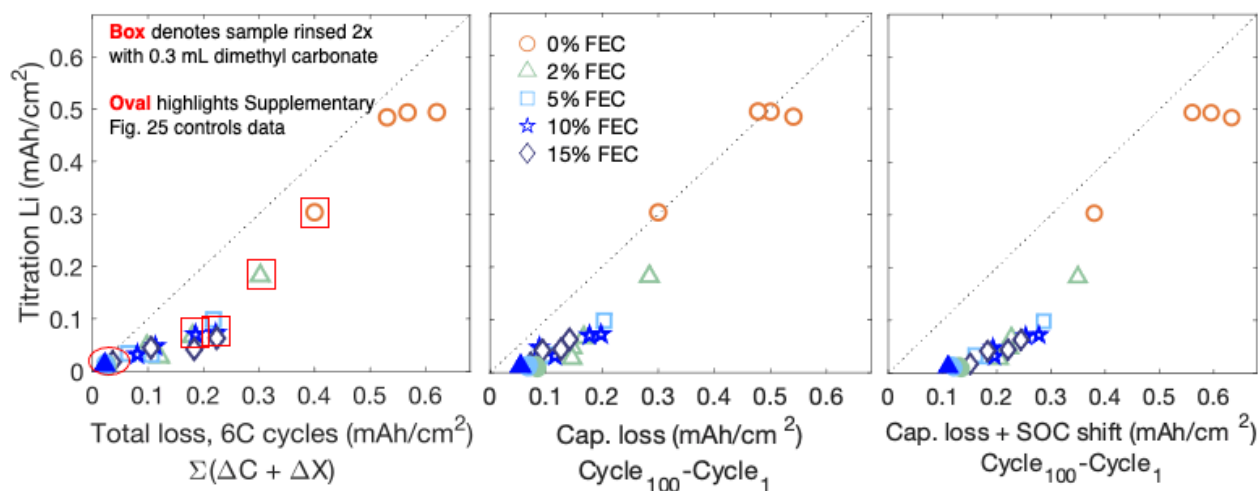
Fig. S33. Fig. 10c Titration Li correlation with various Cycling Data Loss Metrics. **Left:** This plot is the same as Fig. 10c except it shows the minimal effect of sample rinsing with dimethyl carbonate before titrations (boxes), includes the 100-cycle 1C control experiments of Supplementary Fig. S32 (filled points), and the y-values for the fast charging cells (white-filled points) are not corrected by the 0.012 mAh/cm^2 controls average baseline titration Li. **Middle:** This plot contains the same titration data from the Left plot except the x-axis is the total capacity loss observed throughout cycling, calculated from the final (100th) and initial (1st) 1C discharge capacities. The 0% FEC data points along or above the y=x line indicate that it is unlikely that capacity loss fully quantifies irreversible losses from plating or fast charging, given that reactive titration species such as electrically isolated Li^0 and Li_xC_6 are only one source of losses. **Right:** The combined total capacity loss and total graphite SOC shift over 100 cycles, the new x-axis, correlates strongly with Titration Li for the FEC-containing electrolytes, another indication that the graphite SOC shift is highly relevant for cell performance.

55
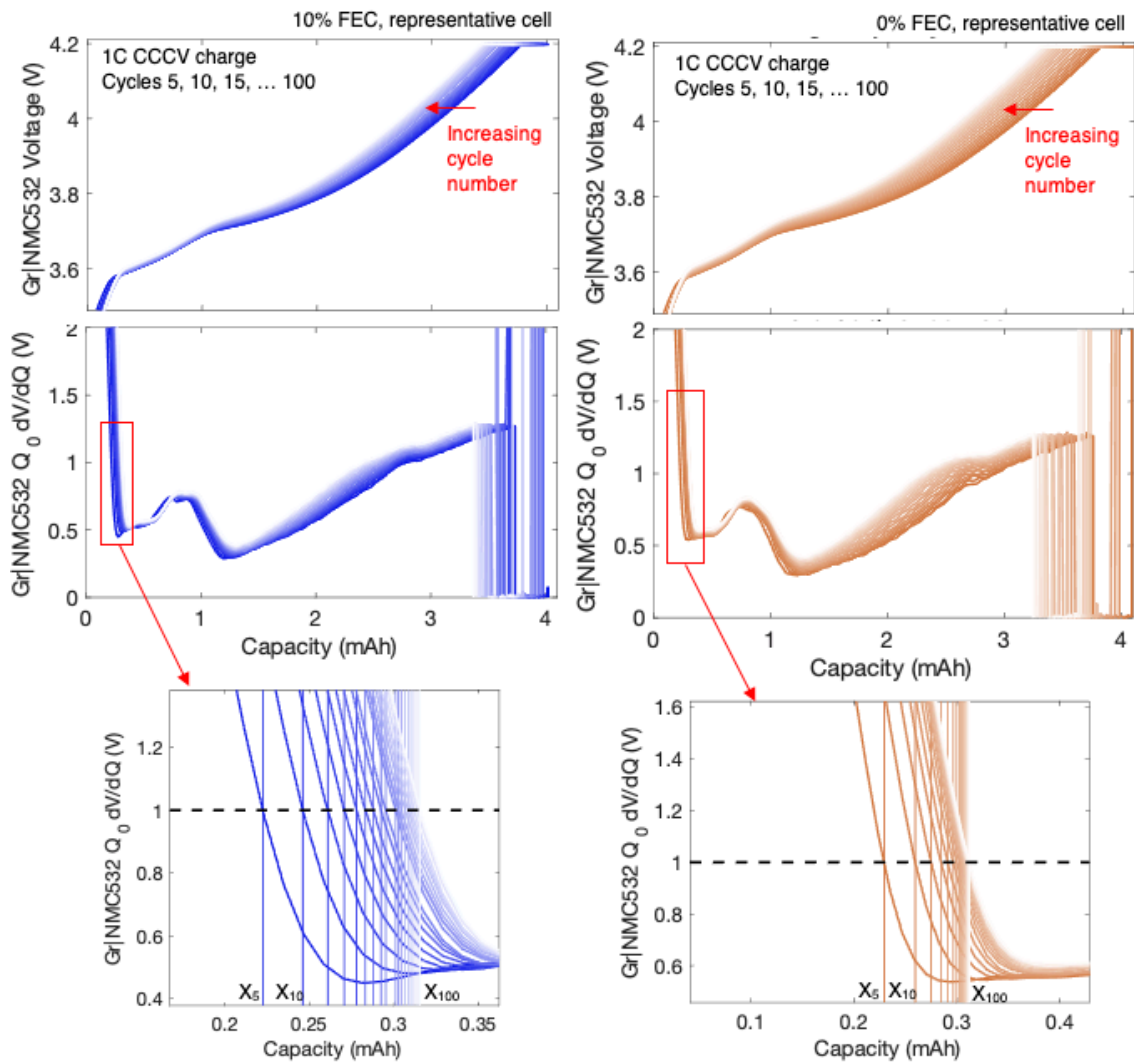
Fig. S34. 1C Cycle Voltage Profiles, Q_0 dV/dQ, and Calculating the Graphite SOC Shift ΔX. Top: 1C cycle charge profiles for the protocol of Fig. 10a. **Middle**: Differential voltage with respect to capacity (see Methods) for the corresponding 1C charge profiles. **Bottom:** Illustrating the methodology for quantifying the voltage segment shift corresponding to early graphite lithiation. The capacity at which Q_0 dV/dQ = 1 for each curve is shown by the horizontal lines, X_5 … X_{100}, and these values are used to calculate the Graphite SOC Shift ΔX as described in the Methods. Using this criterion to calculate curve shifts avoids the noise, error, and algorithm complexity of assigning capacities to local extrema (peaks or troughs) in the Q_0 dV/dQ curves.
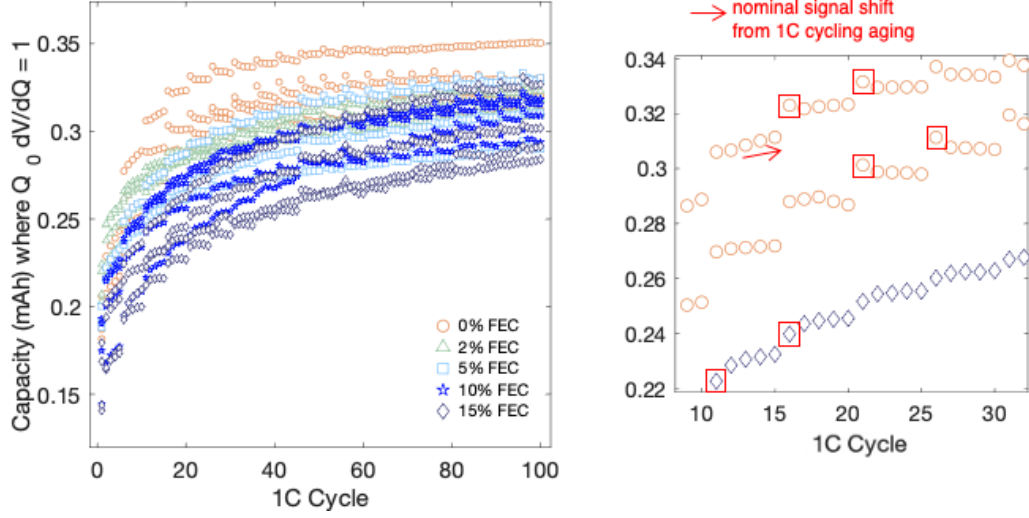
Fig. S35. Graphite SOC shift calculation from 1C cycles. The left plot shows capacity at which $Q_0 \, dV/dQ = 1.0$ V, denoted X_i in Supplementary Fig. S34 and the Methods (i is the 1C cycle number), for each 1C charge for all cells included in the study. The enlarged region in the right plot highlights in red boxes that the 1st 1C cycle following 6C CCCV fast charge (cycles 6, 11, 16, …) shows transient behavior, which is why the value for the 2nd 1C cycle following fast charge (cycles 7, 12, 17, …) is used for the ΔX as described in the Methods, equations below for reference. The arrow highlights nominal X_i change from 1C cycling, which is why this change over 2 cycles (from N-2 to N, below) is subtracted from the ΔX for the 2 6C cycles to distinguish contributions related to fast charging from nominal cell aging/formation.

$$\Delta X_{6C \; cycles \; 1 \, \& \, 2} = (X_7 - X_5) - (X_5 - X_3) \qquad (S5)$$

$$\Delta X_{6C \; cycles \; n \, \& \, (n+1)} = (X_{N+2} - X_N) - (X_N - X_{N-2}) \qquad (S6)$$

For 1C cycle numbers: N = [5, 10, 15, …, 90, 95] and
Corresponding 6C cycle numbers: n = (2N/5) - 1 = [1, 3, 5, …, 35, 37]

57
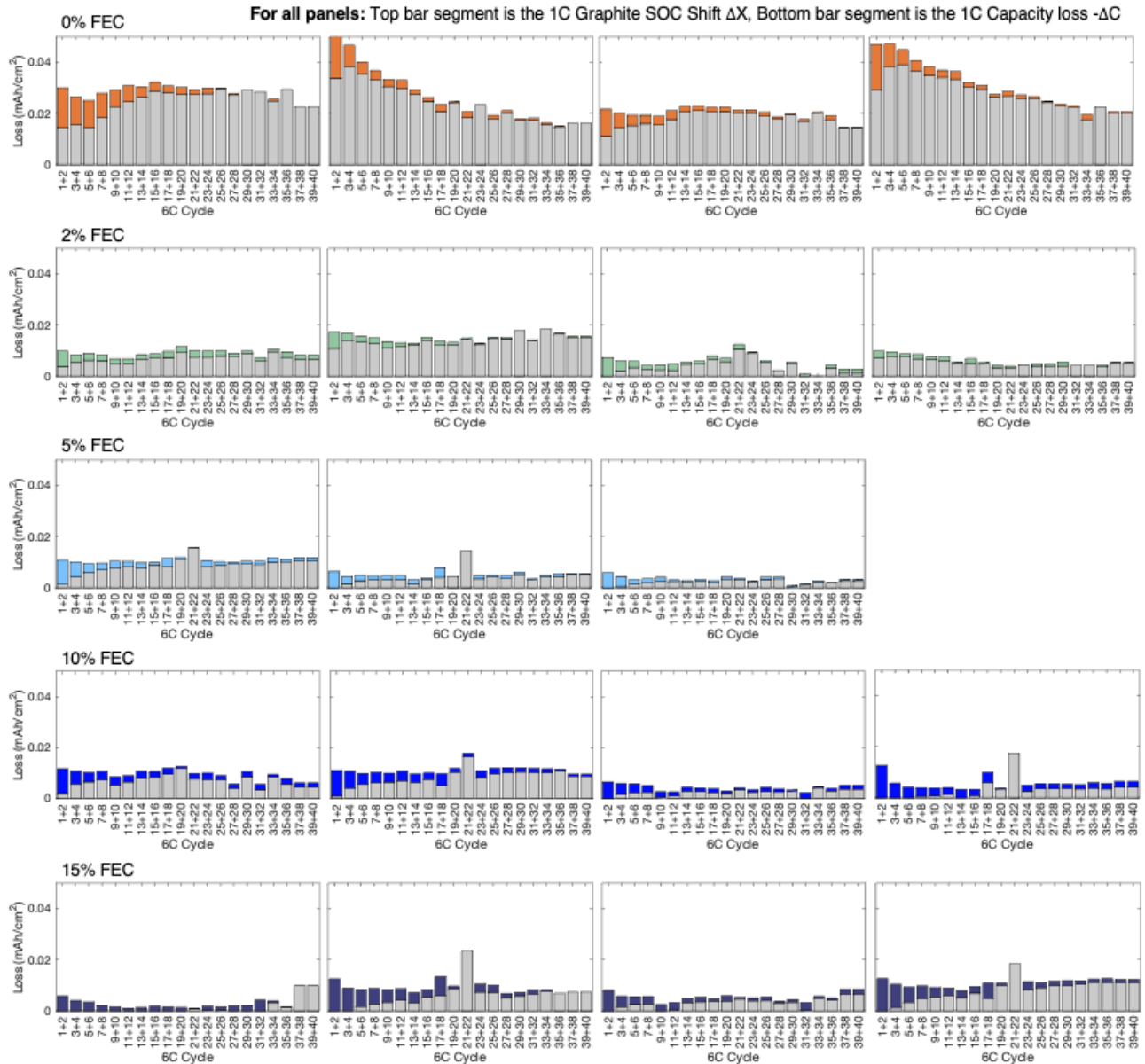
Fig. S36. Capacity loss and Graphite SOC shift by fast charging cycles, all cells. Plots analogous to main text Fig. 10c are shown for all individual cells studied in Fig. 10, grouped by electrolyte concentration. The combined loss of the graphite SOC shift (grey bars, bottom) and the capacity loss (colored bars, top) is remarkably constant or decreasing, as expected and described in the main text, for nearly all cells. This evidence promotes the reliability of these combined metrics to quantify fast charging and Li plating-related loss. Future work could incorporate outlier removal for plating quantification; the data blip for cycles 21+22 for a few cells is due to temporary thermal chamber temperature increase to ~32ºC at that time due to laboratory air conditioning maintenance, when the warm ambient air makes it difficult to cool the oven temperature to 30.0 during heating-only operation.
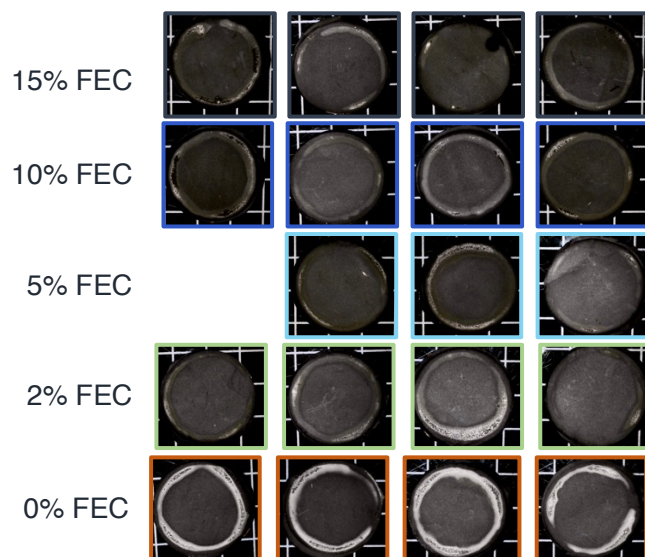
Fig. S37. Graphite electrode images before mass spectrometry titrations. The 0% FEC electrodes from Fig. 10 experiments show much more prominent metallic lithium, motivating the desire to quantify the amounts with titrations. These images also confirm that plating is occurring on the graphite electrode, and not on the spacers behind it, a testament to good electrode alignment and cell fabrication. We believe that the ring shape of plating is due to higher current densities passed near the edge of the undersized NMC electrode (14 mm vs. 15 mm graphite), and is not (at least primarily) a pressure effect from the coin cell spring.
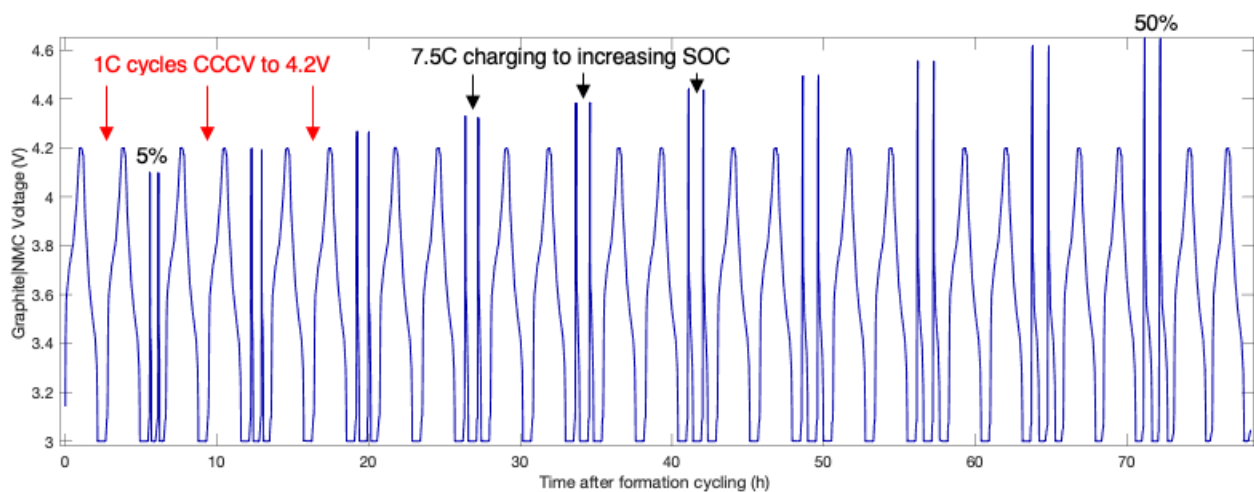
Fig. S38. Gr|NMC voltage during SOC-sweep cycling protocol. This figure illustrates the protocol of alternating 1C cycles with fast charging cycles to different SOC cutoffs, described in the main text and Methods. This data corresponds to 7.5C fast charging ranging 5% SOC (first cycles) to 50% SOC (last cycles).
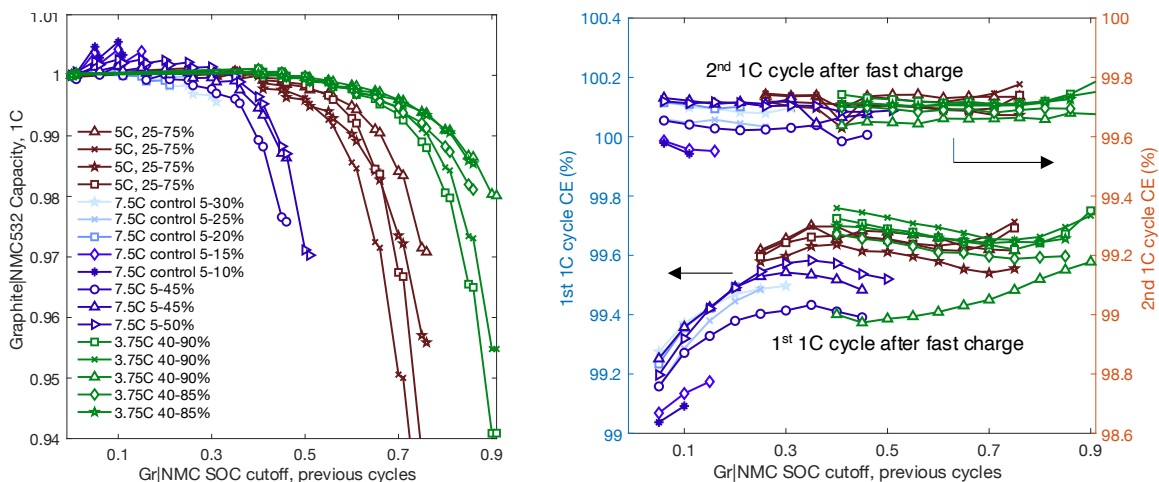
Fig. S39. SOC-sweep 1C discharge capacities and coulombic efficiencies. **Left:** Main text Fig. 11a plot including data from all cells (each unique curve). For many curves, there is significant capacity change observed within each pair of 1C cycles (adjacent points), which is unexpected from previous 100-cycle experiments. We believe the 1C cycle immediately after fast charge has transient anomalous behavior, which was also seen and discussed for the similar protocol in Supplementary Fig. S35, and thus only the 2nd cycle of each pair was used for quantitative analysis. **Right:** The 1C cycles immediately after the fast charging pair (bottom) show drifting CE values between 99.2-99.7% throughout cycling. The 2nd cycle after fast charging (top) shows fairly stable CE between 99.6-99.8%, suggesting stabilized cell behavior desirable for precise discharge capacity analysis.
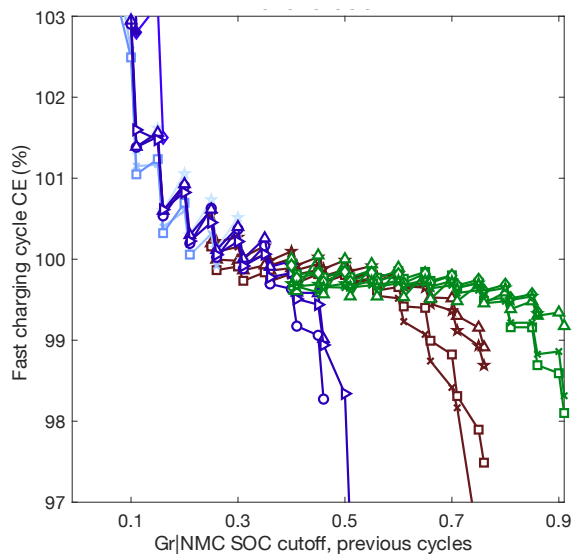
Fig. S40. SOC-sweep fast charging cycle coulombic efficiencies. This plot shows the intermittent fast charging cycle coulombic efficiencies corresponding to Supplementary Fig. S38-Fig. S39 and Fig. 11. Unlike the CEs used to quantify irreversible Li plating in in Li|Gr cells, these values can frequently be greater than 100% and do not exhibit a stable baseline (as in Supplementary Fig. S8) prior to a decrease that indicates the clear onset of irreversible plating. This highlights the benefit of the stable potential of lithium counter electrode in half-cells and is why the 1C cycle discharge capacities and graphite SOC shift are analyzed instead of the fast charging cycles.

60

Rate	μAh Li estimate, nonzero slope baseline	μAh Li estimate, horizontal baseline	μAh Li estimate difference (%)
7.5C	150.4	165.2	9.8
5C	267.2	294.9	10.4
3.75C	184.9	205.8	11.3
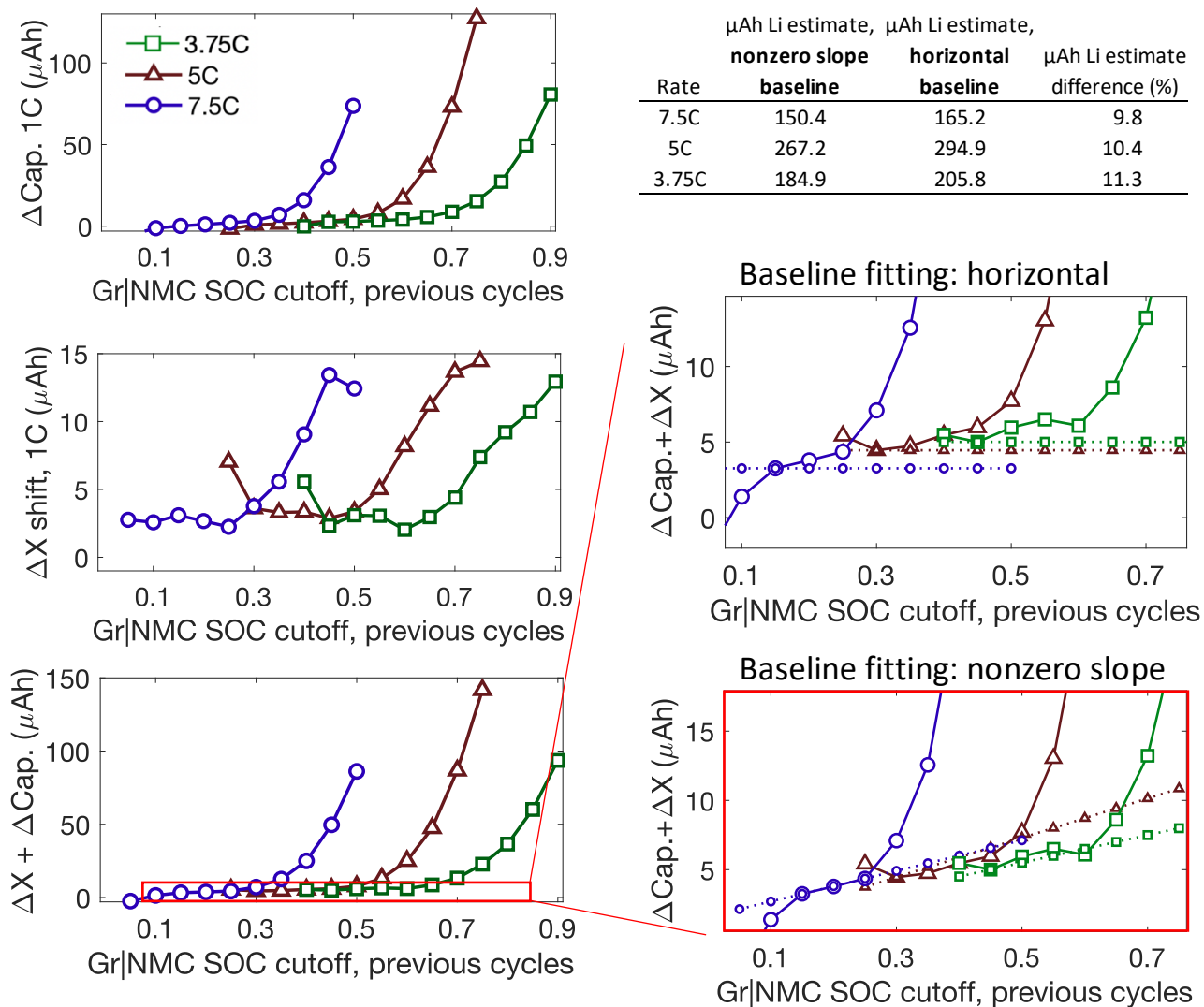
Fig. S41. Estimating irreversible Li from ΔX and ΔC obtained from the SOC-sweep protocol. Left: The individual contributions of capacity loss (ΔC) and graphite SOC shift (ΔX) to the combined loss shown in Fig. 11a. Interestingly, ΔX alone also shows a clear increase at the SOC where the onset of lithium plating is expected, but with lower sensitivity than ΔC (note ~10^1 y-axis scale difference). However, these contributions are significant for quantifying total irreversible lithium plating. **Right**: To isolate irreversible lithium plating from other nominal cell degradation, we subtract baseline losses for each (ΔC+ΔX) data point using a linear baseline with slope > 0 that passes through the data points at low SOC. Each cell (dotted lines) has a unique baseline with nonzero slope, shown in the red box.

Discussion of baselining protocol: This baselining protocol is conceptually equivalent to the previous half-cell CE baselining, which instead uses a singular CE value, because the capacity loss is scaled by the charge capacity by definition of the coulombic efficiency. Fig. S42 below illustrates this point by recasting half-cell data into capacity loss units instead of CEs. Physically, this means that most experimental cells herein exhibit an SOC-dependent fast charge aging likely related to continued graphite SEI formation or electrode de-wetting, but also possibly related to counter electrode (NMC or Li) performance, beyond nominal aging such as that from the 2 1C cycles for this SOC-sweep experiment.

To gauge the sensitivity of the cumulative irreversible plating estimate (Fig. 11c, x-axis) to baseline fitting, we calculate this plating estimate for the extreme case of a horizontal baseline that has no SOC-dependence on nominal cell aging (middle) and show the values in the table. Using the horizontal baseline gives an approximately 10% overestimate for the plating amount across these representative cells, suggesting this is the maximum possible error due to baseline fitting. However, the control experiments in Supplementary Fig. S43 show no titration Li below 0.3 SOC for the 7.5C charging, suggesting no irreversible Li plating, which further supports the nonzero slope baselining approach that gives zero irreversible plating at those SOC in addition to the half-cell justification. From this discussion, we believe the baseline fitting error of irreversible Li quantification is much smaller than 10%, likely in the range of 2-3%.

Finally, the baselined data were then divided by 2 (2 fast charging cycles to each SOC), and normalized to the active graphite capacity, $C_{active\_graphite}$ (5.24 ± 0.07 mAh determined from dV/dQ analysis of 5 cells, Supplementary Fig. S44). The irreversible Li values at low SOC were set to 0 to remove data noise artefacts, and the cumulative Li plating capacity estimate (x-axis, (Fig. 11c) excluded these points.
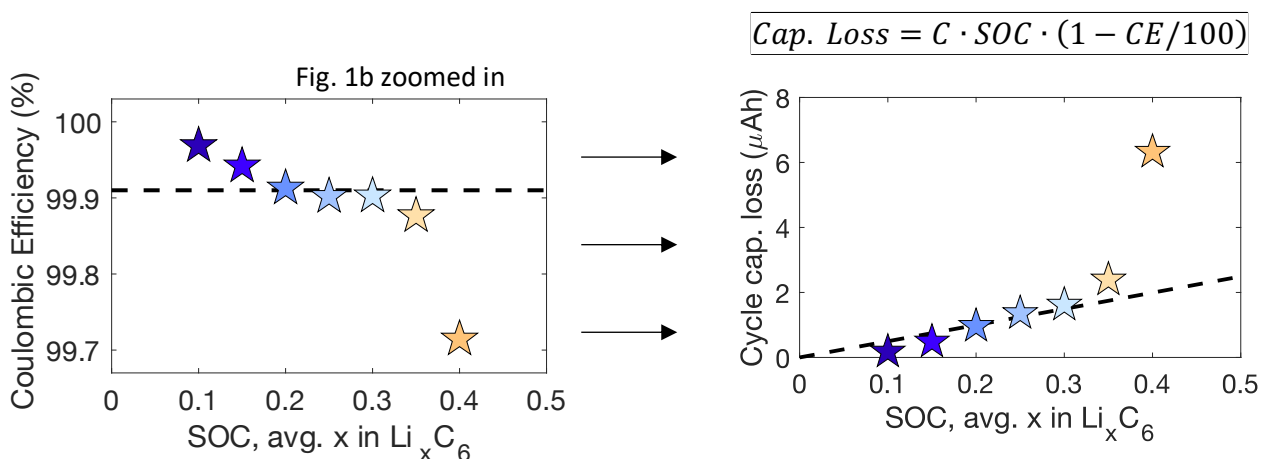
Fig. S42. Half-cell CE baselining for SOC-sweep protocol recast in irreversible capacity units. Converting the CE data of Fig. 7b (left) to capacity loss (right) illustrates how using a horizontal baseline for CE analysis [y = 99.91] is equivalent to using a nonzero slope baseline with capacity units [y = C·SOC·(1-0.9991)], where C is the experimental cell capacity. This further justifies the use of a nonzero slope capacity baseline for the full-cells plating analysis, in which coulombic efficiencies for the fast charging cycle cannot be analyzed due to unpredictable artefacts seen in Supplementary Fig. S40.
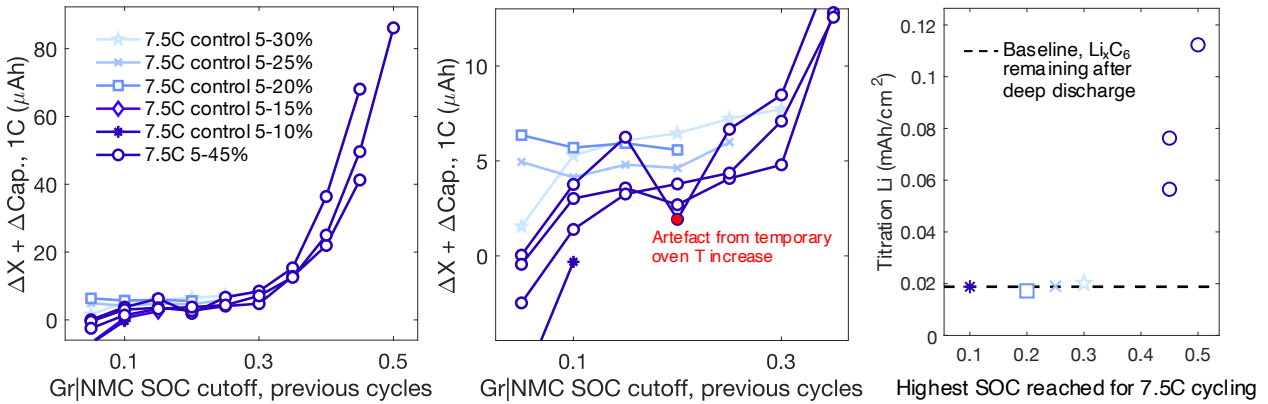
Fig. S43. SOC-sweep control experiments: titration results for cycling at 7.5C to low SOC. Left: (ΔX+ΔC) data for all 7.5C fast charging cells, including control experiments that started cycling at 5% SOC but were stopped at various points during the protocol. **Middle**: Zooming in on the left data shows that the control cells also show the characteristic increase in (ΔX+ΔC) capacity with continued cycling to higher SOC. The filled data point, collected when the oven temperature fluctuated up to ~32ºC from 30ºC, emphasizes the importance of temperature control for precisely quantifying small amounts of irreversible lithium. **Right:** The titrated Li for these cells shows a very constant baseline (dashed line) that should correspond predominantly to Li_xC_6 remaining after the deep discharge step of the protocol. This value is 0.019 ± 0.001 mAh/cm^2, and the cells with significant expected irreversible Li (circles) show titrated Li much greater than the baseline.
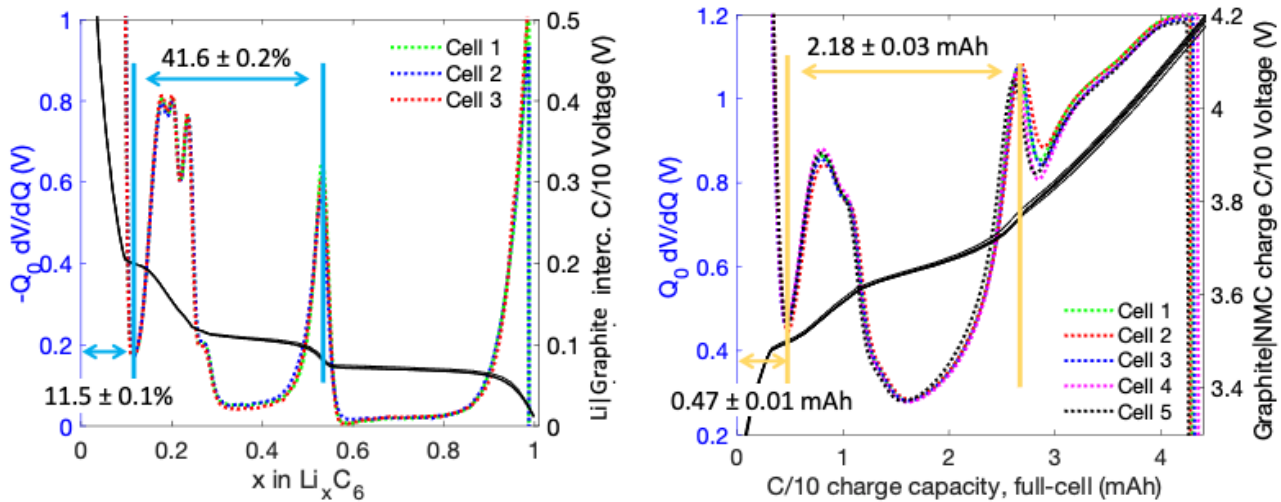
Fig. S44. Using dV/dQ analysis to determine active graphite capacity and lithiation in full-cells. Left: C/10 intercalation voltage (black) to 0.01 V for the 3rd C/10 formation cycle of 3 representative Li|Graphite cells, using the graphite electrode A3 (see Materials section in Methods) and 0% FEC electrolyte. The capacity is normalized to 1 (x-axis). The average normalized capacity up to the first trough in the -Q_0 dV/dQ signal (dotted, colored curves) is $11.5 \pm 0.1\%$, and the capacity between the trough and the clear peak (near x = 0.5) is $41.6 \pm 0.2\%$. These features related to graphite phase change are also visible in the Q_0 dV/dQ analysis during full-cell charging (Right). **Right**: C/10 full-cells charging voltages (black) for the cycle immediately preceding the fast charging SOC-sweep for 5 representative cells (see Methods for protocol), overlaid with Q_0 dV/dQ. The capacity between the first trough and the clear peak (near 2.6 mAh) is 2.18 ± 0.03 mAh. Assuming similar graphite phase behavior at these low rates in the full-cells as to half cells, this amount is 41.6 % of the active graphite material, and on average, 2.18/0.416 = 5.24 mAh is the active graphite capacity in the full-cell configuration. The graphite lithiation at the start of C/10 charge (equivalently, the lithiation at the end of the 1C discharge with 3V hold until C/20) can be calculated from this value and the capacity up to the first trough, 0.47 ± 0.01 mAh, assuming that the trough corresponds to 11.5% graphite lithiation as observed in half-cells. From this, the initial average graphite lithiation in the full-cells is $2.5 \pm 0.1\%$, calculated from (0.115*5.24 – 0.47)/5.24.

63

Supplementary Note 2. Calculating Gr|NMC C-rates to get the same effective graphite current densities as in Li|Gr cells

The NMC electrode in the full-cells was slightly undersized to avoid edge effects like lithium deposition on the stainless steel spacer behind the graphite electrode. To compare irreversible lithium plating in full-cells and half-cells, however, the effective current density applied to the graphite electrode during charge should be fixed. This calculation needs to take into account what area of the 15 mm diameter graphite electrode is actively lithiated and delithiated during cycling. Prior to the above analysis of Supplementary Fig. S44, the below diagram was constructed to help visualize relevant cell length scales to make a reasonable estimate for how much of the graphite

175um sandwich thickness

80 um   NMC
25 um
70 um   Graphite   Overhang

~500um overhang

After C/10 lithiation to 4.2 V in full-cell
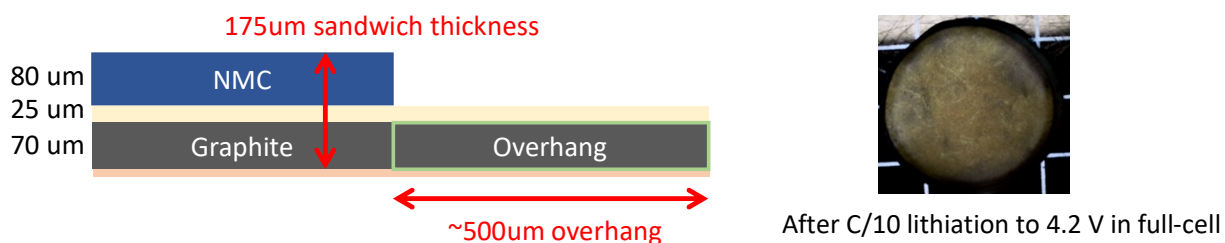
'overhang' region may be active or utilized for the case of perfectly concentric electrodes. We reasoned that 50% of the overhang region might be utilized, or 14.5 mm of the 15 mm diameter graphite in total, due to expecting full wetting of the electrodes and separator with electrolyte. From this assumption and knowledge of the average observed capacity for 15 mm A3 graphite in the half-cells, 5.90 mAh, we multiplied this by the area ratio of (14.5 mm dia.)/(15 mm dia.) = 0.934 to estimate there is 5.5 mAh active graphite in the full-cells. In other words, if the 1C rate in half-cells is 5.9 mA, then the equivalent total current used in the full-cells should be 5.5 mA. Finally, the average full-cells experimental capacity based on the 3rd C/10 formation cycle to 4.2V was 4.30 mAh, indicating that the 1C rate in full-cells is 4.30 mA, so to get the desired 5.5 mA corresponding to 1C rate in half-cells, the full-cell rate should be multiplied by a factor of (5.5/4.3) ~ 1.25. This factor was used to select full-cell rates [3.75C, 5C, 7.5C] corresponding to [3C, 4C, 6C] rates in the half-cells in Fig. 11.

However, after the Supplementary Fig. S44 analysis, a more accurate estimation of the active graphite material was determined to be 5.24 mAh compared with the 5.5 mAh calculated from the 50% overhang utilization assumption. Imaging the graphite electrode after C/10 lithiation to 4.2V in the full-cells also shows significant overhang region that does not show the gold-colored LiC_6 (see image below), giving support for the fidelity of the dV/dQ analysis capacity of 5.24 mAh (instead of 5.9 or 5.5 mAh), which would correspond to only a ~14.2 mm diameter circle of the graphite being utilized. This means that the graphite current densities in the full-cells are likely (1-5.24/5.5) = 5% higher than those applied in the half-cells due to error in the 1.25 factor used to convert between C-rates. This offset is significant but not expected to affect the trends and conclusions drawn in the Fig. 11e comparison of half- vs. full-cells, because the empirical fitting from Eqn. 5 and Table 2 indicates that a 5% change in current rate for the half-cells will only affect the plating onset SOC by ~2% for a 3.25 mAh/cm^2 electrode with 4C rate at 30 ºC.
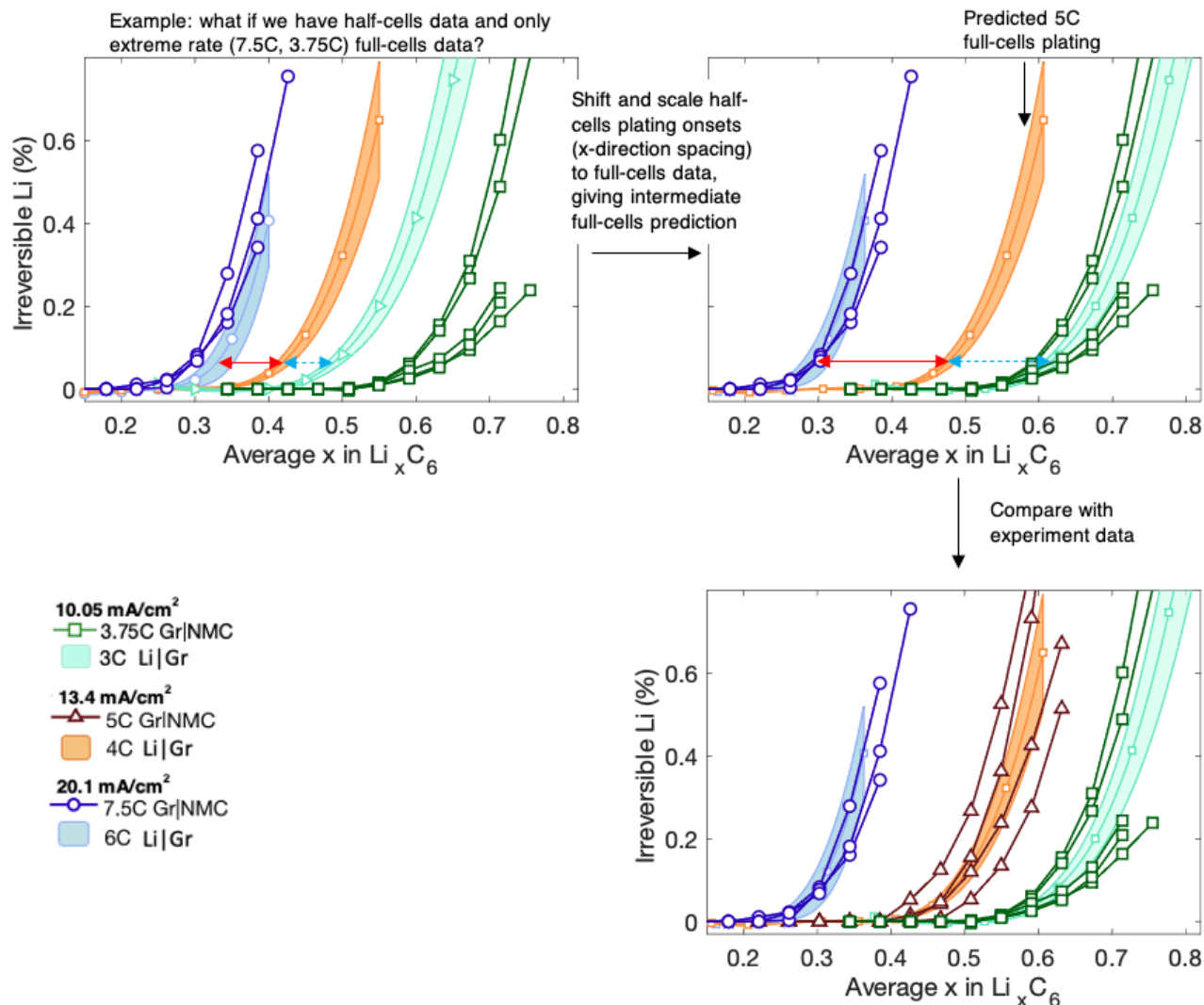
Fig. S45. Scaling half-cell irreversible Li plating data to predict full-cell data with limited measurements. **Top Left**: Replicated Fig. 11b except without the 5C Gr|NMC full-cells data. In all panels, the experimental Gr|NMC data is fixed and shown for reference/comparison. The SOC spacing between the half-cells data (arrows) is scaled such that the spacing between 3C and 6C becomes the same as the spacing between full-cells 3.75C and 7.5C. The curves are then shifted so that the corresponding half/full-cell extremes overlap (3C with 3.75C, 6C with 7.5C), and this transformation result is shown in the **Top Right** figure. The scaled 4C half-cell curve (shaded orange) is now a prediction for Li plating at 5C rate in the full-cells. **Bottom:** Overlaying the 5C full-cell experiment data shows excellent match with the half-cell-based prediction, suggesting that half-cells data and models may be adjusted to predict full-cells behavior with limited full-cells data to provide corrections. For this analysis, plating onsets were again defined as the average x-value where the curves cross the y=0.05 threshold.

Supplementary Note 3. Understanding the observed differences in half-cells and full-cells

The differences for lithium plating onset between full-cells and half-cells is multifaceted. At high current densities, the full-cell plates lithium at lower SOC compared to half-cells. Conversely, at moderate current densities, the half-cell plates lithium at lower SOC compared to full cells, which is somewhat unexpected. A detailed electrochemical model was run in full-cell configuration using NMC properties previously reported[11], and the same complex behavior is predicted for lithium plating onset when comparing configurations. Upon studying model results, the earlier onset for half-cells at moderate current densities seem to be related to the functional form of electrolyte properties with concentration and the relatively flat open circuit potential for graphite. The electrolyte potential drop, which effects SOC heterogeneity, is a function of both electrolyte ionic conductivity and diffusivity. During charging, ion concentration drops in the anode. This results in a decrease in ionic conductivity but an increase in diffusivity. The ion concentration in the anode during charging is lower in full-cells compared to half-cells. At moderate rates, the full-cell seems to be delayed in lithium plating compared to half-cells due to gains in electrolyte diffusivity outweighing a slight drop in ionic conductivity (Fig. 1 in Ref. [11]). However, at high current densities, lithium plating occurs earlier in full cells because severe ion depletion occurs more and the ionic conductivity for large sections of the anode goes to zero. Thus, decreases in ionic conductivity outweigh gains in diffusivity at high current densities when comparing cell setups.

Supplementary Note 4. Calculating the Li:Gr molar ratio of half-cells and influence on performance

The median graphite electrode loading used in this work was 3.1 mAh/cm^2 , which has capacity of 5.5 mAh for a 15 mm diameter punch. The lithium metal used was a 14 mm diameter punch (1.54 cm^2) with 0.75 mm thickness. Thus, the total theoretical capacity of the lithium metal electrode is:

$$(0.075 \ cm \ thick) \cdot (1.54 \ cm^2 \ area) \cdot \left(0.5 \frac{g \ Li}{cm^3}\right) \cdot \left(\frac{1 \ mol}{6.9 \ g \ Li}\right) \cdot \left(96485 \frac{C}{mol \ e^-}\right) \cdot \left(\frac{mAh}{3.6 \ C}\right) = 223 \ mAh \quad \text{(S7)}$$

Therefore, on average, the molar ratio is about 223/5.5 ~ 40 Li:1 Gr, and does not go below 34:1 for the highest loading 3.6 mAh/cm^2 graphite. This is extreme excess; the lithium thickness was selected for ease of handling and supplier availability. We believe the protocol would work with much less Li.

Next, we conservatively estimate the capacity of irreversible Li formed at the Li metal electrode throughout the SOC-sweep protocol, assuming: 15 cycles, an average of 40% graphite capacity passed per cycle (~2 mAh), and 40% irreversibility for the plating/stripping of Li metal (should be higher due to the low ~0.6 mA/cm^2 plating current density on Li metal, see Ref. [49] Fig. 1b, CCE electrolyte)

(15 cycles) $\cdot$ (2 mAh/cycle) $\cdot$ (0.4 irreversibility) = 12 mAh irreversible Li per cell

which gives the molar ratio of about 2.2 Li$_{irrev}$:1 Gr compared with the average 40 Li:Gr ratio in this work. Thus, we expect the quantity change to not influence results and expect much lower thicknesses of Li metal, on the order 0.2 mm instead of 0.75 mm, to provide sufficient lithium for these experiments.

Supplementary Note 5. Discussion of ambient temperature vs. fast-charging internal cell temperature

In the authors' previous thermal analysis of single-layer pouch cells using a similar Gr-NMC cell at rates of 1C-9C, the maximum computed temperature rise from 30°C was 5°C [Ref. [11] Fig. 7a-b]. In the coin cells of this work, the high thermal mass and thermal conductivity of the stainless steel spacers, case and spring relative to the active material make us believe that the experimental temperature rise would be even lower. According to our Table 2 analysis, a ~3°C increase in temperature from ambient would only change the plating onset by 2% SOC, giving us confidence that the conclusions of the study would still hold even if the data would shift slightly if measured temperatures were a few degrees higher than ambient.

Supplementary Note 6. Deciding on method for Graphite SOC shift calculation

Calculating the graphite SOC shift (ΔX), limited data points collected during 1C charging made it difficult to use dV/dQ peak positions, which are broader at the 1C charging rate, with the precision required for the analysis. Instead, we selected the x-position where the quantity Q_0 dV/dQ equals 1.0 V as the feature to monitor SOC shifting (Supplementary Fig. S34), because it occurs in the low-voltage regime of interest and precisely reports the change to ~1 µAh (Supplementary Fig. S35, Left). The value of 1.0 was selected arbitrarily and visual inspection of Supplementary Fig. S34, bottom, suggests any value between 0.8-1.2 V would give identical results. Supplementary Fig. S35 shows that significant SOC shift occurs from 1C cycling alone during the first ~30 1C cycles, and that the 1C cycle immediately following fast charging often has a value uniquely higher than cycles 2-5 after fast charging. The $(X_5 - X_3)$ correction subtracts any SOC shift anticipated from nominal cell formation or aging processes that occur in 2 1C cycles from the change observed over the 2 fast charging cycles.

Supplementary Note 7. Uncertainty analysis for converting full-cell SOC to graphite lithiation

$$x \text{ } in \text{ } Li_x C_6 = x_{initial} + SOC_{full-cell} \cdot \frac{C_{full-cell}}{C_{active\_graphite}} \qquad \text{(S8)}$$

Although Supplementary Fig. S44 analysis determined that $x_{initial}$ is 0.025 ± 0.001, this value is known to decrease throughout cycling because ΔX is consistently positive for each set of fast charging cycles (Supplementary Fig. S41). Integrating ΔX gives a total capacity shift throughout cycling, and dividing by $C_{active\_graphite}$ shows that the total decrease in initial lithiation is about 0.015. For the Li plating cycles that happen near the end of the protocol, we expect the average decrease in lithiation from the start to be about 0.01 ± 0.003, assumed to be a constant value to simplify analysis. Thus, $x_{initial}$ is presumed to be $(0.025-0.01) = 0.015 \pm 0.003$. Combining the uncertainty contributions of $x_{initial}$ and $C_{active\_graphite}$ to $x \text{ } in \text{ } Li_x C_6$, the maximum uncertainty expected in the x-axis for Fig. 11b, at $SOC_{full-cell} = 0.9$ is:

$$\sigma_{x\,in\,LixC6} = \sqrt{\left(\frac{\partial x_{in\,LixC6}}{\partial x_{initial}}\right)^2 \sigma_{x_{initial}}^2 + \left(\frac{\partial x_{in\,LixC6}}{\partial C_{active_{gr}}}\right)^2 \sigma_{C_{active_{gr}}}^2} \quad (S9)$$

$$= \sqrt{\sigma_{x_{initial}}^2 + \left(\frac{-0.9 \cdot 4.3}{5.24^2}\right)^2 \sigma_{C_{active_{gr}}}^2}$$

$$= \sqrt{0.003^2 + \left(\frac{-0.9 \cdot 4.3}{5.24^2}\right)^2 0.07^2} = \mathbf{0.010}$$

Supplementary Note 8. Calculating H2 quantities from m/z = 2 ion current data

To calculate H_2 amounts from the online MST system, the following steps are taken and are based on previously developed knowledge of mass spectrometry application for titration experiments[39,75]. First, a value proportional to the H_2 mole fraction in the gas outlet, $\alpha \cdot y_{H2}$, where α is a proportionality factor, and is calculated from the ratio of m/z = 2 to m/z = 36 (Ar). We will denote this ion current signal ratio as $S_{2/36}$. Next, a linear baseline is applied to this data such that the first and final data points for each vial are 0, giving $S_{2/36,baselined}$. Then, the total system pressure P_{sys} for each data point is multiplied by this quantity to give a quantity proportional to the partial pressure of H_2. Finally, the ideal gas law is used to calculate a value proportional to the moles of H_2 in each sample, dn_{H2}, by knowing the lab temperature for each data point and the volume of the sample loop (2000 μL).

Thus, the moles of H_2 eluted in the ith gas headspace sample is:

$$n_{H2,i} = \alpha \frac{V_{loop}}{R} \frac{S_{2/36,baselined,i} \, P_{sys,i}}{T_{sys,i}} \quad (S10)$$

And the total moles of H_2 in a vial, related to the electrode titrated Li, is:

$$n_{H2,total} = \alpha \frac{V_{loop}}{R} \sum \frac{S_{2/36,baselined,i} \, P_{sys,i}}{T_{sys,i}} \quad (S11)$$

Where the α proportionality factor is determined to be 1.96 x 10^{-4} from the calibration curve in Supplementary Fig. S30. This approach is different than our previous works, where α is explicitly estimated with other mass spectrometer gas calibration methods that require mixing the analyte gas (here H_2) with Ar at known pressures (concentrations) in-line.

4. Voltage-based strategies for preventing battery degradation under diverse fast-charging conditions[3]

4.1. Motivation to address battery operating challenges for fast-charging

Lithium-ion batteries are central to the global energy transition, and fast-charging technology may have broad impacts for their utilization beyond obvious performance improvements. One example pertains to electric vehicle design. Vehicles are increasingly designed with large battery packs and long ranges (>300 km) to reduce the frequency of inconvenient charging. With widespread fast-charging, however, this trend could be reversed, leading to battery material conservation and more affordable vehicles that still satisfy the daily driving habits of most consumers.

On the individual battery cell level, the primary limitation for fast-charging is the poorly reversible lithium plating reaction that occurs instead of desired graphite intercalation. Understanding of the intertwined physical phenomena that can cause Li plating has progressed over decades[35,46,47,76,77]. While plating is frequently studied in the context of fast-charging of high-power cells (80% charge in <15 minutes), it is equally a concern for low-temperature charging[43], cell aging conditions[77,78], and moderate charging of high-energy cells[29,79].

Recent battery operating advances to enable fast-charging have focused on charge protocol development and control systems that prevent lithium plating by preventing the graphite potential from passing below the Li plating limit (0 V vs. Li/Li$^+$)[80,81]. Common strategies for charge protocol discovery include Doyle-Fuller-Newman (DFN) based electrochemical modeling[82], the use of three-electrode experiments[83–85], and data-driven methods[8,86]. For real-time battery controls, model predictive control (MPC) methods effectively apply constraints from the DFN model[87] to enhance charging performance and safety. The promise of the MPC approach has led to diverse efforts to reduce its high computational cost[88–93], typically via some combination of approximating the complex DFN model and simplifying the controls schemes with added elements such as reference governors[88,89,91].

A remaining challenge not reflected in many studies is that realistic battery charging conditions vary widely and depend on factors such as application, charging infrastructure, climate, energy availability and pricing, consumer needs, and pack configuration. Optimal charging protocols and temperature management vary across applications. Initial battery temperature will vary greatly by climate. Temperature rise during charge can be rapid at the cell level and increases with rate[94], energy density, and can exceed 20°C/min depending on the pack configuration and thermal management[95]. Novel shape memory alloy wires that facilitate rapid switching between battery insulation and cooling during fast charge[96] highlight system design factors. Additional challenges that emerge at the pack level include uneven cell aging[97] and temperature variability that can cause aging in colder cells linked to Li plating[98]. This diverse behavior might be captured with cell-level controllers, diagnostic testing, or temperature probes, but these add substantial computational or hardware cost.

In this work, we use electrochemical modeling and data visualization methods to explore simple voltage-based strategies to prevent fast-charging degradation over diverse conditions. First, we

---

[3] This chapter is in preparation for publication and is included herein with permission of co-authors.
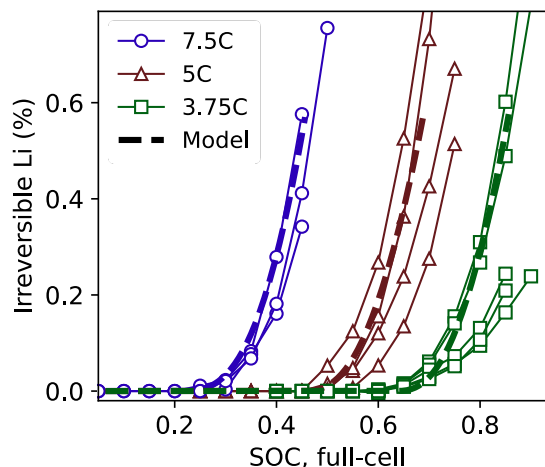
69

leverage recent experimental advances to quantify Li plating[99] to calibrate a high-fidelity electrochemical Li plating model and add modifications to reflect battery aging. Then we simulate fast charging while systematically changing operating or aging parameters, and quantify the relationship between measurable voltage characteristics and the plating onset response. Finally, we devise an algorithm for generating realistic, coupled current-temperature charging protocols, and use simulation results to propose empirical operating voltage constraints to safely avoid plating. Together, the findings reveal important connections between real-time voltage measurements and fast-charging ability that could reduce the negative impact of cell variability on performance.

Fig. 12. Calibrated model output for Li plating compared with Fig. 11 experimental data. The results are for Gr|NMC532 cells at T=30°C and constant current charge, where 1C = 2.8 mA/cm². Irreversible Li plating capacity is reported as a percentage of the graphite capacity, 3.35 mAh/cm². SOC is the charge capacity normalized to either: the total C/10 capacity between 3.0-4.2V (experiment) or the theoretical capacity calculated from the maximum NMC532 lithium fraction change (model), nominally the same value of 2.8 mAh/cm².

4.2. Model calibration to experimental lithium plating

This study employs a pseudo-2D (P2D) electrochemical-thermal model of a Graphite|LiNi$_{0.5}$Mn$_{0.3}$Co$_{0.2}$O$_2$ (NMC532) cell that has extensive experimental validation for fast charging and lithium plating. Early works[11,35] show strong model-experiment agreement for charging voltage profiles at varying electrode loadings (1.5 to 5.0 mAh/cm²), currents (1C to 9C), and temperatures (20 to 50°C)[11]. Experimental Li plating quantification in Li|Graphite half-cells was then used to estimate an exchange current density (i_0) for the lithium plating reaction[39] and refine the expression for lithium diffusion in graphite particles[99]. Finally, in this work, the P2D model was recalibrated to Li plating results of a 2.8 mAh/cm² cell from Fig. 11 by matching the material properties (Table S6) and doubling the graphite exchange current density pre-factor. This change increases the maximum i_0 from about 5 to 10 A/m² at standard Li concentrations and 30°C, well within literature ranges[100,101]. The model gives the expected lithium plating response to changes in rate (Fig. 12) and temperature (Fig. S46).

4.3. Li plating sensitivity to operating parameters and aging conditions

We then utilize the calibrated P2D model to quantify the impact of aging on fast-charging performance and lithium plating. This is in response to widespread recognition of the importance of cell aging on plating but a dearth of studies due to the difficulty of experimental data collection and model validation. Here we add simple and physical aging mechanisms to our model formulation, summarized in Table 3. The equation adjustments new to this work are shown in the supplementary information and complement past model documentation from Ref. 102. We approximate the worst values of each parameter under the assumption that cells with less than 80% of the initial capacity are not likely used for high-performance applications. Thus, we expect that up to 10-20% change in the values is possible for operational cells. The exception is the charge transfer kinetics parameters, which may change to a greater extent due to knowledge that reaction

Table 2. Aging mechanisms and values applied to Li plating model

Aging mechanism	Description	Value Range (Best − Worst)	Max. range expected within battery pack
Electrode expansion	The electrode thickness is increased and a void fraction is created, decreasing the volume fraction of other components (electrolyte, solids) and increasing the spacing between particles	$0-8$ µm, anode $0-8$ µm, cathode	4 µm 4 µm
Void formation or electrolyte depletion	A void fraction is subtracted from the electrolyte volume fraction (porosity) is decreased, also affecting tortuosity, while other component fractions remain unchanged	$0-0.05$, anode $0-0.05$, cathode	0.03 0.03
Loss of active material	The active material fraction of the total electrode solids is decreased, decreasing the electrode capacity and active reaction surface area	$0-10\%$, anode $0-20\%$, cathode	6% 15%
Charge transfer kinetics decrease	The exchange current density is multiplied by a coefficient (≤ 1), increasing the resistance to charge transfer	$1-0.5$, anode $1-0.5$, cathode	0.4 0.4
Lithium inventory loss, slippage	The anode lithiation at the start of charge is decreased relative to the expected value given the cathode lithiation	$0-0.08^*$, anode	0.05
Electrolyte conductivity decrease	The electrolyte conductivity is multiplied by a coefficient (≤ 1)	$1-0.8$, electrolyte	0.2

See Supplementary Information for model formulation of each mechanism. The initial electrode lengths are $\sim70\mu m$ and electrolyte volume fractions ~0.35. *For charges starting at low SOC, this value is constrained such that ($x \geq 0.01$ in Li_xC_6).

kinetics can change orders of magnitude with surface passivation. The final column in Table 3 estimates the largest cell-to-cell variability of each parameter at a given moment throughout the battery pack's lifetime and will be used for the analysis of Fig. 14.

Fig. 13 visualizes the effect of various operating and aging parameters on the charging voltage curve and Li plating onset for constant-current, constant-temperature charging. The x-axis for these plots is the normalized charge capacity delivered so all curves begin at x=0. Battery temperature and rate have outsize impact on the voltage and Li plating onset (Fig. 13a-b), as expected from many past works[11,35,39,99]. Plating is known to become more likely at higher states-of-charge (SOC) as the graphite approaches its full lithiation capacity, so it logically follows that increasing the initial state-of-charge (SOC) leads to plating at earlier charge capacities (Fig. 13c). Conversely, the loss of lithium inventory (LLI) in the graphite electrode lowers the initial lithiation relative to the expected value and more charge capacity can be safely delivered before plating (Fig. 13j, stars shift right from the baseline). LLI is the only aging mechanism that interestingly postpones the Li plating onset. The aging mechanism most drastically affecting plating is related to decreased electrolyte transport within the graphite via void formation or expansion (Fig. 13d-e), although these changes minimally affect the full-cell voltage. The voltage profiles are more affected by changes to the NMC electrode (Fig. 13f,l) due the sensitivity of its potential to lithiation state. Graphite intercalation kinetics worsening may also critically affect lithium plating if the exchange current value decreases greater than 50% (Fig. 13g).

4.4. Quantifying the correlation between voltage and Li plating onset

Next, we systematically quantify the relationship between voltage change and plating onset change from Fig. 13. The goal of this analysis is to understand whether voltage profile variability between cells, measured at the beginning of charge, can give accurate, cell-specific Li plating onset predictions later during the same charge. Fig. 14a illustrates the two metrics we use to quantify the difference between voltage curves: the average capacity difference between 3.95-4V (ΔQ_{4V}) and the average voltage difference between 2-5% capacity ($\Delta V_{2-5\%}$). These regions were selected because Li plating is not expected until well beyond 4V or 5% charge capacity for all conditions; lower voltage regions (< 3.95V) were not considered because some conditions start at high SOC

and thus high cell voltage (> 3.85V), and lower capacity regions (< 2%) were not selected because voltage differences are smaller in magnitude at the start of charge. Similarly, the change in plating onset voltage and capacity, which would be useful quantities to predict for battery control systems, is annotated in Fig. 14a. Fig. 14c-f plot the correlation between these voltage and plating onset metrics for the physical parameters labeled in Fig. 14b. Each data point is generated from a unique combination of 2 curves from a given panel of Fig. 13 where the parameter difference is below the maximum values provided in Table 3 or Fig. 14 caption. The maximum parameter difference constraint is applied because we seek to analyze small deviations in cell voltage within a nominally uniform pack at a single condition, not the voltage change spanning all possible battery conditions.

The first interesting conclusion drawn from this analysis is that Li plating prediction models should be designed to predict the onset SOC or capacity instead of the onset voltage. Fig. 14c-d show points scattered both above and below the y=0 line, indicating that for a given shift in the voltage profile (x-axis value), the plating onset voltage (y-axis value) could change in the positive or negative direction (Fig. 14d, red oval) depending on the underlying parameter change, making it difficult to predict. This means that additional knowledge of the specific aging mechanisms would
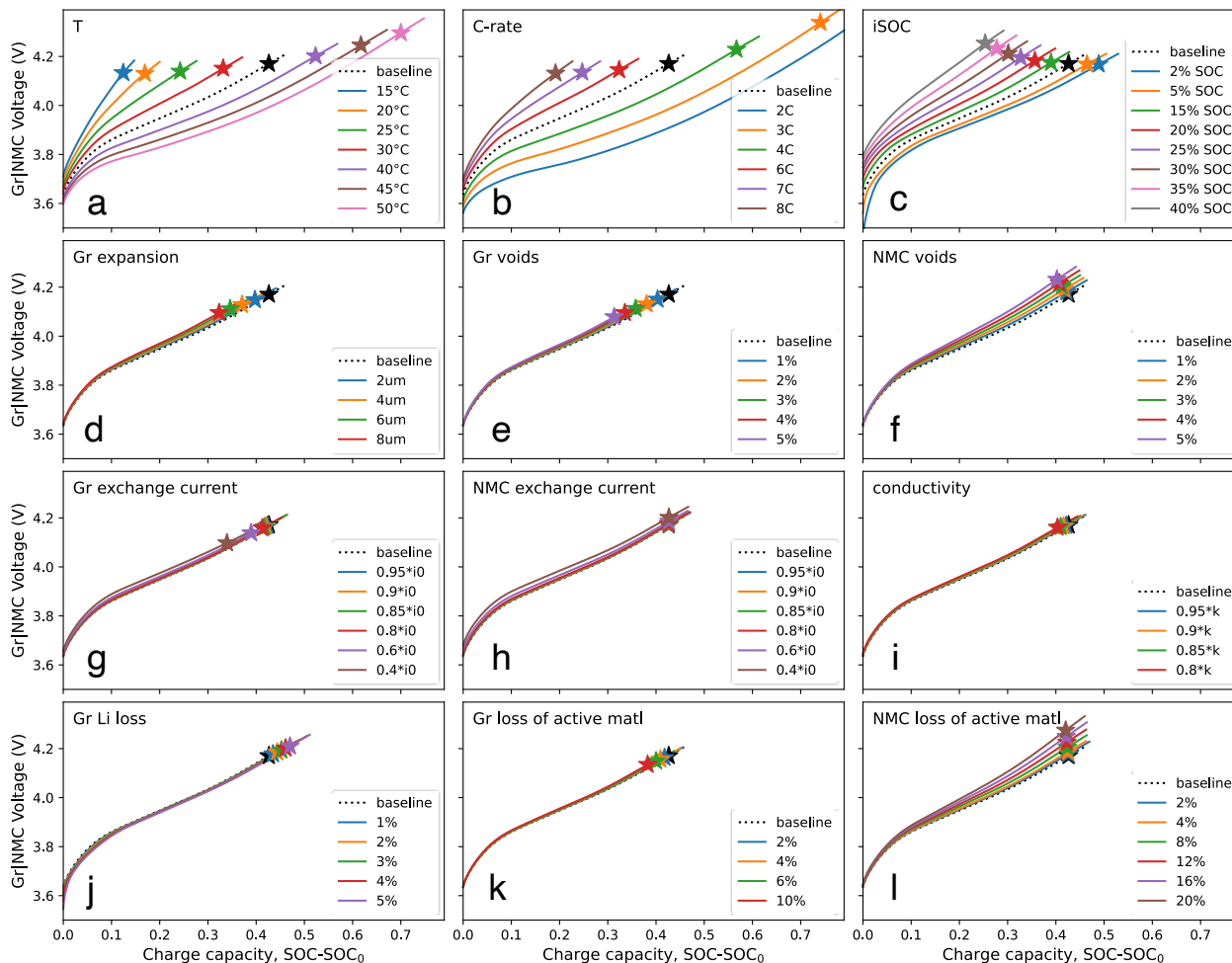
Fig. 13. Voltage and Li plating sensitivity to operating parameters and aging conditions. The baseline condition is constant-current charging at 5C, 35°C, 10% initial SOC, and no aging. Each panel shows the effect of a single parameter on the baseline voltage profile and Li plating onset (star). The Li plating onset is defined as the point where irreversible Li plating amount exceeds 0.01% of the graphite capacity (3.35 mAh/cm^2).
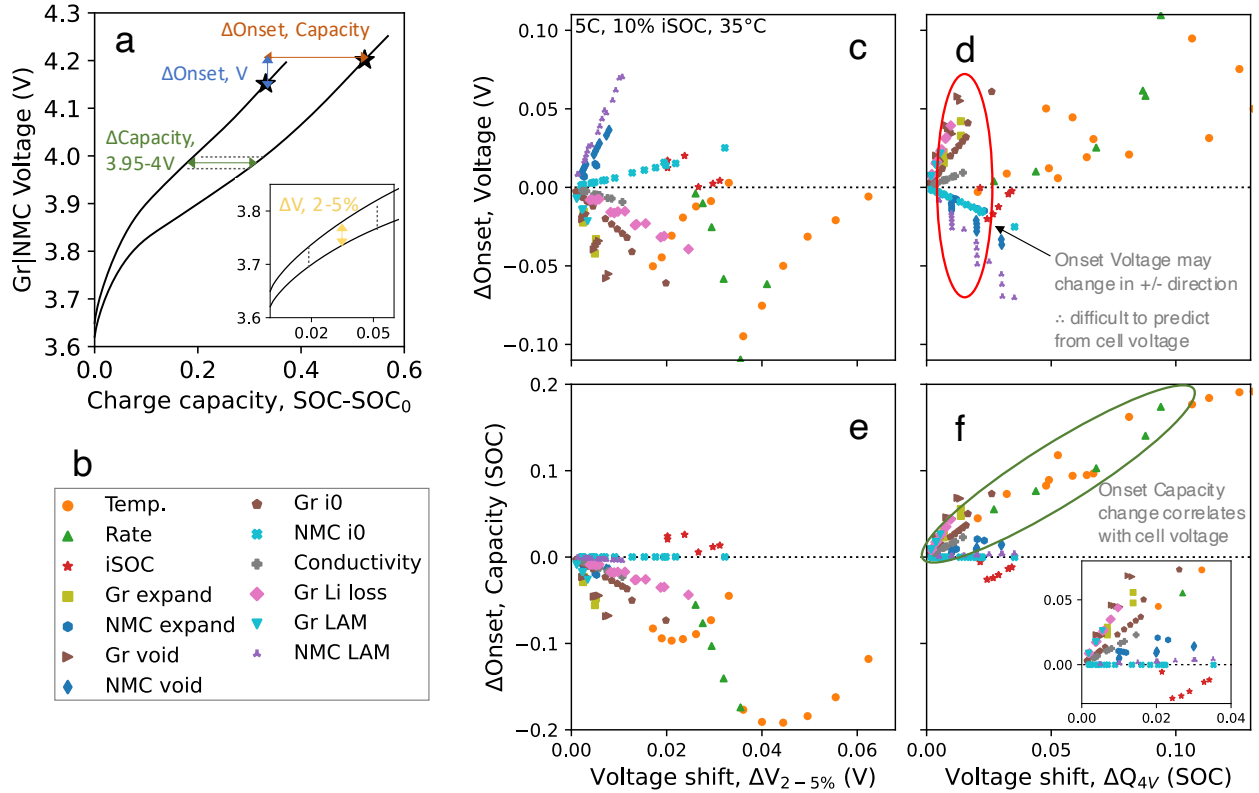
Fig. 14. Quantifying the correlation between voltage shift and Li plating onset change for the physical phenomena of Fig. 13. a, Two metrics are used to quantify the shift in voltage curve: the average voltage change between 2-5% charge capacity ($\Delta V_{2\text{-}5\%}$, yellow arrow) and the average capacity (SOC) change between 3.95-4.00V (green arrow). The plating onset change is quantified by the change in onset voltage or onset capacity, corresponding to the lengths of the respective arrows. **b,** Legend for data in panels c-f specifying which physical parameter causes the response. **c-f,** Each axis corresponds to one of the metrics in (a). Each data point is calculated from a unique combination of voltage curves from Fig. 13 that have the same parameter varied within the 'Maximum range expected within battery pack' of Table 2. The maximum variability for temperature, rate, and initial SOC (iSOC) are taken to be 10ºC, 1C, 5% respectively. It follows, then, that there are 13 temperature data points in each panel for the following simulation pairs [ºC-ºC] of Fig. 13: [15-20], [15-25] , [20-25], [20-30], [25-30], [25-35], [30-35], [30-40], [35-40], [35-45], [40-45], [40-50], [45-50].

be required to make an accurate onset voltage prediction. In contrast, data points for Fig. 14e-f that plot the change in onset capacity largely fall on the same side of the y=0 line. For Fig. 14e, this observation is readily interpretable. For a positive voltage shift corresponding to increased cell resistance due to lower temperature, for example, the plating onset capacity is shifted earlier, as indicated by the negative values. Most interestingly, the ΔQ_{4V} voltage metric correlates exceptionally well with the change in onset capacity regardless of underlying physical phenomena. These findings hold when the Fig. 13-Fig. 14 analysis is repeated at different baseline conditions of [4C, 25ºC, 20% SOC] and [7C, 45ºC, 5% SOC], shown in Fig. S47-48.

The sensitivity analysis workflow of Fig. 13-14 provides important insights towards battery management system (BMS) development and generally demonstrates the power of high-fidelity P2D models for battery systems. The ΔQ_{4V} metric may be a promising input for a voltage-based machine learning model that predicts the Li plating onset capacity. However, the data points from the NMC exchange current density variation (NMC i_0, blue x) lay along the y=0 line of Fig. 14f, indicating that this aging mechanism could cause a 'false-positive' event in which the voltage shifts but Li plating onset capacity is unchanged. Similarly, the initial SOC variation yields points below the y=0 line (red stars), contradicting the trend of the other parameters (green oval). These

observations highlight the importance of other BMS diagnostics, aging models, and SOC estimators to enhance a purely voltage-based model to enable safe high-performance fast charging.

4.5. Understanding patterns across diverse fast-charging protocols

We then wanted to understand Li plating behavior and fast-charging limitations over the vast current and temperature combinations that may be experienced by large format cells. There are recent reports of combined charging protocol and thermal management synergies[96,103], but the design space remains mostly unexplored because typically model users specify a current protocol and compute the heat generation for only a single thermal management condition. For single-layer cell P2D models like ours, this approach estimates unrealistically low battery self-heating (< 7°C at 7.5C rate). For 3D models that estimate multi-layer commercial cell temperature rise, there is increased computational complexity and uncertainty due to the difficulty of model calibration. Here, we instead impose time-dependent piecewise temperature and current functions on the P2D model, striving to simulate conditions realistic to commercial cells under diverse thermal management strategies. Table 4 shows parameters used to constrain the randomly generated fast-charging conditions to plausible SOC, currents, temperatures, and temperature ramps. Fig. 15a-b shows examples of the joint profiles, and the Supplementary Information details the careful design of the protocol generation algorithm.

The computed cell voltage and irreversible Li plating for four unique charging conditions is highlighted in Fig. 15c-d. Examples 1 and 3 show how irreversible Li plating typically increases exponentially with time (or State of Charge) under constant current charging conditions as in Fig. 12. Example 2, however, interestingly shows that Li plating may start and then subside in response to increasing temperature while at fixed current (Fig. 15a-c #2). Another effect of the notable temperature ramp is that the voltage is observed to decrease with increasing state of charge (Fig. 15d #2). Example 4 similarly shows that

Table 3. Parameters for generating realistic fast charging conditions

Variable	Value
Number of current steps	4
Stop SOC	0.95
Initial SOC [min,max]	[0.02, 0.5]
[Min, Max] rates by step	Max: [8, 7, 6, 5]C Min: [3, 3, 2, 2]C
[Min, Max] temperature ramp at I_{ref} = 8C	[5, 20] °C/min
[Min, Max] initial charging temperature	[10, 45] °C
[Min, Max] target temperature of charge	[30, 60] °C
Minimum difference between target and initial temperature	5 °C
Temperature drift factor max	0.2
Max rate increase for final current step	0.5 C
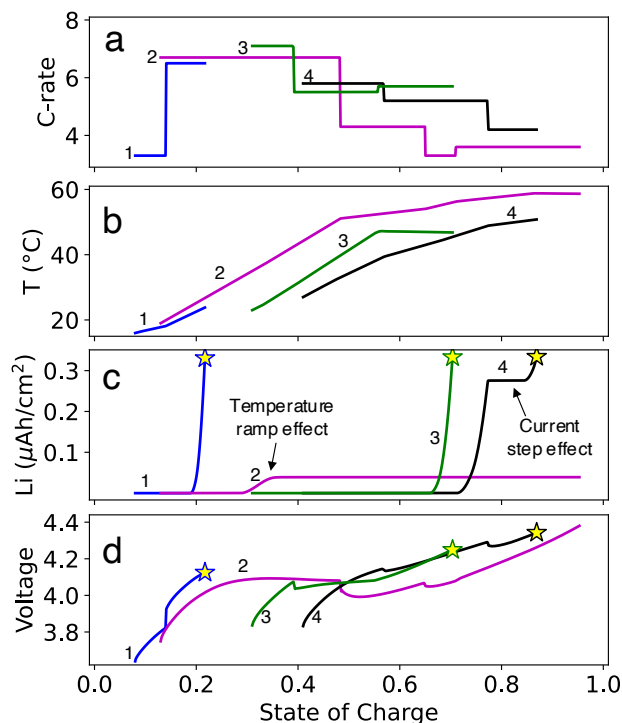
Fig. 15. Visualizing model Li plating and voltage output for example fast charging simulations. a, Normalized current (1C = 2.8 mA/cm²) and **b,** Temperature profiles applied to the fast charging model, with **c,** simulated total irreversible Li plating and **d,** simulated Gr|NMC cell voltage. Data are displayed either until the Li plating onset condition is met (curves 1,3,4), denoted by the stars, or until the cell voltage reaches 4.40V (curve 2). Each fast charging protocol generated with Table 3 parameters has 4 current steps, but in practice fewer are often observed due to simulation stop conditions. The color-coded examples are labeled with numbers 1-4 for clarity, establishing connection between panels a-d.

74

irreversible Li plating can be abruptly stopped in response to a current decrease (Fig. 15a,c #4). The stars denote the point at which irreversible Li plating exceeds the threshold we define as the plating onset.

Of the 1000 fast-charging conditions attempted, 600 induced notable Li plating, summarized in Fig. 16a-d. The visualization confirms that Li plating was studied over a comprehensive range of currents, temperatures, and SOC. Fig. 16e plots the plating onsets, which are the end points of the voltage curves in Fig. 16d. The plating onsets are tightly clustered despite the wide range of experimental conditions. It is expected that the plating onset voltages generally increase with increasing SOC, following the cell open-circuit voltage dependence on SOC. The red oval highlights two points that are separate from the clustering, and the corresponding voltage profiles in Fig. 16d indicate that the current was abruptly increased prior to the start of Li plating, explaining the jump in the cell voltage.

An exciting empirical result from this meta-analysis is that there is a minimum voltage below which plating does not occur, dependent on current SOC (Fig. 16e, blue curve). This boundary curve could inform when to conservatively stop fast-charging or, better, when to calculate the next optimal step in a charge sequence. Fig. 16f illustrates, however, that voltage curves crossing the boundary at the same SOC can have variable plating onsets. To quantify the conservatism of the universal boundary curve approach, we first plot the charge capacity remaining after the boundary
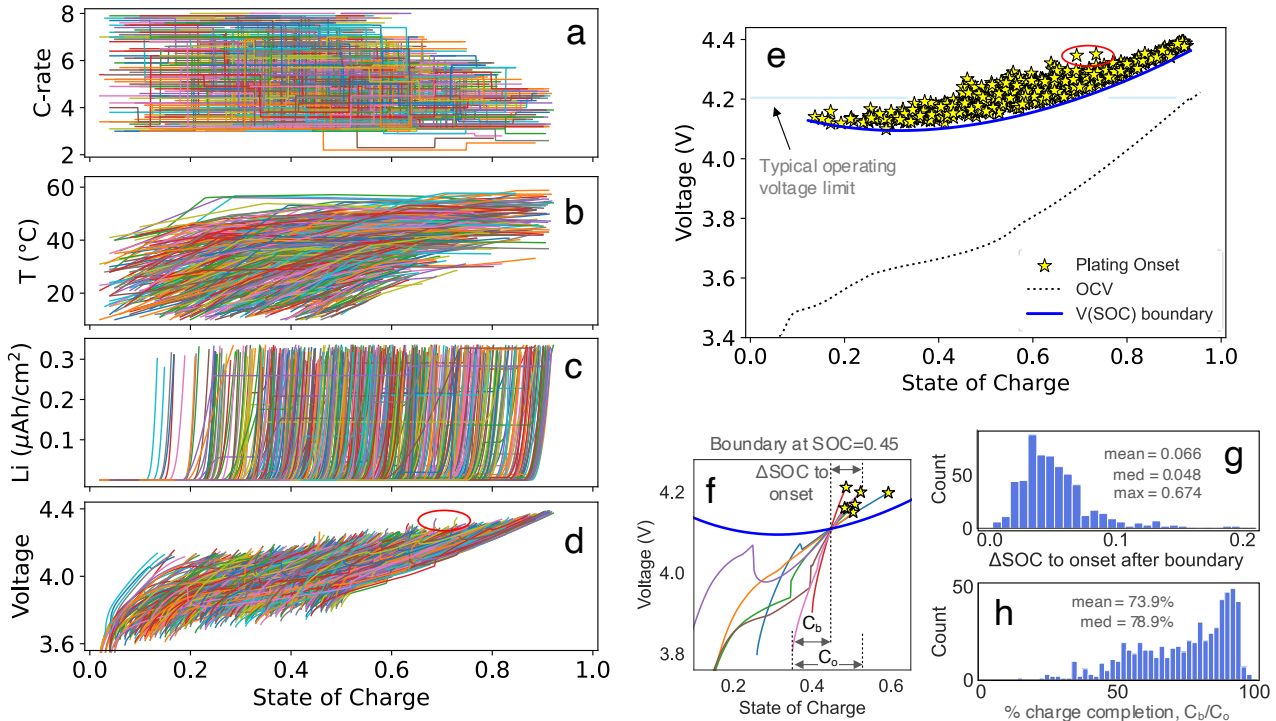
Fig. 16. Meta-analysis of Li plating onset conditions for diverse fast charging protocols. a-b, Model inputs, and **c-d,** model outputs for n=600 simulations, as in Fig. 15, that induce irreversible Li plating above the onset threshold. **e,** Plating onsets for all simulations, which correspond to the charging voltage curve endpoints in (d). The boundary is an empirical curve sketched along the lowest stars in the cluster, indicating a possible operating voltage constraint to avoid plating. The red ovals in (d) and (e) emphasize the connection between the plots. **f,** Shows charging curves from (d) that intersect the plating boundary at 0.45 ± 0.003 SOC. **g,** Distribution of the capacity remaining after the boundary, before the plating onset (ΔSOC to onset). This equals ($C_o - C_b$), the onset capacity minus the boundary capacity. **h,** Distribution of the percent charge completion attained by the time the voltage hits the boundary, where full completion (100%) means the charge stops exactly at the plating onset. This equals C_b/C_o from (f).

75

until the onset of plating (ΔSOC to onset, Fig. 16f-g). This shows that the plating onset typically occurs within 0.05 SOC after reaching the boundary. Next, we quantify the fractional charge completion achieved up to the boundary relative to the total charge capacity before Li plating (C_b/C_o, Fig. 16f,h). This highlights that, on average, about 75% of the maximum safe charge capacity is attained. Overall, This very simple battery operating constraint could prove useful and complementary to other controls methods, including those that map safe current rates as a function of the operating voltage[91], SOC[93], or estimated graphite critical surface concentration[92] using reduced-order electrochemical models.

4.6. Plating onset voltage boundary variation with aging

In culmination, we add the aging effects (Table 3) to the diverse fast-charging conditions (Table 4) to understand how the plating voltage boundary may vary with age. To simulate a variety of possible aging impacts without presupposing specific aging mechanisms, parameter values are drawn from health-dependent distributions (Fig. 17a). We represent the extent of degradation to each aging parameter as a health index, which ranges from 1 at beginning-of-life to 0.8 at end-of-life. This is analogous to state-of-health, but we refrain from using the term because it is often synonymous with remaining battery capacity. For example, minimally aged cells with health index of 0.98 draw aging parameters that are only slightly worse than their initial values with relatively tight distribution; parameters for extensively aged cells, in contrast, may be much worse than their initial values and vary substantially across draws, reflecting the increasing variability of cell
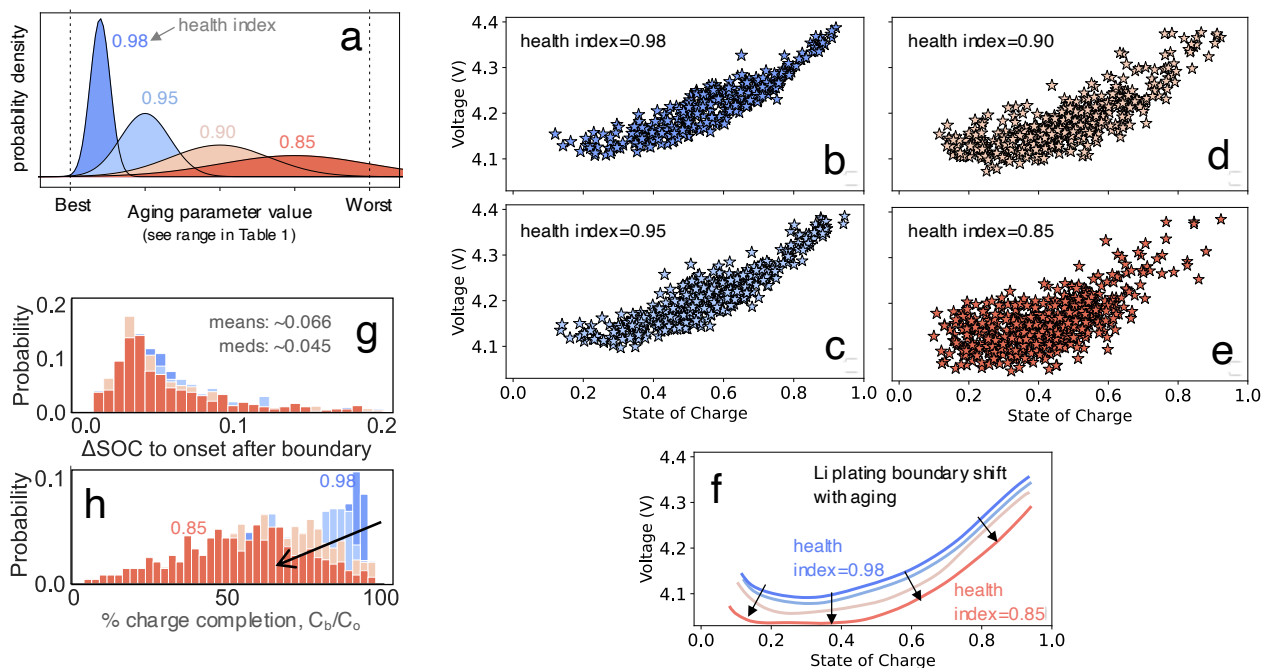
Fig. 17. The effect of aging on Li plating onsets and operating voltage boundaries. a, The distributions from which aging parameters were selected for battery pack health indices ranging 0.98→0.85, where health index=1 means the Best value and health index=0.8 means the Worst value of Table 2. For a simulation at a specified health, each parameter is drawn independently from the specified distribution, resulting in moderate correlation of aging parameters based on the health, with larger variability for lower-health packs. **b-e,** Li plating onsets for multistep fast charging protocols with correlated aging. 500 conditions were tested for each health index, and the number of simulations inducing Li plating were n=330, n=408, n=443, and n=484 (plotted) for health indices 0.98→0.85 respectively. **f,** Sketch of how the operating voltage boundary approach of Fig. 16 may vary with aging, based on the data in (b-e). **g-h,** Overlaid distributions of (g) the capacity remaining after the boundary, before the plating onset (ΔSOC to onset) and (h) the percent charge completion attained by the time the voltage hits the boundary, for each health index using the curves in (f).

76

performance with aging due to variability of cell failure mechanisms, operating heterogeneity, and manufacturing defects.

Fig. 17b-e shows Li plating onsets from 500 simulations at health indices of 0.98, 0.95, 0.9, and 0.85, which can be be compared to the beginning-of-life results in Fig. 16e. Unsurprisingly, the Li plating onset becomes more variable for the lower health indices due to increased aging parameter variability, making it necessary to adjust the voltage plating boundary strategy in accordance to cell health. This result is also a useful demonstration of why Li plating can occur unexpectedly in aged cells despite using voltage cutoffs that are well below Li plating thresholds at beginning-of-life. In Fig. 17f, we overlay the plating voltage boundaries required to maintain safe charging at each health index. Because the variable-health boundaries are adjusted to the worst-performing cells, it is expected that the voltage boundary approach becomes more conservative with aging. Interestingly, Fig. 17g shows that the plating onset still typically occurs about 0.05 SOC after the boundary regardless of the health index, as in the beginning-of-life cells (Fig. 16g). The mean percent charge acceptance up to the boundary, in contrast, declines notably from 75% to 55% as the health index is lowered from 0.98 to 0.85 (Fig. 17h).

4.7. Conclusions and outlook

This work importantly shows that cell voltage differences correlate with differences in plating onset SOC and that a lower voltage boundary may prevent Li plating across variable operating conditions. There are many opportunities to expand upon the demonstrated approach and findings. Validated P2D models could be further applied to develop optimal charge protocols, such as where the graphite potential is fixed at the Li plating limit, at diverse imposed temperatures and SOC. Similar workflow may be used for cathode materials such as lithium iron phosphate (LFP) that have unique voltage profiles and may differently affect fast charge capability[104]. In particular, the flat voltage profile of LFP or other phase-transformation positive electrode materials may cause the voltage-boundary approach demonstrated here to be excessively conservative. 3D modeling will be necessary to consider effects of heterogeneous aging or temperature distribution in large-format cells; 18650 cell internal temperature gradients may be minimal (< 5ºC) without active thermal management[105], the scenario where our results are most transferrable, but can reach 20ºC difference with pulse charging and external cooling[106]. Finally, experimental cell aging studies can be combined with in-situ Li plating quantification[99] to further refine this approach and elucidate modifications needed for real-world application.

4.8. Methods and model formulation

COMSOL Simulations. The pseudo-2D model based on the Doyle-Fuller-Newman framework was simulated with COMSOL software using the Lithium-ion Battery module. Model parameter values and equations have been extensively justified in previous works[11,35,39,99,102], some of which are reproduced below. Here we highlight important notes or differences from past studies. First, for Fig. 12 simulations performed to compare with past experiments, the initial temperature was specified to be 30 ºC but the simulation is not isothermal. The computed temperature rise based on previously validated thermal properties was 2.4, 3.9, and 6.5 ºC for the rates of 3.75C, 5C, and 7.5C respectively. For all other simulations, the temperatures were user-defined; the Fig. 13 sensitivity analysis was performed isothermally and the multi-step protocols used piecewise temperature functions. In COMSOL, the user-defined temperature was achieved with a Heat Flux component within the Heat Transfer in Solids module. At both electrode current collectors, the convective heat flux was applied as

$$q_0 = h \cdot (T_{ext} - T)$$

where T_{ext} is the external temperature defined by the piecewise function, T is the cell temperature at the boundary, and h is the convection heat transfer coefficient. To force the cell temperature to rapidly approach T_{ext}, h is multiplied by 10^3 to give 6000 W/m^2·K.

For the piecewise functions used for the multistep protocol, the current inputs are four C-rate values corresponding to the unique time steps. The SOC interval corresponding to each current step is split into 2 for a total of 8 temperature steps. The temperature piecewise function is defined by 8 step end-time parameters (s), 8 start-temperature values (ºC), and 8 temperature ramp values (ºC/s). Writing the piecewise function in terms of model-defined parameters enabled use of the Parametric Study option to systematically vary those parameters and quickly simulate thousands of different conditions. Simulation stop criteria were added to prevent simulations from exceeding 4.4V or 0.1% irreversible Li plating, the regions of interest for this study. Data analysis and visualization was performed in Python using a combination of the Pandas, SciPy, Seaborn, and matplotlib libraries.

 Charge protocol generation algorithm. In this description, variables are selected randomly from a uniform (flat) distribution unless specified. **1) Random starting variable selection.** Random current values are selected for steps 1-3 between the [Min, Max] values provided in Table 4, then the current for step 4 is randomly selected such that it cannot be 0.5C larger than step 3. This constraint was added because it is unrealistic for a large current increase near the end of charge. An initial SOC is randomly selected, and then the ΔSOC for each of the 8 temperature steps are randomly generated so that the proposed charge would reach the target Stop SOC of 0.95. The initial charging temperature is randomly selected and then the charging target temperature, which must be at least 5 ºC higher than initial, is selected. This constraint maintains that batteries will heat some, naturally occurring and desirable for avoiding Li plating, during fast charge. **2) Calculate the first step of the piecewise temperature function.** Based on the initial rate and temperature, a semi-random initial temperature ramp is selected. The initial temperature is normalized between 0 and 1 according to the minimum and maximum initial values. A random value x is drawn from the normal distribution with μ=(1-T$_{i,norm}$) and σ=0.4 is selected and

constrained to $0 < x < 1$. Then this value is scaled according to the minimum (0) and maximum (1) temperature ramp rates (m) expected for the given rate I, with ramp rates given by:

$$m_{min}(°C/s) = \frac{I^2}{I_{ref}^2} \, m_{ref,min}$$

$$m_{max}(°C/s) = \frac{I^2}{I_{ref}^2} \, m_{ref,max}$$

This was done to incorporate the logic that for lower initial temperatures, higher temperature ramps are likely desired to achieve high-temperature conditions most suitable for fast-charging. This also captures the idea that temperature ramp values should be higher for higher C-rates, roughly scaling with an I^2 dependence derived from joule heating (I^2R) of an electrical conductor. **3) Calculate remaining steps of the piecewise temperature function.** For each remaining step, ramp rates are calculated according to the historical temperature. If the target temperature has been exceeded, then the temperature ramp will fluctuate randomly within a range of values, positive or negative, to capture uneven heating or cooling effects. The temperature drift factor of Table 4, 0.2, is multiplied by the m_{max} to constrain the fluctuation ramp values, which vary with C-rate. If the target temperature has not been reached, then either i) If the C-rate of the next step is the same, then the temperature ramp is kept approximately the same with some added noise to account for real-life variability or curvature, or ii) If the C-rate of the next step is different than the previous, a new semi-random temperature ramp is selected according to the present temperature and rate according to the function from Section (2). Finally, for all cases, if the proposed temperature ramp for a given step causes the temperature to greatly exceed the target temperature (which might occur if the random ΔSOC for a step is very large), then the ramp is adjusted with knowledge of the future target.

Electrode expansion, void formation, and loss of active material. The length of the electrode, l ,is increased from its beginning-of-life (BOL) length, l_{BOL}, by $\boldsymbol{l_{expansion}}$. The BOL length is used to calculate electrode capacity from the volume of active material, so other battery operating parameters remain unaffected when expansion is added to the model. The nominal battery properties without added aging have the subscript BOL. The same formulation is used for both electrodes, graphite and NMC532.

$$l = l_{BOL} + \boldsymbol{l_{expansion}}$$

When the electrode thickness is increased, a void fraction is created, and the effect is a decreasing volume fraction of other components (solids, electrolyte, pre-existing voids). This material conservation is captured by multiplying each component fraction by the following expansion factor, which is always ≤ 1 because we only consider positive values for $\boldsymbol{l_{expansion}}$:

$$\left(\frac{l_{BOL}}{l}\right)$$

The equations below relate the solids volume fraction, ε_{solids}, to the BOL value according to the above factor:

$$\varepsilon_{solids,BOL} = 1 - \varepsilon_{elyte,BOL}$$

$$\varepsilon_{solids} = \varepsilon_{solids,BOL} \left(\frac{l_{BOL}}{l}\right)$$

A similar correction is made for the electrolyte fraction ε_{elyte}. Note that the electrolyte fraction can also be affected by direct void formation, a separate mechanism to simulate electrolyte drying or gas formation within electrode pores. We assume this void volume fraction, $\varepsilon_{void,elyte,BOL}$, is present at BOL, prior to electrode expansion, for simplicity:

$$\varepsilon_{elyte} = (\varepsilon_{elyte,BOL} - \boldsymbol{\varepsilon_{void,elyte,BOL}}) \left(\frac{l_{BOL}}{l}\right)$$

The fractional loss of active material, %**LAM**, another aging mechanism, is added to the equation below where ε_{AM} is the volume fraction of active material and CBD_AM is the volume fraction of solids that are non-active carbon binder material:

$$\varepsilon_{AM,anode} = \varepsilon_{solids,anode}(1 - CBD\_AM)(1 - \%\boldsymbol{LAM})$$

Finally, to ensure consistency of the formulation, we confirm in the model that the sum of all volume fractions (electrolyte, active material, carbon binder material, inactive material, expansion-induced voids, electrolyte loss voids – in order, below) equals to 1, regardless of the aging parameter values:

$$\varepsilon_{elyte} + \varepsilon_{AM} + \varepsilon_{AM}\left(\frac{CBD\_AM}{1-CBD\_AM}\right) + \varepsilon_{AM}\left(\frac{\%LAM}{1-\%LAM}\right) + \frac{l_{expansion}}{l} + \varepsilon_{void,elyte,BOL}\left(\frac{l_{BOL}}{l}\right) = 1$$

Charge transfer kinetics decrease and electrolyte conductivity decrease. The exchange current density i_0 [A m^{-2}] for either graphite intercalation or NMC532 de-insertion, the reactions that dominate during battery charge, is multiplied by a coefficient A (≤ 1), increasing the resistance to charge transfer. This coefficient does not affect the dependence of i_0 on solid Li concentration c_s, electrolyte Li$^+$ concentration c_e, or temperature T. Similarly, the electrolyte conductivity κ_e is multiplied by a coefficient B (≤ 1).

$$i_{0,\text{aging}} = A \cdot i_0(c_s, c_e, T)$$

$$\kappa_{e,\text{aging}} = B \cdot \kappa_e(c_e, T)$$

Lithium inventory loss, electrode slippage. The initial lithium intercalation fraction in the graphite electrode $x_{Gr,i}$ is determined by the initial state-of-charge (SOC_i) and is calculated using the minimum lithium fraction in the graphite $x_{Gr,min}$, the capacities of both electrodes, C_{Gr} and C_{NMC}, and the maximum graphite intercalation fraction change $\Delta x_{max,Gr}$. The loss of lithium inventory $x_{Li,loss}$, is subtracted from $x_{Gr,i}$:

$$x_{Gr,i} = x_{Gr,min} + SOC_i \cdot \Delta x_{max,Gr} \frac{C_{NMC}}{C_{Gr}} - x_{Li,loss}$$

The electrode capacities are calculated from their respective theoretical volumetric lithium concentrations multiplied by the maximum expected intercalation fraction changes Δx. The initial lithium fraction in the NMC electrode $x_{NMC,i}$ is:

$$x_{NMC,i} = x_{NMC,max} - SOC_i \cdot \Delta x_{max,NMC}$$

The change in $x_{Gr,i}$ shifts the graphite potential range accessed during charge, which is why electrode slippage is used to alternately name this effect. We only consider one direction of slippage resulting from irreversible reactions at the graphite electrode, such as Li plating or SEI formation, but believe future work could consider scenarios where the initial graphite lithiation is higher than expected $(x_{Li,loss} < 0)$.

Lithium plating and stripping reaction formulation. The Li plating and stripping reaction j_{Li} is expressed in the Butler-Volmer formulation as

$$j_{Li} = \frac{i_0}{F}\left[exp\left(\frac{(1-\alpha)F(\Phi_s - \Phi_e - U_{OCP})}{RT}\right) - exp\left(\frac{-\alpha F(\Phi_s - \Phi_e - U_{OCP})}{RT}\right)\right],$$

where i_0 is exchange current density, α is the transfer coefficient for plating, U_{OCP} is the open-circuit potential of the plating reaction (0 vs. Li/Li$^+$), F is Faraday's constant, R is the universal gas constant, and T is the temperature.

In COMSOL, the lithium plating and stripping equations are implemented by adding a Distributed ODE to the graphite electrode domain with conditional statements. If the local voltage, $(\Phi_s - \Phi_e)$, is less than 0 V vs. Li/Li$^+$, then the lithium plating reaction occurs $(j_{Li} < 0)$, forming both reversible and irreversible lithium plating:

$$\frac{\partial n_{Li,irrev.}}{\partial t} = -(1-\beta)\,j_{Li}\,A_s$$

$$\frac{\partial n_{Li,rev.}}{\partial t} = -\beta\,j_{Li}\,A_s$$

where $n_{Li,irrev.}$ and $n_{Li,rev.}$ are the concentrations (mol/m^3) of irreversible and reversible lithium plating respectively, A_s is the anode specific surface area with units 1/m, and β is the plating reversibility factor.

If $(\Phi_s - \Phi_e) > 0$, then no plating will occur and:

$$\frac{\partial n_{Li,irrev.}}{\partial t} = 0$$

If $(\Phi_s - \Phi_e) > 0$ and $n_{Li,rev.} > 0$, then Li stripping ($j_{Li} > 0$) will occur and reversible lithium plating will decrease according to:

$$\frac{\partial n_{Li,rev.}}{\partial t} = -\beta\, j_{Li}\, A_s \frac{n_{Li,rev.}}{n_{Li,rev.} + \gamma}$$

where the term containing γ is added to decrease the stripping amount as $n_{Li,rev.}$ approaches 0.

Finally, if $(\Phi_s - \Phi_e) > 0$ and $n_{Li,rev.} \leq 0$, then Li stripping will not occur and:

$$\frac{\partial n_{Li,rev.}}{\partial t} = 0$$

The parameter values used for the Li plating formulation are: $i_0 = 10$ A/m^2, $\alpha = 0.7$, $U_{OCP} = 0$ V, $\beta = 0.8$, and $\gamma = 0.01$.

Table S6. Constant-value model parameters

Variable	Description	Value	Unit
A	Current-collector area	1.54	cm^2
C_{NMC}	Full-cell capacity (Measured & used for C-rates)	2.80	mAh cm^{-2}
C_{Gr}	Anode theoretical capacity (set to match expt.)	3.35	mAh cm^{-2}
$c_{e,0}$	Initial electrolyte concentration	1.2	kmol m^{-3}
$c_{s,max,an}$	Maximum Li concentration in the anode	30.0	kmol m^{-3}
$c_{s,max,an}$	Maximum Li concentration in the cathode	49.6	kmol m^{-3}
$\Delta x_{max,Gr}$	Maximum intercalation fraction change, graphite anode	0.97	-
$x_{Gr,min}$	Minimum graphite anode intercalation fraction	0.02	-
$\Delta x_{max,NMC}$	Maximum intercalation fraction change, NMC cathode	0.58	-
$x_{NMC,max}$	Maximum NMC cathode intercalation fraction	0.89	-
N/P	Anode capacity vs. cathode capacity	1.16	-
t_{an}	Length/thickness of anode	70	µm
t_{sep}	Length/thickness of separator	25	µm
t_{ca}	Length/thickness of cathode	71	µm
$p_{e,an}$	Bruggeman coefficient of electrolyte in anode	2	-
$p_{e,sep}$	Bruggeman coefficient of electrolyte in separator	1.8	-
$p_{e,ca}$	Bruggeman coefficient of electrolyte in cathode	2	-
$p_{s,an}$	Bruggeman coefficient of solid phase in anode	2	-
$p_{s,ca}$	Bruggeman coefficient of solid phase in cathode	2	-
$R_{s,an}$	Average particle radius in anode	4	µm
$R_{s,ca}$	Average particle radius in cathode	1.8	µm
α	Reaction transfer coefficient, all intercalation reactions	0.5	-
$\epsilon_{el,an}$	Electrolyte volume fraction in anode	0.34	-
$\epsilon_{el,ca}$	Electrolyte volume fraction in cathode	0.354	-
$\epsilon_{el,sep}$	Electrolyte volume fraction in separator	0.55	-
$\epsilon_{s,an}$	Solid-phase active material volume fraction in anode	0.60	-
$\epsilon_{s,ca}$	Solid-phase active material volume fraction in cathode	0.51	-
$\sigma_{s,an}$	Effective solid-phase conductivity in the anode	2.6	S m^{-1}
$\sigma_{s,ca}$	Effective solid-phase conductivity in the cathode	2.7	S m^{-1}
$i_{0,Li}$	Exchange current density for Li plating/stripping	10	A m^{-2}
α_{Li}	Transfer coefficient of Li plating reaction	0.7	-
β	Li plating reversibility factor	0.8	-
γ	Trick for oxidation of reversible Li plating	0.01	-

Summary of physics-based model governing equations, based on the original Doyle-Fuller-Newman framework. *Reproduced with author permission from the supplementary information of Ref [102], parameters are modified to reflect the present work.*

The pseudo-2D model simulates 1) liquid-phase Li-ion concentration, 2) liquid-phase potential, 3) solid-phase potential, and 4) solid-phase Li concentration. The "primary direction" is the direction normal to the anode current-collector, the "secondary direction" is the particle-level radial coordinate resolved within both electrodes. In the primary direction, the anode current collector location is denoted as "$-$", the anode/separator interface is denoted as "$-s$", the separator/cathode interface is denoted as "s+", and the cathode current collector location is denoted as "+". The primary-direction equations govern the solid-phase potential Φ_s, liquid-phase potential Φ_e, and liquid-phase concentration c_e dynamics. The liquid-phase states (Φ_e and c_e) are solved across the entire domain from $-$ to +. The solid-phase potential Φ_s is only solved in the electrode domains ($-$ to $-s$ and s+ to +). The "minus" domain is referred to as the anode. The "plus" domain is referred to as the cathode. Between these two electrode domains ($-s$ to s+) is referred to as the separator. It is important to note that while the governing equations are similar or the same between domains, the properties are *different*. For example, the Bruggeman coefficient p is used in all domains, but the Bruggeman is different in the anode domain, as compared to the separator domain, as compared to the cathode domain. As a rule-of-thumb, assume that all parameters are domain-dependent unless otherwise stated. The reader is directed to influential work by Newman and coworkers for governing equations derivations[25,66–69].

Liquid-phase concentration, c_e. The governing equation for the liquid-phase potential is solved in the primary x-direction across the entire domain (i.e., $-$ to + face). The governing equation can be expressed compactly as

$$\frac{\partial(\varepsilon_e c_e)}{\partial t} = \nabla_x \cdot \left(D_e \varepsilon_e^{p_e} \nabla_x c_e - \mathbf{i}_e \frac{t_+^0}{F} \right) + \frac{3\varepsilon_s}{R_s} j,$$

where ε_e is the domain-specific electrolyte volume fraction, c_e is the concentration in the electrolyte, t is time, D_e is the domain-independent electrolyte diffusion coefficient, p_e is the domain-specific electrolyte Bruggeman coefficient, t_0^+ is the domain-independent transport number, F is Faraday's constant, R_s is the domain-specific particle radius, and j is the charge-transfer production rate. Note that the ∇_x symbols have a subscript x. This means that these gradients and divergences are taken in the primary x-direction. The electrolyte current density $\mathbf{i}_e$ is expressed as

$$\mathbf{i}_e = -\kappa_e \varepsilon_e^{p_e} \nabla_x \Phi_e + 2\frac{\kappa_e \varepsilon_e^{p_e} RT}{F}\left(1 + \frac{\partial \ln f_\pm}{\partial c_e}\right)(1 - t_+^0)\nabla_x \ln c_e,$$

where R is the universal gas constant, T is the temperature, κ_e is the domain-independent electrolyte conductivity, and $(\partial \ln f_\pm / \partial c_e)$ is the domain-independent thermodynamic factor. The charge-transfer production of Li j is domain-dependent. In the separator ($-s$ to s+) j=0. In either the anode or the cathode, j is expressed in the Butler--Volmer formulation as

$$j = \frac{i_0}{F}\left[\exp\left(\frac{(1-\alpha)F(\Phi_s - \Phi_e - U_{OCP})}{RT}\right) - \exp\left(\frac{-\alpha F(\Phi_s - \Phi_e - U_{OCP})}{RT}\right)\right],$$

where i_0 is the domain-specific exchange current density, α is the transference number, and U_{OCP} is the domain-specific open-circuit potential. The liquid-phase concentration c_e has no-flux boundary conditions at the $-$ and + faces. This is expressed mathematically as

$$\mathbf{n} \cdot \nabla_x c_e|_{-,t} = 0, \quad \text{and} \quad \mathbf{n} \cdot \nabla_x c_e|_{+,t} = 0,$$

where $\mathbf{n}$ is the surface normal. The initial conditions are assumed to be uniform across all domains,

$c_e(x)|_{t=0} = c_{e,0}$.

   Liquid-phase potential, Φ_e. The liquid-phase potential is solved across the entire domain. Notably, the liquid-phase potential is commonly referred to as a "constraint equation'" because it does not have a time derivative. The liquid-phase potential governing equation can be expressed as

$$\nabla_x \cdot \mathbf{i}_e = \frac{3\varepsilon_s}{R_s} j F.$$

The boundary conditions for the liquid-phase potential are defined at the $-$ and $+$ face. At these boundaries, the current is set to zero. Mathematically, this can be stated as

$$\mathbf{n} \cdot \mathbf{i}_e|_{-,t} = 0, \quad \text{and} \quad \mathbf{n} \cdot \mathbf{i}_e|_{+,t} = 0.$$

Depending on the solver, this constraint equation may or may not need an initial condition. If an initial condition is required, the potential can be assumed to be uniform across the domain and be near

$$\Phi_e(x)|_{t=0} \approx - U_{OCP,an}\left(\frac{c_{s,0}}{c_{s,max}}\right),$$

where $c_{s,0}$ is the initial solid-phase concentration in the anode domain, and $U_{OCP,an}$ is the open-circuit potential function in the anode domain.

   Solid-phase potential, Φ_s. The solid-phase potential is solved in the primary direction in the anode and cathode domains. It is not resolved in the separator. The solid-phase potential dynamics can be expressed as

$$\nabla_x \cdot (-\sigma_s (1 - \epsilon_{el})^{p_s} \nabla_x \Phi_s) = \frac{-3\varepsilon_s}{R_s} j F,$$

where σ_s is the domain-specific solid-phase conductivity, ε_s is the domain-specific solid-phase volume fraction, and p_s is the domain-specific solid-phase Bruggeman coefficient. The solid-phase potential requires boundary conditions at either end of the domain ($-$ and $+$), and at the interior boundaries ($-s$ and $s+$). At the $-$ boundary, the potential is set to zero

$$\Phi_s|_- = 0.$$

At the separator boundaries, $-s$ and $s+$ the flux is zero

$$\mathbf{n} \cdot \nabla_x \Phi_e|_{-s,t} = 0, \quad \text{and} \quad \mathbf{n} \cdot \nabla_x \Phi_e|_{s+,t} = 0.$$

At the $+$ face, either the flux can be set (constant-current mode), or the potential can be specified (constant-voltage mode). Constant-current mode can be expressed as

$$\mathbf{n} \cdot (-\sigma_s (1 - \epsilon_{el})^{p_s} \nabla_x \Phi_s)|_+ = -\frac{I}{A},$$

where I is the current demanded (in Amps) and A is the current-collector geometric area. Constant-voltage mode is represented as

$$\Phi_s|_+ = U_{CV},$$

where U_{CV} is the specified constant-voltage constraint. The solid-phase potential Φ_s initial conditions are domain-specific and are not necessarily required for this algebraic constraint equation. If required, in the anode, the potential is approximately the same value as the boundary condition at the $-$ face

$$\Phi_s|_{x \in [-,-s], t=0} \approx 0.$$

In the cathode, the potential is approximately related to the battery-level open-circuit potential

$$\Phi_s|_{x \in [s+,+], t=0} \approx U_{OCP,ca}\left(\frac{c_{s,ca,0}}{c_{s,ca,max}}\right) - U_{OCP,an}\left(\frac{c_{s,an,0}}{c_{s,an,max}}\right),$$

where U_{OCP} is the open-circuit potential function and $c_{s,0}$ is the initial solid-phase concentration. Note that extra subscripts are added to identify anode- and cathode-specific properties.

Secondary-direction, solid-phase Li concentration, c_s. The solid-phase Li concentration is resolved on the secondary r-axis. If it is easier to rationalize, assume that c_s is a function of x and r. However, the gradients in the x-direction are ignored. The solid-phase concentration is only solved for in the anode and cathode domains. These equations are not solved in the separator. The spherical governing equations for the solid-phase concentration are

$$\frac{\partial c_s(x,r)}{\partial t} = -\nabla_r \cdot (-D_s \nabla_r c_s),$$

where D_s is the domain-specific solid-phase diffusion coefficient. In spherical coordinates, this can be expanded to

$$\frac{\partial c_s(x,r)}{\partial t} = \frac{1}{r^2}\frac{\partial}{\partial r}\left(D_s r^2 \frac{\partial c_s}{\partial r}\right),$$

This equation requires radial boundary conditions at the center and surface of the particle. At the particle center, the symmetry condition is

$$\frac{\partial c_s}{\partial r}\Big|_{r=0} = 0.$$

At the particle surface, the flux is specified to be related to the Butler—Volmer current

$$-D_s \frac{\partial c_s}{\partial r}\Big|_{r=R_s} = j.$$

Finally, the domain-specific initial concentration is assumed to be uniform (within the domain) for all x and r locations

$$c_s(t=0)|_{x\in[-,-s],r\in[0,R_s]} = c_{s,an,0}, \quad \text{and} \quad c_s(t=0)|_{x\in[s+,+],r\in[0,R_s]} = c_{s,ca,0}.$$

Note that R_s and $c_{s,0}$ are both domain-specific.

Model parameter expressions. Table S6 documents the constant physics-based model parameters. The parameters with functional dependence are expressed below. Several of these expressions have been published before in Colclasure et al[35], and some have been modified from other works[99,102]. The electrolyte Li-ion diffusion coefficient depends on the salt concentration and temperature and can be expressed as

$$log_{10}\left(1E4\, D_e(c_e,T)\right)$$
$$= \left(-0.5688226 - \frac{1607.003}{T-(-24.83763+64.07366c_e)}\right)$$
$$+ \left(-0.8108721 + \frac{475.291}{T-(-24.83763+64.07366c_e)}\right)c_e$$
$$+ \left(-0.005192312 - \frac{33.43827}{T-(-24.83763+64.07366c_e)}\right)c_e^2.$$

In the above equation, it is assumed that c_e is in kmol m^{-3}, T is in K, and D_e is in m^2 s^{-1}.

The electrolyte ionic conductivity is expressed as a function of salt concentration and temperature as

$$\kappa_e(c_e,T) = c_e\big((0.0001909446\,T^2 - 0.08038545\,T + 9.00341)$$
$$+ (-0.00000002887587\,T^4 + 0.00003483638\,T^3 - 0.01583677\,T^2 + 3.195295\,T - 241.4638)c_e$$
$$+ (0.00000001653786\,T^4 - 0.0000199876\,T^3 + 0.009071155\,T^2 - 1.828064\,T + 138.0976)c_e^2$$
$$+ (-0.000000002791965\,T^4 + 0.000003377143\,T^3 - 0.001532707\,T^2 + 0.3090003\,T - 23.35671)c_e^3\big),$$

where κ_e is in S m^{-1}, c_e is in kmol m^{-3}, and T is in K. The electrolyte thermodynamic factor is a function of concentration and temperature and can be expressed as

$$\left(1 + \frac{\partial \ln f_\pm}{\partial c_e}\right) = 0.54\, c_e^2 \, exp\left(\frac{329}{T}\right) + 0.00225\, c_e exp\left(\frac{1360}{T}\right) - 0.341 exp\left(\frac{261}{T}\right) + 2,$$

where c_e is in kmol m^{-3}, and T is in K. The Li-ion transport number can be expressed as

$$\begin{aligned}
t_+^0 = & (-0.0000002876102\, T^2 + 0.0002077407\, T - 0.03881203) c_e^2 \\
& + (0.000001161463\, T^2 - 0.00086825\, T + 0.1777266) c_e \\
& + (-0.0000006766258\, T^2 + 0.0006389189\, T + 0.3091761),
\end{aligned}$$

where c_e is in kmol m^{-3}, and T is in K. The exchange current density for the anode is expressed as

$$i_{0,an}\left(c_{s,an}|_{r=R_{s,an}}, T\right) =$$
$$0.6\, exp\left(\frac{-30E6}{R}\left(\frac{1}{T} - \frac{1}{303.15}\right)\right) c_e^\alpha \left(c_{s,an,max} - c_{s,an}|_{r=R_{s,an}}\right)^\alpha \left(c_{s,an}|_{r=R_{s,an}}\right)^{1-\alpha},$$

where $c_{s,an}$, c_e, and $c_{s,an,max}$ are in kmol m^{-3} R is in J kmol^{-1} K^{-1}, T is in K, and $i_{0,an}$ is in A m^{-2}. Thus, the pre-factor has units A m$^{-2} \cdot$ [m$^{4.5}$ kmol$_{Li+}^{-0.5}$ kmol$_{Li,s}^{-1}$]. The exchange current density in the cathode can be expressed as

$$\begin{aligned}
i_{0,ca}(x, c_e, T) = & 9(16.50452829641290\, x^5 - 75.23567141488800 x^4 + 124.0524690073040 x^3 \\
& - 94.16571081287610 x^2 + 32.49768821737960\, x \\
& - 3.585290065824760) \left(\frac{c_e}{1.2}\right)^\alpha exp\left(\frac{-30E6}{R}\left(\frac{1}{T} - \frac{1}{303.15}\right)\right),
\end{aligned}$$

where $x = c_{s,ca}|_{r=Rs,ca}/c_{s,ca,max}$ is unitless, c_e is in kmol m^{-3}, T is in K, and $i_{0,ca}$ is in A m^{-2}. The anode solid-phase diffusion coefficient can be expressed as

$$D_{s,an}(T) = 3E - 14\, exp\left(\frac{-30E6}{R}\left(\frac{1}{T} - \frac{1}{303.15}\right)\right)(1.5 - x)^{2.5},$$

where $x = c_{s,an,avg}/c_{s,an,max}$ is unitless, where $D_{s,an}$ is in m^2 s^{-1}, R is in J kmol^{-1} K^{-1}, T is in K. The cathode solid-phase diffusion coefficient can be expressed as

$$D_{s,ca}(x, T) = 2.25 * 10^\gamma\, exp\left(\frac{-30E6}{R}\left(\frac{1}{T} - \frac{1}{303.15}\right)\right),$$
$$\begin{aligned}
\gamma = & -250.9010843479270 x^{10} + 2391.026725259970 x^9 - 4868.420267611360 x^8 \\
& - 83.31104102921070 x^7 + 10576.36028329000 x^6 \\
& - 12683.24548348120 x^5 + 5016.272167775530 x^4 \\
& + 982.4896659649480 x^3 - 1502.439339070900 x^2 \\
& + 472.3709304247700 x^4 - 65.26092046397090,
\end{aligned}$$

where $x = c_{s,ca} / c_{s,ca,max}$ is unitless, R is in J kmol^{-1} K^{-1}, T is in K, and $D_{s,ca}$ is in m^2 s^{-1}.

4.9. Supplementary Information
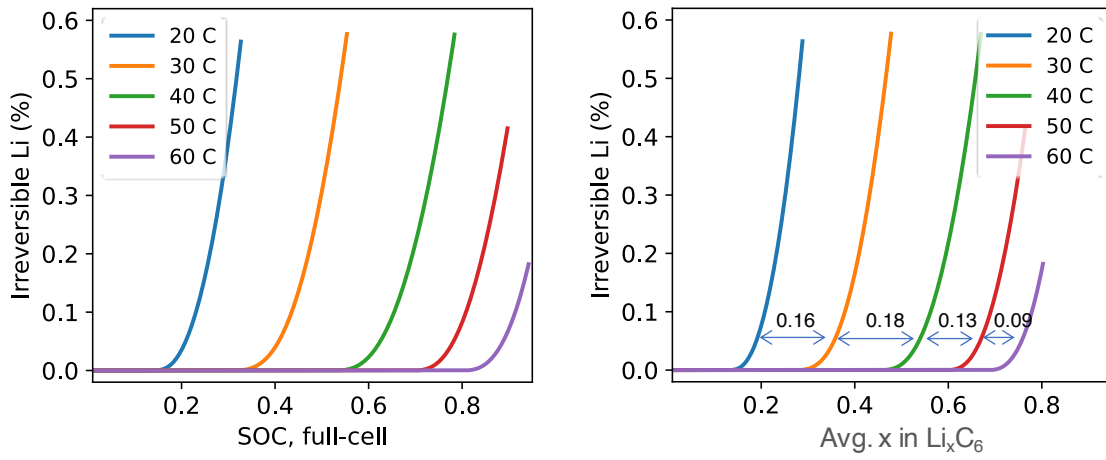
Fig. S46. Calibrated model response to initial temperature change, 6C rate. This illustrates that the Gr|NMC532 model temperature response to Li plating is reasonable given past half-cells Li plating temperature studies of Fig. 8, which estimate a plating onset change (x-direction shift of curves) of about 0.01 Graphite SOC per 1ºC. The data in the right plot are the same as the left, except the x-axis is recast as the expected average graphite electrode lithiation, to enable comparison with past half-cells. The shifts with 10ºC temperature change range 0.09-0.18 SOC.
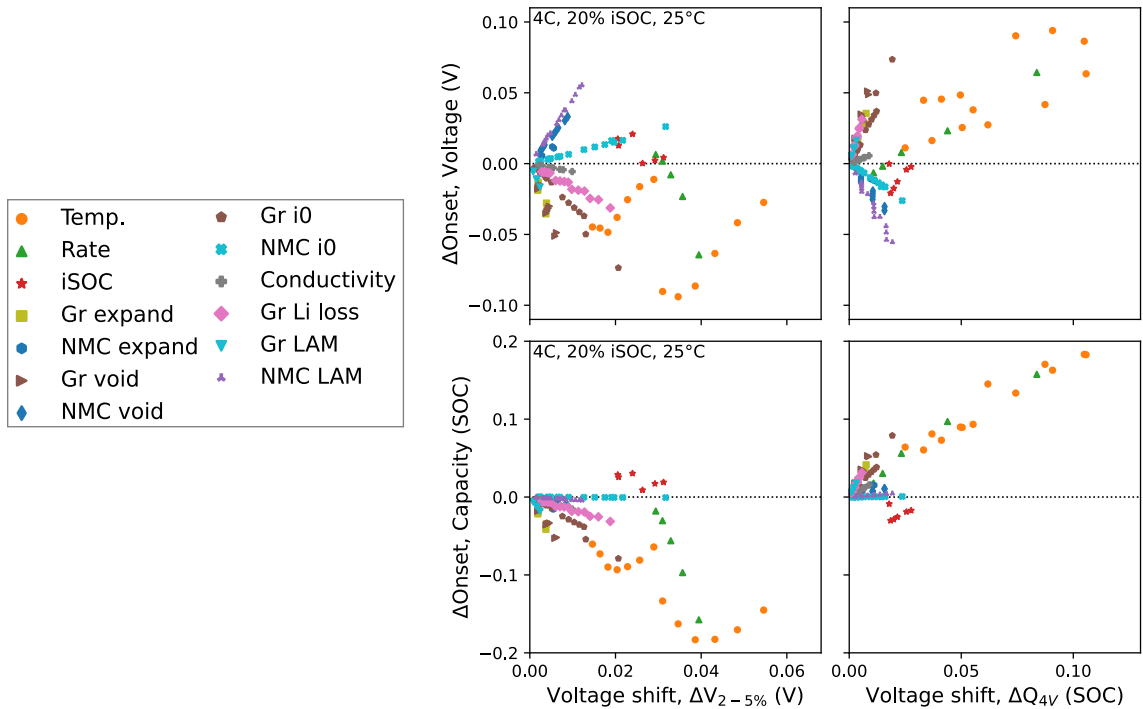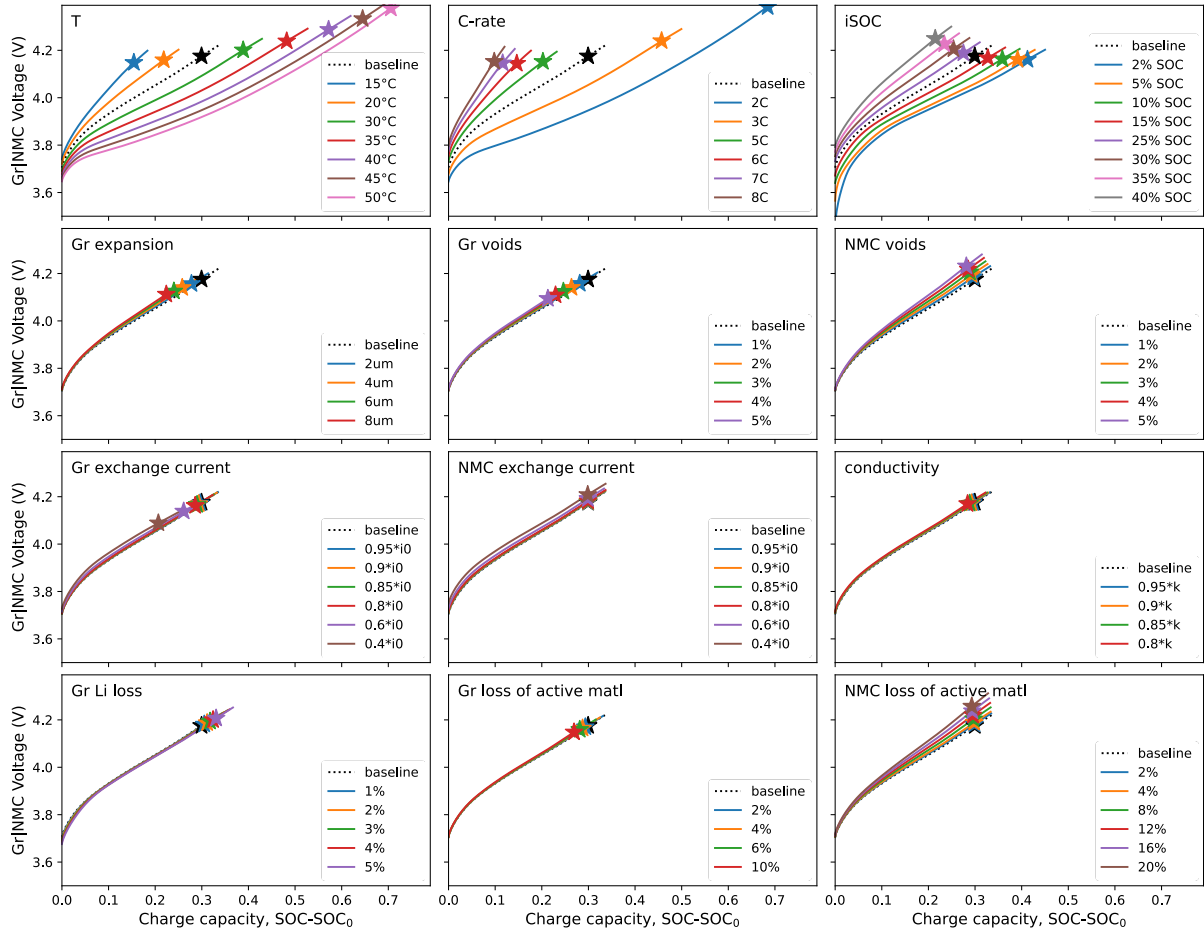
Fig. S47. Sensitivity analysis of Fig. 13-Fig. 14 performed with baseline charging conditions of 4C, 25ºC, 20% initial SOC, and no aging. Trends are similar despite different temperature, SOC, and rate.
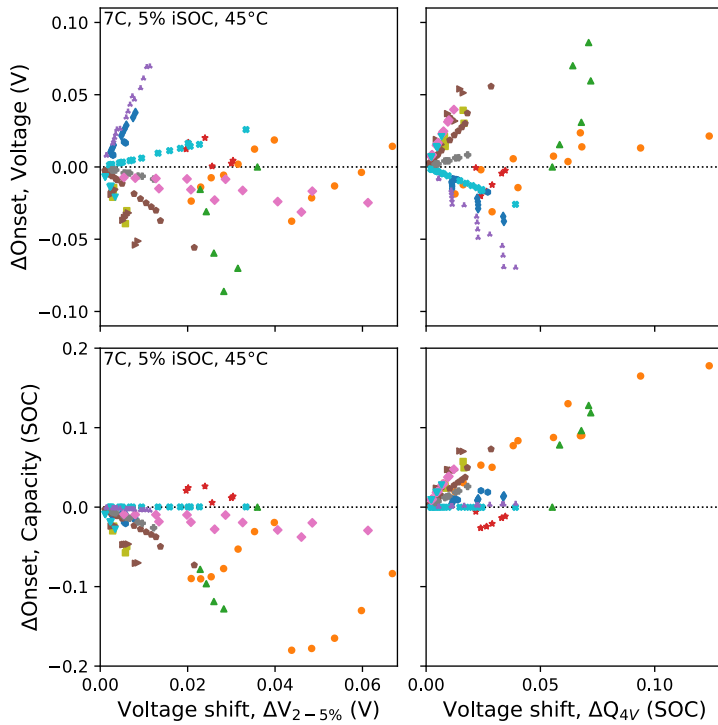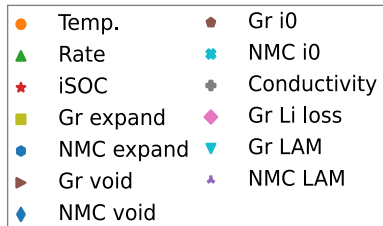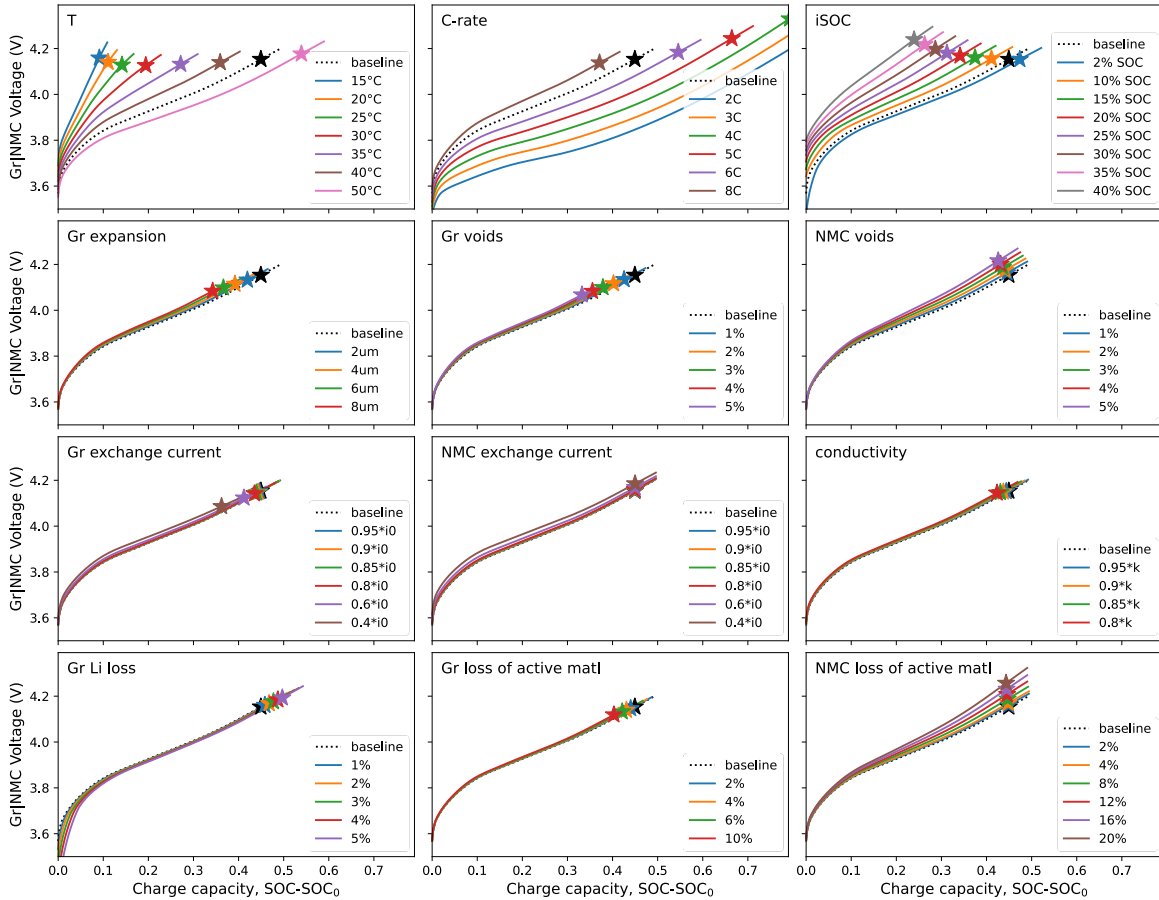
Fig. S48. Sensitivity analysis of Fig. 13-Fig. 14 performed with baseline charging conditions of 7C, 45ºC, 5% initial SOC, and no aging. Trends are similar despite different temperature, SOC, and rate.

5. Conclusions

After a brief introduction (Chapter 1) on the challenges facing Li plating detection in Li-ion batteries, Chapter 2 presents a simple technique for determining the Li plating onset state of charge at rates and temperatures relevant to fast charging. Experimentally determined Li plating onsets were used to design charge steps that avoid Li plating during cycling. We also report a framework for estimating the Li detection limit of electrochemical methods using coulombic efficiencies. For voltage relaxation derivatives (dOCV), that value is near 1% of the graphite electrode capacity, or 4 mAh Li/g graphite, which should motivate the development of dOCV technology for safety applications. The methods presented in this work can be used to validate other Li plating detection techniques, improve predictive Li plating models, and enable efficient charge protocol design.

In Chapter 3, we demonstrated high-throughput experimental protocols for robust quantitative studies of Li plating. We have developed and verified high-throughput cycling techniques to quantify lithium plating in-situ in Li|Graphite and Graphite|NMC cells, and the abundant data have led to physical insights of plating behavior, electrochemical modeling improvements, cell design heuristics, routes toward data-driven plating models, and electrolyte engineering strategies. Going forward, we believe that widespread reporting of irreversible Li plating curves and onset SOC will help quantify the tradeoffs of novel battery design or operation approaches for fast charging, as well as lead to improved fundamental understanding. We hope these techniques are employed by academic and industry researchers and continually adapted to further reduce experiment time, consider battery aging effects on plating, transfer effectively to other cell formats, and study nascent battery chemistries.

Finally in Chapter 4, we demonstrate combined modeling and data-driven approaches to connect measurable voltage values to difficult-to-predict phenomena such as Li plating. The emphasis on understanding the underlying mechanisms will enable reliable machine learning models that use the voltage and other inputs to predict Li plating for diverse conditions.

5.1. Future Work
There are many possible research directions stemming from this work. Some of these include:

Quantify improvements of new graphite electrode design or electrolyte chemistry. The most direct application of these methods is to quantify improvements of electrode design (microstructure, active material supplier, binder content or type, etc.) or electrolyte composition on fast-charging performance. Instead of comparing the long-term cycling capacity retention of 2 experimental cell-types, a common practice influenced by human assembly error, improvements should be reported as a % delay of plating onset SOC, with error bars, encouraging more transparent and reliable electrolyte development science.

Large-format cells testing. The methods developed herein using small mAh-scale single-layer cells should be transferrable to large-format multi-layer multi-Ah cells because they utilize universal battery metrics. However, cell self-heating or heterogeneity within large-format cells may affect Li plating accumulation. It would be particularly interesting to understand the distribution of Li plating onsets for identically manufactured cells, and how this varies after the

cells have been cycled 500, 1000, 2000, 5000 etc. times. These studies would be most readily performed by industry partners but could also be an applied academic project.

Understand the impact of novel cathodes. This work used an NMC532 cathode throughout, which as of 2023 is an undesirable material due to its high cobalt content and is being replaced with cheaper, less energy dense, electrodes such as LFP. The experimental and modeling methods should be applied to understand further the influence of additional cathode chemistries on fast-charging performance and the efficacy of the methods developed with NMC532 cathodes.

Operando lithium plating prediction model development. From the battery management system perspective, a critical question is: given the following available data, with what accuracy can the plating onset SOC (later during the same charge) be predicted?

- measured real-time charging voltage at beginning-of-charge
- scheduled charging rate or current step sequence
- estimated, or measured with low resolution, cell temperature
- estimated cell aging or health metrics
- estimated SOC

Developing data-driven models that are computationally efficient would enable more effective on-board vehicle or device Li plating prevention. This would be an improvement over the simple voltage boundary plating prevention method of Chapter 4. This analysis could also indicate, for example, how accurate a temperature estimate is required to closely predict the Li plating onset SOC, an insight that could inform battery pack thermocouple placement.

Finally, it is my hope that this work and future efforts enable the rapid adoption of affordable, long-lasting electric vehicles that help mitigate the climate crisis. If the reader finds themselves working towards this effort and would find discussion with the author helpful, please do not hesitate to reach out via LinkedIn or via Advisor Bryan D. McCloskey, with whom the author will maintain updated contact information.

6. References

1. Kane, M. US: All-Electric Car Sales Increased In Q1 2023: 257,000 Registrations. *InsideEVs* https://insideevs.com/news/667516/us-electric-car-sales-2023 (2023).
2. Steven Boyd. Batteries and Electrification R&D Overview. *Batteries and Electrification R&D Overview, U.S. Department of Energy (DOE) Vehicle Technologies Office (VTO) Annual Merit Review Meeting (AMR)* 20 https://www.energy.gov/sites/prod/files/2018/06/f53/bat918_boyd_2018.pdf (2018).
3. Severson, K. A. *et al.* Data-driven prediction of battery cycle life before capacity degradation. *Nat. Energy* **4**, 383–391 (2019).
4. Zhang, Y. *et al.* Identifying degradation patterns of lithium ion batteries from impedance spectroscopy using machine learning. *Nat. Commun.* **11**, 1706 (2020).
5. Ahmed, S. *et al.* Enabling fast charging – A battery technology gap assessment. *J. Power Sources* **367**, 250–262 (2017).
6. Mao, C., Ruther, R. E., Li, J., Du, Z. & Belharouak, I. Identifying the limiting electrode in lithium ion batteries for extreme fast charging. *Electrochem. commun.* **97**, 37–41 (2018).
7. Christensen, J. & Newman, J. Cyclable Lithium and Capacity Loss in Li-Ion Cells. *J. Electrochem. Soc.* **152**, A818–A829 (2005).
8. Attia, P. M. *et al.* Closed-loop optimization of fast-charging protocols for batteries with machine learning. *Nature* **578**, 397–402 (2020).
9. Yamada, Y., Iriyama, Y., Abe, T. & Ogumi, Z. Kinetics of lithium ion transfer at the interface between graphite and liquid electrolytes: effects of solvent and surface film. *Langmuir* **25**, 12766–12770 (2009).
10. Ho, A. S. *et al.* 3D Detection of Lithiation and Lithium Plating in Graphite Anodes during Fast Charging. *ACS Nano* **15**, 10480–10487 (2021).
11. Colclasure, A. M. *et al.* Electrode scale and electrolyte transport effects on extreme fast charging of lithium-ion cells. *Electrochim. Acta* **337**, 135854 (2020).
12. Chen, K. H. *et al.* Efficient fast-charging of lithium-ion batteries enabled by laser-patterned three-dimensional graphite anode architectures. *J. Power Sources* **471**, 228475 (2020).
13. Dunlap, N. *et al.* Laser ablation of Li-ion electrodes for fast charging: Material properties, rate capability, Li plating, and wetting. *J. Power Sources* **537**, 231464 (2022).
14. Gotoh, K. *et al.* In situ 7Li nuclear magnetic resonance study of the relaxation effect in practical lithium ion batteries. *Carbon N. Y.* **79**, 380–387 (2014).
15. Zinth, V. *et al.* Lithium plating in lithium-ion batteries at sub-ambient temperatures investigated by in situ neutron diffraction. *J. Power Sources* **271**, 152–159 (2014).
16. Ghanbari, N., Waldmann, T., Kasper, M., Axmann, P. & Wohlfahrt-Mehrens, M. Detection of Li Deposition by Glow Discharge Optical Emission Spectroscopy in Post-Mortem Analysis. *ECS Electrochem. Lett.* **4**, A100–A102 (2015).
17. Wandt, J., Jakes, P., Granwehr, J., Eichel, R. A. & Gasteiger, H. A. Quantitative and time-resolved detection of lithium plating on graphite anodes in lithium ion batteries. *Mater. Today* **21**, 231–240 (2018).
18. Bommier, C. *et al.* In Operando Acoustic Detection of Lithium Metal Plating in Commercial LiCoO2/Graphite Pouch Cells. *Cell Reports Phys. Sci.* (2020) doi:10.1016/j.xcrp.2020.100035.
19. Waldmann, T., Hogg, B. I. & Wohlfahrt-Mehrens, M. Li plating as unwanted side reaction in commercial Li-ion cells – A review. *J. Power Sources* **384**, 107–124 (2018).

20. Liu, Y., Zhu, Y. & Cui, Y. Challenges for electrolyte mass transport Challenges and opportunities towards fast-charging battery materials. *Nat. Energy* **4**, 540–550 (2019).

21. Wu, Y. *et al.* An Empirical Model for the Design of Batteries. *ACS Energy Lett.* **5**, 807–816 (2020).

22. Schindler, S., Bauer, M., Petzl, M. & Danzer, M. A. Voltage relaxation and impedance spectroscopy as in-operando methods for the detection of lithium plating on graphitic anodes in commercial lithium-ion cells. *J. Power Sources* **304**, 170–180 (2016).

23. Uhlmann, C., Illig, J., Ender, M., Schuster, R. & Ivers-Tiffée, E. In situ detection of lithium metal plating on graphite in experimental cells. *J. Power Sources* **279**, 428–438 (2015).

24. von Lüders, C. *et al.* Lithium plating in lithium-ion batteries investigated by voltage relaxation and in situ neutron diffraction. *J. Power Sources* **342**, 17–23 (2017).

25. Yang, X. G., Ge, S., Liu, T., Leng, Y. & Wang, C. Y. A look into the voltage plateau signal for detection and quantification of lithium plating in lithium-ion cells. *J. Power Sources* **395**, 251–261 (2018).

26. Ren, D. *et al.* Investigation of Lithium Plating-Stripping Process in Li-Ion Batteries at Low Temperature Using an Electrochemical Model. *J. Electrochem. Soc.* **165**, A2167–A2178 (2018).

27. Rao Koleti, U., Zhang, C., Malik, R., Quang Dinh, T. & Marco, J. The development of optimal charging strategies for lithium-ion batteries to prevent the onset of lithium plating at low ambient temperatures. *J. Energy Storage* **24**, 100798 (2019).

28. Bauer, M. *et al.* Multi-phase formation induced by kinetic limitations in graphite-based lithium-ion cells: Analyzing the effects on dilation and voltage response. *J. Energy Storage* **10**, 1–10 (2017).

29. Rao Koleti, U., Quang Dinh, T. & Marco, J. A new on-line method for lithium plating detection in lithium-ion batteries. *J. Power Sources* **451**, 227798 (2020).

30. Fan, J. & Tan, S. Studies on charging lithium-ion cells at low temperatures. *J. Electrochem. Soc.* **153**, A1081–A1092 (2006).

31. Burns, J. C., Stevens, D. A. & Dahn, J. R. In-Situ Detection of Lithium Plating Using High Precision Coulometry. *J. Electrochem. Soc.* **162**, A959–A964 (2015).

32. Tanim, T. R., Dufek, E. J., Dickerson, C. C. & Wood, S. M. Electrochemical Quantification of Lithium Plating: Challenges and Considerations. *J. Electrochem. Soc.* **166**, A2689–A2696 (2019).

33. Rodrigues, M.-T. F. *et al.* Fast Charging of Li-Ion Cells: Part I. Using Li/Cu Reference Electrodes to Probe Individual Electrode Potentials. *J. Electrochem. Soc.* **166**, A996–A1003 (2019).

34. Diederichsen, K. M., McShane, E. J. & McCloskey, B. D. Promising Routes to a High Li+ Transference Number Electrolyte for Lithium Ion Batteries. *ACS Energy Lett.* **2**, 2563–2575 (2017).

35. Colclasure, A. M. *et al.* Requirements for Enabling Extreme Fast Charging of High Energy Density Li-Ion Cells while Avoiding Lithium Plating. *J. Electrochem. Soc.* **166**, A1412–A1424 (2019).

36. Aurbach, D. Review of selected electrode-solution interactions which determine the performance of Li and Li ion batteries. *J. Power Sources* **89**, 206–218 (2000).

37. Wang, L. *et al.* Identifying the components of the solid–electrolyte interphase in Li-ion batteries. *Nat. Chem.* **11**, 789–796 (2019).

38. Petzl, M. & Danzer, M. A. Nondestructive detection, characterization, and quantification of

lithium plating in commercial lithium-ion batteries. *J. Power Sources* **254**, 80–87 (2014).

39. McShane, E. J. *et al.* Quantification of Inactive Lithium and Solid–Electrolyte Interphase Species on Graphite Electrodes after Fast Charging. *ACS Energy Lett.* **5**, 2045–2051 (2020).

40. Smart, M. C. & Ratnakumar, B. V. Effects of electrolyte composition on lithium plating in lithium-ion cells. *J. Electrochem. Soc.* **158**, 379–389 (2011).

41. Campbell, I. D., Marzook, M., Marinescu, M. & Offer, G. J. How Observable Is Lithium Plating? Differential Voltage Analysis to Identify and Quantify Lithium Plating Following Fast Charging of Cold Lithium-Ion Batteries. *J. Electrochem. Soc.* **166**, A725–A739 (2019).

42. Rashingkar, G. & Frost & Sullivan. *Global Li-ion Battery Materials Growth Opportunities*. https://www.marketresearch.com/Frost-Sullivan-v383/Global-Li-ion-Battery-Materials-14856305/ (2021).

43. Zhang, S. S., Xu, K. & Jow, T. R. Study of the charging process of a LiCoO2-based Li-ion battery. *J. Power Sources* **160**, 1349–1354 (2006).

44. Tobishima, S. I. & Yamaki, J. I. A consideration of lithium cell safety. *J. Power Sources* **81**–**82**, 882–886 (1999).

45. DNV-GL and Arizona Public Service. *McMicken Battery Energy Storage System Event Technical Analysis and Recommendations*. https://www.aps.com/-/media/APS/APSCOM-PDFs/About/Our-Company/Newsroom/McMickenFinalTechnicalReport.ashx?la=en&hash=50335FB5098D9858BFD276C40FA54FCE (2020).

46. Arora, P., Doyle, M. & White, R. E. Mathematical Modeling of the Lithium Deposition Overcharge Reaction in Lithium-Ion Batteries Using Carbon-Based Negative Electrodes. *J. Electrochem. Soc.* **146**, 3543 (1999).

47. Tang, M., Albertus, P. & Newman, J. Two-Dimensional Modeling of Lithium Deposition during Cell Charging. *J. Electrochem. Soc.* **156**, A390 (2009).

48. Paul, P. P. *et al.* A Review of Existing and Emerging Methods for Lithium Detection and Characterization in Li-Ion and Li-Metal Batteries. *Adv. Energy Mater.* **11**, 1–29 (2021).

49. Fang, C. *et al.* Quantifying inactive lithium in lithium metal batteries. *Nature* **572**, 511–515 (2019).

50. Deng, Z. *et al.* Towards autonomous high-throughput multiscale modelling of battery interfaces. *Energy Environ. Sci.* **15**, 579–594 (2022).

51. Kang, K., Meng, Y. S., Bréger, J., Grey, C. P. & Ceder, G. Electrodes with high power and high capacity for rechargeable lithium batteries. *Science (80-.).* **311**, 977–980 (2006).

52. Qie, L. *et al.* Nitrogen-doped porous carbon nanofiber webs as anodes for lithium ion batteries with a superhigh capacity and rate capability. *Adv. Mater.* **24**, 2047–2050 (2012).

53. Smith, A. J., Burns, J. C., Trussler, S. & Dahn, J. R. Precision Measurements of the Coulombic Efficiency of Lithium-Ion Batteries and of Electrode Materials for Lithium-Ion Batteries. *J. Electrochem. Soc.* **157**, A196 (2009).

54. Dahn, J. R., Burns, J. C. & Stevens, D. A. Importance of coulombic efficiency measurements in R & D efforts to obtain long-lived li-ion batteries. *Electrochem. Soc. Interface* **25**, 75–78 (2016).

55. Aykol, M., Herring, P. & Anapolsky, A. Machine learning for continuous innovation in battery technologies. *Nat. Rev. Mater.* **5**, 725–727 (2020).

56. Konz, Z. M., McShane, E. J. & McCloskey, B. D. Detecting the onset of lithium plating and monitoring fast charging performace with voltage relaxation. *ACS Energy Lett.* **5**, 1750–1757 (2020).

57. Adam, A., Knobbe, E., Wandt, J. & Kwade, A. Application of the differential charging voltage analysis to determine the onset of lithium-plating during fast charging of lithium-ion cells. *J. Power Sources* **495**, 229794 (2021).

58. Finegan, D. P. *et al.* Spatial dynamics of lithiation and lithium plating during high-rate operation of graphite electrodes. *Energy Environ. Sci.* **13**, 2570–2584 (2020).

59. Robertson, D. C. *et al.* Effect of Anode Porosity and Temperature on the Performance and Lithium Plating During Fast-Charging of Lithium-Ion Cells. *Energy Technol.* **9**, 1–14 (2021).

60. Chen, Y. *et al.* Operando video microscopy of Li plating and re-intercalation on graphite anodes during fast charging. *J. Mater. Chem. A* **9**, 23522–23536 (2021).

61. Adam, A. *et al.* Development of an innovative workflow to optimize the fast-charge capability of lithium-ion battery cells. *J. Power Sources* **512**, 230469 (2021).

62. Hobold, G. M. *et al.* Moving beyond 99.9% Coulombic efficiency for lithium anodes in liquid electrolytes. *Nat. Energy* **6**, 951–960 (2021).

63. Gunnarsdóttir, A. B., Amanchukwu, C. V., Menkin, S. & Grey, C. P. Noninvasive in Situ NMR Study of 'dead Lithium' Formation and Lithium Corrosion in Full-Cell Lithium Metal Batteries. *J. Am. Chem. Soc.* **142**, 20814–20827 (2020).

64. Gao, T. *et al.* Interplay of Lithium Intercalation and Plating on a Single Graphite Particle. *Joule* **5**, 393–414 (2021).

65. Martin, C., Genovese, M., Louli, A. J., Weber, R. & Dahn, J. R. Cycling Lithium Metal on Graphite to Form Hybrid Lithium-Ion/Lithium Metal Cells. *Joule* **4**, 1296–1310 (2020).

66. Cai, W. *et al.* The Boundary of Lithium Plating in Graphite Electrode for Safe Lithium-Ion Batteries. *Angew. Chemie - Int. Ed.* **60**, 13007–13012 (2021).

67. Mei, W., Jiang, L., Liang, C., Sun, J. & Wang, Q. Understanding of Li-plating on graphite electrode: detection, quantification and mechanism revelation. *Energy Storage Mater.* **41**, 209–221 (2021).

68. Brown, D. E., McShane, E. J., Konz, Z. M., Knudsen, K. B. & McCloskey, B. D. Detecting onset of lithium plating during fast charging of Li-ion batteries using operando electrochemical impedance spectroscopy. *Cell Reports Phys. Sci.* **2**, 100589 (2021).

69. Duangdangchote, S. *et al.* Effect of fluoroethylene carbonate on the transport property of electrolytes towards Ni-rich Li-ion batteries with high safety. *Chem. Commun.* **57**, 6732–6735 (2021).

70. Yan, S. *et al.* Regulating the growth of lithium dendrite by coating an ultra-thin layer of gold on separator for improving the fast-charging ability of graphite anode. *J. Energy Chem.* **67**, 467–473 (2022).

71. Shin, H., Park, J., Sastry, A. M. & Lu, W. Effects of Fluoroethylene Carbonate (FEC) on Anode and Cathode Interfaces at Elevated Temperatures. *J. Electrochem. Soc.* **162**, A1683–A1692 (2015).

72. Kazyak, E., Chen, K. H., Chen, Y., Cho, T. H. & Dasgupta, N. P. Enabling 4C Fast Charging of Lithium-Ion Batteries by Coating Graphite with a Solid-State Electrolyte. *Adv. Energy Mater.* **12**, (2022).

73. Paul, P. P. *et al.* Quantification of heterogeneous, irreversible lithium plating in extreme fast charging of lithium-ion batteries. *Energy Environ. Sci.* **14**, 4979–4988 (2021).

74. Gong, C. *et al.* Revealing the Role of Fluoride-Rich Battery Electrode Interphases by Operando Transmission Electron Microscopy. *Adv. Energy Mater.* **11**, 2003118 (2021).

75. Renfrew, S. E. & McCloskey, B. D. Residual Lithium Carbonate Predominantly Accounts

for First Cycle CO2 and CO Outgassing of Li-Stoichiometric and Li-Rich Layered Transition-Metal Oxides. *J. Am. Chem. Soc.* **139**, 17853–17860 (2017).

76. Cannarella, J. & Arnold, C. B. The Effects of Defects on Localized Plating in Lithium-Ion Batteries. *J. Electrochem. Soc.* **162**, A1365–A1373 (2015).

77. Attia, P. M. *et al.* Review—"Knees" in Lithium-Ion Battery Aging Trajectories. *J. Electrochem. Soc.* (2022) doi:10.1149/1945-7111/ac6d13.

78. Yang, X. G., Leng, Y., Zhang, G., Ge, S. & Wang, C. Y. Modeling of lithium plating induced aging of lithium-ion batteries: Transition from linear to nonlinear aging. *J. Power Sources* **360**, 28–40 (2017).

79. Smith, A. J. *et al.* Localized lithium plating under mild cycling conditions in high-energy lithium-ion batteries. *J. Power Sources* **573**, (2023).

80. Dufek, E. J. *et al.* Developing extreme fast charge battery protocols – A review spanning materials to systems. *J. Power Sources* **526**, 231129 (2022).

81. Tomaszewska, A. *et al.* Lithium-ion battery fast charging: A review. *eTransportation* **1**, 100011 (2019).

82. Mai, W., Colclasure, A. M. & Smith, K. Model-Instructed Design of Novel Charging Protocols for the Extreme Fast Charging of Lithium-Ion Batteries Without Lithium Plating. *J. Electrochem. Soc.* **167**, 080517 (2020).

83. Sieg, J. *et al.* Fast charging of an electric vehicle lithium-ion battery at the limit of the lithium deposition process. *J. Power Sources* **427**, 260–270 (2019).

84. Waldmann, T., Kasper, M. & Wohlfahrt-mehrens, M. Optimization of Charging Strategy by Prevention of Lithium Deposition on Anodes in high-energy Lithium-ion Batteries – Electrochemical Experiments. *Electrochim. Acta* **178**, 525–532 (2015).

85. Epding, B., Rumberg, B., Mense, M., Jahnke, H. & Kwade, A. Aging-Optimized Fast Charging of Lithium Ion Cells Based on Three-Electrode Cell Measurements. *Energy Technol.* **8**, 1–9 (2020).

86. Jiang, B. *et al.* Bayesian learning for rapid prediction of lithium-ion battery-cycling protocols. *Joule* **5**, 3187–3203 (2021).

87. Klein, R. *et al.* Optimal charging strategies in lithium-ion battery. *Proc. Am. Control Conf.* 382–387 (2011) doi:10.1109/acc.2011.5991497.

88. Perez, H., Shahmohammadhamedani, N. & Moura, S. Enhanced Performance of Li-Ion Batteries via Modified Reference Governors and Electrochemical Models. *IEEE/ASME Trans. Mechatronics* **20**, 1511–1520 (2015).

89. Romagnoli, R., Couto, L. D., Goldar, A., Kinnaert, M. & Garone, E. A feedback charge strategy for Li-ion battery cells based on Reference Governor. *J. Process Control* **83**, 164–176 (2019).

90. Hahn, M. *et al.* Model predictive fast charging control by means of a real-time discrete electrochemical model. *J. Energy Storage* **42**, 103056 (2021).

91. Couto, L. D. *et al.* Faster and Healthier Charging of Lithium-Ion Batteries via Constrained Feedback Control. *IEEE Trans. Control Syst. Technol.* **30**, 1990–2001 (2022).

92. Drummond, R., Courtier, N. E., Howey, D. A., Couto, L. D. & Guiver, C. Constrained optimal control of monotone systems with applications to battery fast-charging. 1–13 (2023).

93. Wassiliadis, N., Kriegler, J., Abo, K. & Lienkamp, M. Model-based health-aware fast charging to mitigate the risk of lithium plating and prolong the cycle life of lithium-ion batteries in electric vehicles. *J. Power Sources* **561**, 232586 (2023).

94. Liu, T., Ge, S., Yang, X. G. & Wang, C. Y. Effect of thermal environments on fast charging Li-ion batteries. *J. Power Sources* **511**, 230466 (2021).

95. Keyser, M. *et al.* Enabling fast charging – Battery thermal considerations. *J. Power Sources* **367**, 228–236 (2017).

96. Zeng, Y. *et al.* Extreme fast charging of commercial Li-ion batteries via combined thermal switching and self-heating approaches. *Nat. Commun.* 1–9 (2023) doi:10.1038/s41467-023-38823-9.

97. Tanim, T. R., Shirk, M. G., Bewley, R. L., Dufek, E. J. & Liaw, B. Y. Fast charge implications: Pack and cell analysis and comparison. *J. Power Sources* **381**, 56–65 (2018).

98. Zilberman, I., Ludwig, S., Schiller, M. & Jossen, A. Online aging determination in lithium-ion battery module with forced temperature gradient. *J. Energy Storage* **28**, 101170 (2020).

99. Konz, Z. M. *et al.* High-throughput Li plating quantification for fast-charging battery design. *Nat. Energy* (2023) doi:10.1038/s41560-023-01194-y.

100. Smith, R. B., Khoo, E. & Bazant, M. Z. Intercalation Kinetics in Multiphase-Layered Materials. *J. Phys. Chem. C* **121**, 12505–12523 (2017).

101. Chen, Z. *et al.* Overpotential analysis of graphite-based Li-ion batteries seen from a porous electrode modeling perspective. *J. Power Sources* **509**, 230345 (2021).

102. Weddle, P. J. *et al.* Battery State-of-Health Diagnostics During Fast Cycling Using Physics-Informed Deep-Learning. (2023).

103. Pegel, H. *et al.* Fast-charging performance and optimal thermal management of large-format full-tab cylindrical lithium-ion cells under varying environmental conditions. *J. Power Sources* **556**, 232408 (2023).

104. Adam, A., Wandt, J., Knobbe, E., Bauer, G. & Kwade, A. Fast-Charging of Automotive Lithium-Ion Cells: In-Situ Lithium-Plating Detection and Comparison of Different Cell Designs. *J. Electrochem. Soc.* **167**, 130503 (2020).

105. T. Heenan. Mapping internal temperatures during high-rate battery applications. *Nature* **617**, (2023).

106. Fleckenstein, M., Bohlen, O., Roscher, M. A. & Bäker, B. Current density and state of charge inhomogeneities in Li-ion battery cells with LiFePO4 as cathode material due to temperature gradients. *J. Power Sources* **196**, 4769–4778 (2011).